University of Nottingham
UK | CHINA | MALAYSIA

Electrical Control of Antiferromagnetic CuMnAs

Oliver James Amin

Thesis submitted to the University of Nottingham
for the degree of Doctor of Philosophy

March 2022

Abstract

Antiferromagnetic (AF) materials are expected to become the primary components in next generation magnetic memory devices, due to their ultrafast spin dynamics, robustness against external magnetic fields, and downsize scalability. The most promising candidate material, so far, is tetragonal CuMnAs - a semimetal AF with the required crystal symmetry to host current-induced Néel spin-orbit torque. This offers a novel way to efficiently manipulate the AF order using electrical pulses.

The work presented in this thesis explores the effect of electrical pulses on the transport properties and AF domain structure in tetragonal CuMnAs thin films, epitaxially grown on GaP(001) and GaAs(001) substrates. It is revealed in the transport measurements that the onset of a large magnetoresistive switching signal, $> 1\%$, occurs above a pulse current density threshold. The signal exhibits a multicomponent exponential relaxation, which is shown to follow Néel-Arrhenius behaviour. A temperature dependent study of the signal relaxation is compared in three different CuMnAs layers: 20 nm and 45 nm layers grown on GaP(001), and a 60 nm layer grown on GaAs(001). Whilst the relaxation components show a strong dependence on the CuMnAs layer thickness and sample temperature, the extracted material dependent attempt rates all fall within the terahertz range of AF spin dynamics.

Synchrotron based magnetic imaging technique, X-ray magnetic linear dichroism combined with photoemission electron microscopy, is used to directly image current-induced changes to the AF domain structure of devices fabricated from 50 nm layers of CuMnAs grown on GaP(001). At relatively low pulse current densities, 180° domain walls are observed to move between pinning sites in a reversible and repeatable manner, depending on the direction of the pulse. It is also shown that topological AF vortices and antivortices can be stabilized at room temperature in CuMnAs. Vortex-antivortex pairs are generated and moved using electrical pulses. Their coherent movement is reversible and repeatable, in the direction of the pulse.

Acknowledgements

My supervisors, Peter Wadley and Kevin Edmonds, are the best two people I could have hoped to work with. Their unrivalled sense of humour, friendliness, and passion for research (most important to least important) has made my PhD a real enjoyment. If it wasn't for Pete I would have never started this project and if it wasn't for Kev I would have never finished.

Being crammed into a PhD office, you are forced to get to know people, and during my 4 year shift I decided that some of them weren't so bad. Luke Barton, fountain of all superfluous knowledge and supplier of mediocre banter, began his PhD at the same time as me. We had a lot of fun over the 4 years, much of which involved pub trips, and he will remain a close friend of mine. Sonka Reimers, winner of ridiculously long distance races and provider of Barney Bears. I've never met someone with so much drive. Although she spent half of her PhD at diamond we still formed a strong friendship and it was always fun visit her at beamtimes. Stuart Poole joined the office a couple of years into my PhD. He was immediately assigned role as IT support, based entirely on his custom keyboard that was designed to be as loud as possible. He opened my ears to a range of incredibly niche music ranging from the drummiest drum and bass, to the heaviest metal subgenres. The newest arrival to the office, Alfred Dal Din, also deserves a shout-out. He has shown a fresh fascination for the research, which really reminded me of being a new PhD student. He has also been incredibly encouraging during the later stages of my thesis writing.

Outside of the physics building, my family have been a massive support to me during my PhD. Mum, Dad, Alex and Rachel, as well as Linda and Barry, you've all shown genuine interest in the work I've been doing, which has made it feel so worthwhile. Most importantly, Meg has been my biggest supporter. She has made my life outside of physics so enjoyable and I can't thank her enough!

List of Publications

The following publication directly corresponds to Chapter 3 of this thesis:

1. Amin, O.J., Edmonds, K.W., Wadley, P., 2020. "Electrical control of antiferromagnets for the next generation of computing technology". *Appl. Phys. Lett.* 117, 010501.
   https://doi.org/10.1063/5.0013917

Other publications to which the author of this thesis contributed:

2. Wang, M., Andrews, C., Reimers, S., Amin, O.J., Wadley, P., Campion, R.P., Poole, S.F., Felton, J., Edmonds, K.W., Gallagher, B.L., Rushforth, A.W., Makarovsky, O., Gas, K., Sawicki, M., Kriegner, D., Zubáč, J., Olejník, K., Novák, V., Jungwirth, T., Shahrokhvand, M., Zeitler, U., Dhesi, S.S., Maccherozzi, F., 2020. "Spin flop and crystalline anisotropic magnetoresistance in CuMnAs". *Phys. Rev. B* 101, 094429.
   https://doi.org/10.1103/PhysRevB.101.094429

3. Omari, K.A., Barton, L.X., Amin, O., Campion, R.P., Rushforth, A.W., Kent, A.J., Wadley, P., Edmonds, K.W., 2020. "Low-energy switching of antiferromagnetic CuMnAs/GaP using sub-10 nanosecond current pulses". *Journal of Applied Physics* 127, 193906.
   https://doi.org/10.1063/5.0006183

4. Janda, T., Godinho, J., Ostatnicky, T., Pfitzner, E., Ulrich, G., Hoehl, A., Reimers, S., Šobáň, Z., Metzger, T., Reichlová, H., Novák, V., Campion, R.P., Heberle, J., Wadley, P., Edmonds, K.W., Amin, O.J., Chauhan, J.S., Dhesi, S.S., Maccherozzi, F., Otxoa, R.M., Roy, P.E., Olejník, K., Němec, P., Jungwirth, T., Kaestner, B., Wunderlich, J., 2020. "Magneto-Seebeck microscopy of domain switching in collinear antiferromagnet CuMnAs". *Phys. Rev. Materials* 4, 094413.
   https://doi.org/10.1103/PhysRevMaterials.4.094413

5. Krizek, F., Reimers, S., Kašpar, Z., Marmodoro, A., Michalička, J., Man, O., Edstrom, A., Amin, O.J., Edmonds, K.W., Campion, R.P., Maccherozzi, F., Dnes, S.S., Zubáč, J., Železný, J., Výborný, K., Olejník, K., Novák, V., Rusz, J., Idrobo, J.C., Wadley, P., Jungwirth, T., 2020. "Atomically sharp domain walls in an antiferromagnet". arXiv:2012.00894 [cond-mat].
   https://doi.org/10.48550/arXiv.2012.00894

6. Kašpar, Z., Surýnek, M., Zubáč, J., Krizek, F., Novák, V., Campion, R.P., Wörnle, M.S., Gambardella, P., Marti, X., Němec, P., Edmonds, K.W., Reimers, S.,

Amin, O.J., Maccherozzi, F., Dhesi, S.S., Wadley, P., Wunderlich, J., Olejník, K., Jungwirth, T., 2021. "Quenching of an antiferromagnet into high resistivity states using electrical or ultrashort optical pulses". *Nat Electron* 4, 30–37. https://doi.org/10.1038/s41928-020-00506-4

7. Reimers, S., Kriegner, D., Gomonay, O., Carbone, D., Krizek, F., Novák, V., Campion, R.P., Maccherozzi, F., Björling, A., Amin, O.J., Barton, L.X., Poole, S.F., Omari, K.A., Michalička, J., Man, O., Sinova, J., Jungwirth, T., Wadley, P., Dhesi, S.S., Edmonds, K.W., 2022. "Defect-driven antiferromagnetic domain walls in CuMnAs films". *Nat Commun* 13, 724. https://doi.org/10.1038/s41467-022-28311-x

Contents

List of Tables

List of Figures

Chapter 1

Introduction

Magnetically ordered materials have been successfully implemented as memory devices, known as magnetoresistive random access memory (MRAM) [1–4]. Information is stored in the relative orientation of the magnetic order, read from the magnetoresistance, and written using external magnetic fields and electrical currents. Most forms of commercial MRAM consist of two stacked ferromagnetic (FM) layers separated by a non-magnetic spacer. The magnetic order (magnetization) in one of the FM layers is free to move, while the other is kept fixed by an adjacent pinned reference layer. Depending on the relative orientation of the layer magnetizations, a current flowing vertically through the stack experiences high or low resistance. This is due to the giant magnetoresistance (GMR) in a spin-valve (type of stack) where the spacer layer is conducting, or tunneling magnetoresistance (TMR) in a magnetic tunneling junction (MTJ) where the spacer layer is insulating [2–5]. The way in which the FM free layer magnetization is controlled has developed over the years to improve device scalability and increase the speed of reading and writing.

An early form of MRAM, called toggle-MRAM, uses a magnetic field to rotate both FM layers in an MTJ, as shown in Figure 1.1 [2]. At equilibrium, in the absence of a field, the FM layers form a synthetic antiferromagnet (SAF), with equal in-plane magnetizations aligned antiparallel cancelling each other out. A field, generated by applying currents along wires, or 'write lines', running at orthogonal directions above and below the MTJ, induces a spin-flop transition which cant the magnetizations and creates a small net magnetization in the direction of the field. By varying the current applied along each line, the field direction can be rotated, reorienting the SAF layer magnetizations 180°

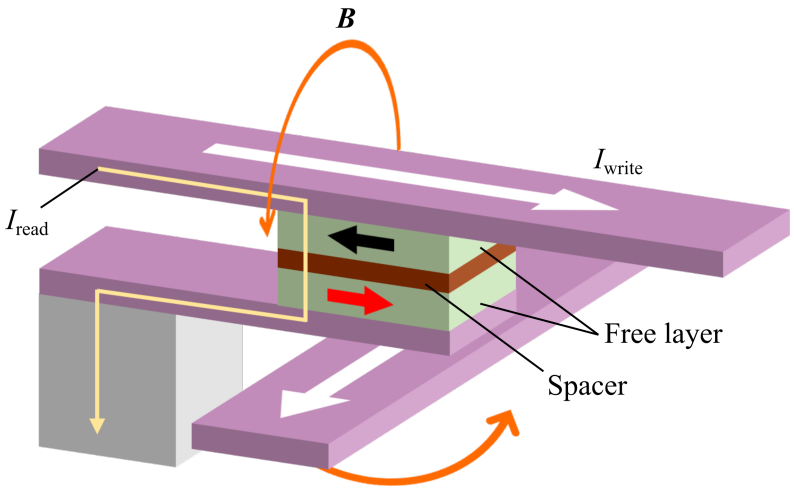

Figure 1.1: *Toggle-MRAM. A spin-valve or MTJ consisting of two free FM layers (green layers), separated by a non-magnetic spacer layer (brown layer), can be switched by magnetic fields (orange arrows) generated from writing currents, I_{write}, flowing through neighbouring write lines (white arrows). Switching is detected as a change in the GMR or TMR by a small read current, I_{read}, which is applied vertically through the stack.*

from their initial positions. Reversing the magnetization orientations causes the TMR to switch between a high and low resistive state which is assigned '1' and '0', respectively. Whilst toggle-MRAM has been employed commercially, its downsize scalability is hindered by electromigration in the write lines, limiting the MTJ width to a minimum of 100 nm. The use of magnetic fields for writing also prevents MTJs from being closely packed without the risk of impairing neighbouring devices.

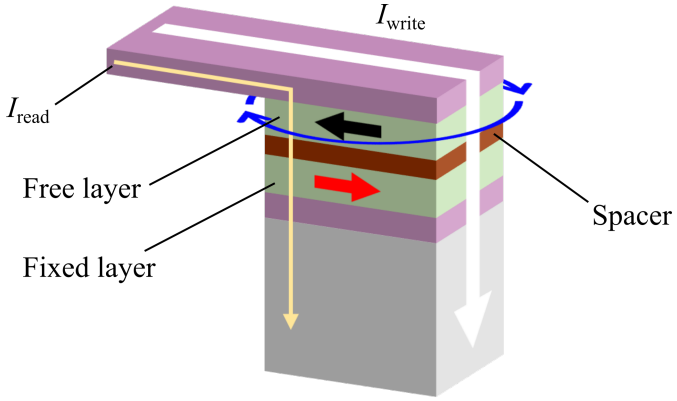

Figure 1.2: *STT-MRAM. Field-free method for switching the magnetization of a free FM layer in a spin-valve or MTJ. A writing current is applied vertically through the stack. The current is spin polarized, dependent on the polarity of the pulse, by the fixed FM layer and induces a STT on the free layer, rotating the magnetization (blue arrows) between two orientations. Both the read and write currents share the same path.*

Spin-transfer torque MRAM (STT-MRAM), on the other hand, does not use field-based writing methods [2–4]. Instead, a writing current applied vertically through the spin-

valve or MTJ stack is spin polarized by the fixed FM layer with polarization direction dependent on the current polarity. When the polarized current passes through the free FM layer the itinerant electrons transfer their spin angular momentum to the magnetic moments, generating a torque which reverses the magnetization. This method of writing is more efficient than the field-base method of toggle-MRAM because device sizes can be reduced and devices can be more densely packed without the risk of stray fields interfering with neighbours. The basic concept of an STT-MRAM device is shown in Figure 1.2.

The most recent generation of MRAM, shown in Figure 1.3, is based on relativistic spin-orbit torque (SOT-MRAM, also called three terminal MRAM) [3, 4, 6, 7]. The writing current polarization occurs due to broken spatial symmetry and spin-orbit coupling in the bulk FM free layer of an MTJ (Dresselhaus effect) or at the interface with the spacer layer (Rashba effect). It is also possible to inject a spin current in the MTJ from an adjacent non-magnetic heavy metal layer (spin Hall effect). Note that all effects originate from spin-orbit coupling. The spin polarization depends only on the direction of the writing current and not on the MTJ magnetization. As such, the torque induced on the magnetization of the FM free layer by the spin polarized current is field-like (and a mix of field-like and damping-like for the spin current injected from the heavy metal layer). This mechanism allows decoupled write and read paths (three-terminal) which improves the speed of SOT-MRAM compared to STT-MRAM.

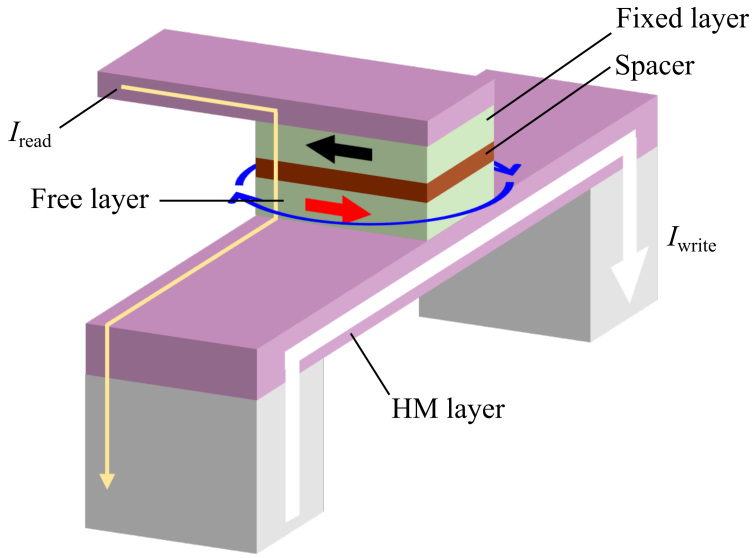

Figure 1.3: *SOT-MRAM. The write current is applied through a HM layer, which generates a spin current via the spin Hall effect. This is injected into the neighbouring free FM layer of a spin-valve or MTJ and induces a spin-orbit torque which switches the free layer magnetization. Reading and writing is done between three terminals as shown.*

In the pursuit of developing more efficient MRAMs, antiferromagnets (AFs) stand out as candidate materials [6, 8–10]. The absence of a stray field prevents stored information from being disturbed by external magnetic fields. It allows independent devices to be packed closely together without the risk of device cross-talk. Furthermore, the intrinsically strong AF coupling between neighbouring magnetic moments results in an exchange enhanced increase of the spin dynamic frequencies by an order of magnitude, from the GHz regime in FMs to THz in AFs [9, 11]. This enables orders of magnitude faster read and write speeds in AF-based MRAM compared to their FM counterparts.
So far, the primary magnetic components in MRAMs are FM materials. AF materials are most often used as secondary components to pin the fixed FM layer, or to act as the reference layer. This is largely because the antiparallel alignment of neighbouring magnetic moments in AFs produces zero net magnetization making them difficult to manipulate with external magnetic fields. It is possible to exchange couple a thin AF layer to an adjacent FM layer, so that rotating the FM magnetization with an external magnetic field drags the AF moments via the interfacial exchange spring mechanism, but this method suffers from the same downsides as toggle-MRAM and does not exploit the full potential of AF dynamics. As a solution, the all-electrical read and write methods used in STT-MRAM and SOT-MRAM (although slightly modified) offers a much more efficient way to control AF devices [6, 7].
There has been a swathe of preliminary work looking at current-induced STT and SOT switching in AF materials, a detailed overview of which is given in Chapter 3. The material central to recent developments, and the focus of this thesis, is the tetragonal phase of CuMnAs, a semimetal AF with the required crystal symmetry to host current-induced Néel-order spin-orbit torques [12, 13]. While preceding work demonstrated the switching of AF domains using relatively low current density pulses, a thorough understanding of the underlying switching mechanism is lacking. This thesis attempts to fill some of the gaps by exploring current-induced phenomena in the electrical transport properties of tetragonal CuMnAs epilayers, as well as resolving changes to the AF domain structure using magnetic imaging technique X-ray magnetic linear dichroism combined with photoemission electron microscopy (XMLD-PEEM).
The structure of this thesis. In the following chapter (Chapter 2) an introduction to the basic physics of antiferromagnets and spintronic phenomena is given. Then a review

of the recent literature focusing on the experimental study of the electrical switching of AFs via STT and SOT is given in Chapter 3. This leads on to the demonstration of current-induced high magnetoresistive switching in Chapter 4 and the characterization of the temperature and sample-dependent signal relaxation. Combined electrical pulsing and XMLD-PEEM imaging is presented in Chapters 5 and 6, where the control of 180° AF domain walls (Chapter 5) and AF vortices and antivortices (Chapter 6) is demonstrated. All of this work leads towards the development of AF materials for memory device applications, with conclusions of the main results and a brief outlook on the aims for future experiments (Chapter 7).

Chapter 2

Background

2.1 Properties of tetragonal CuMnAs

CuMnAs is an antiferromagnetic semimetal compound. In bulk material, the crystal structure is orthorhombic [14–16], meaning the lattice parameters $a \neq b \neq c$. When grown via molecular beam epitaxy (MBE) on III-V substrates, such as GaP(001) and GaAs(001), the CuMnAs crystal structure is tetragonal phase with lattice constants $a = b < c$ [15, 17]. In this case, the a and b, [100] and [010] axes, of the CuMnAs unit cell align along the half diagonal, [110] and [1-10] axes, of the substrate unit cell. There is $< 1\%$ mismatch between the CuMnAs a and b length and GaP(001) half diagonal which enables a fully strained growth of the CuMnAs layer up to thicknesses $\sim$130 nm. Larger, $\sim 5\%$, mismatch with the GaAs(001) half diagonal maintains strained growth for the first few monolayers before the CuMnAs layer phase relaxes, forming mosaic block structures [15].

Figure 2.1 shows the tetragonal CuMnAs unit cell. It is centrosymmetric with symmetry space group $P4/nmm$ [14, 18]. The Cu atoms (yellow) occupy symmetry related Wyckoff positions, $2a$, in the basal plane and the As (green) and Mn (purple) atoms occupy interstitial Wyckoff positions, $2c$. The lattice parameters measured for the relaxed material grown on GaAs are $a = b = 3.820$ Å and $c = 6.318$ Å [15].

The Mn atoms have a half filled $3d$ electron band. The electrons in the half-filled $3d$ band give rise to a magnetic moment, estimated from neutron diffraction experiments to be $3.6 \pm 0.2\,\mu_B$ at room temperature [15]. As shown in Figure 2.1, the Mn atoms form two magnetic sublattices which are aligned parallel in the ab plane and antiparallel (coupled

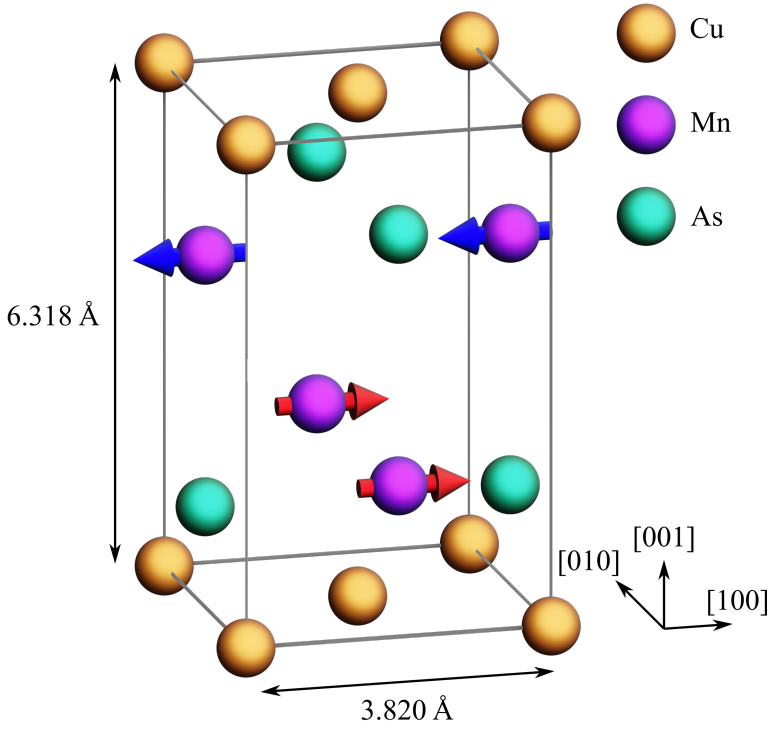

Figure 2.1: *Unit cell of tetragonal CuMnAs. The magnetic Mn atoms form collinear inversion partner sublattices, parallel in the crystal plane, and antiparallel out-of-plane.*

antiferromagnetically) perpendicular to the plane, in the c direction. This arrangement of magnetic atoms is called type A antiferromagnetic order [19].

Stoichiometric (even ratio of elements) orthorhombic and tetragonal CuMnAs have typical Néel temperatures of 312 K and 480 K [15, 17, 20], respectively. The effect of Cu $\rightarrow$ Mn substitution, away from stoichiometry, was explored in polycrystalline bulk material, revealing elevated Néel temperature for Mn rich tetragonal CuMnAs, and decreasing Néel temperature for increased Cu substitution [21]. Increasing the Mn concentration to $Cu_{0.82}Mn_{1.18}As$ stabilized a hexagonal crystal phase in bulk material, which was semiconducting with a reduced Néel temperature of 270 K [22]. Substitution of As atoms by Ge, Si, or Al is expected to induce perpendicular magnetic anisotropy in tetragonal CuMnAs [23].

The semimetal band structure of tetragonal CuMnAs is characterized by a very small overlap of the valence and conduction bands at high symmetry point, Γ, in the Brillouin zone, as well as a suppressed density of states at the Fermi energy level [12, 24]. This is different from a semiconductor, which has an energy gap separating the valence and conduction bands, and a Fermi level within the gap; and a metal, which has an appreciable density of states at the Fermi level due to a partially filled conduction band [19, 25]. The

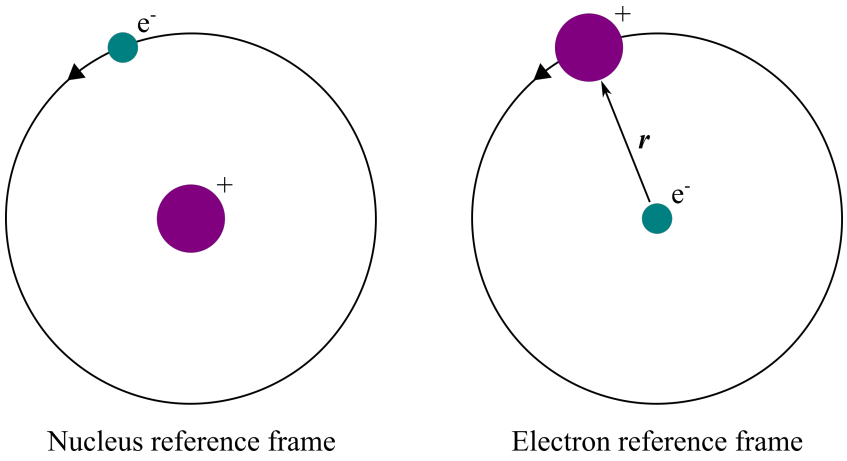

Figure 2.2: *Illustration of the intrinsic spin-orbit coupling. In the reference frame of the nucleus, the electron orbits, but transforming to the inertial frame of the electron, it is the nucleus which orbits.*

resistivity of tetragonal CuMnAs is 90 µΩ cm at 4 K and 160 µΩ cm at room temperature [15], increasing nearly linearly to an inflection point at the Néel temperature [20].

Both the orthorhombic and tetragonal phases of CuMnAs have been identified as candidate materials for spintronic applications. Orthorhombic CuMnAs hosts topologically protected Dirac quasiparticles [26–28]. Tetragonal CuMnAs has the required crystal symmetry for Néel spin-orbit torques (NSOTs) [10, 12], a method for electrically controlling the antiferromagnetic order, which is the focus of this thesis.

2.2 Spin-orbit coupling

Considering the simple picture shown in Figure 2.2, a Lorentz transformation from the nucleus reference frame to the orbiting electron reference frame yields an effective magnetic field experienced by the electron [19],

$$\boldsymbol{B} = \frac{\boldsymbol{E} \times \boldsymbol{v}}{c^2}, \tag{2.1}$$

where the radial vector, $\boldsymbol{E} = \frac{E}{\boldsymbol{r}}\hat{r}$, is the electric field at the electron due to the nucleus, $\boldsymbol{v}$ is the velocity of the nucleus relative to the electron, and c is the speed of light. Relating the effective magnetic field to the electron's orbital angular momentum, $\frac{\hbar}{m_e}\boldsymbol{L} = \boldsymbol{r} \times \boldsymbol{v}$, gives,

$$\boldsymbol{B} = \frac{E}{rc^2}\boldsymbol{L}. \tag{2.2}$$

The effective magnetic field interacts with the electron spin magnetic moment, $\boldsymbol{\mu}$, contributing an energy term to the Hamiltonian,

$$H_{\mathrm{SOC}} = -\frac{1}{2}\boldsymbol{\mu} \cdot \boldsymbol{B} = \frac{g\mu_{\mathrm{B}}E}{2\hbar r c^2}\boldsymbol{S} \cdot \boldsymbol{L}, \tag{2.3}$$

where the electron's magnetic moment, $\boldsymbol{\mu} = \frac{g\mu_{\mathrm{B}}}{\hbar}\boldsymbol{S}$, is related to its spin by the Landé g-factor, g, and the Bohr magneton, μ_{B}. The Hamiltonian is scaled by a factor of 1/2 due to the relativistic correction known as the Thomas half [29]. This interaction between the electron's orbital angular momentum and spin is called spin-orbit coupling and is not necessarily constrained to an electron orbiting a nucleus. For example, an electron moving through a crystal experiences a periodic electric potential, called the crystal field, due to localized atoms in a periodic lattice, which, in the presence of spatial symmetry breaking, can generate an effective spin-orbit coupling [19, 30, 31]. This gives rise to a plethora of interesting spintronic phenomena, some of which are considered in the following sections.

2.3 Magnetic anisotropy

Magnetic moments of electrons in a crystal have a preference to align along certain crystallographic directions, called easy axes, whereas energetically unfavourable directions are called hard axes. The temperature dependent energy difference between easy and hard axis alignment of the magnetic moments is the magnetic anisotropy energy, given by,

$$E_{\mathrm{ani}} = E_{\mathrm{hard}} - E_{\mathrm{easy}}. \tag{2.4}$$

The magnetic anisotropy can originate from several different effects, the main contributors in antiferromagnetic thin films being magnetocrystalline anisotropy, surface anisotropy, shape anisotropy and magnetostriction. These effects are also present in ferromagnetic materials, but the role of shape anisotropy is phenomenologically different; stray fields at the sample edges introduce a demagnetization energy (also called magnetostatic energy) that is minimized by the perpendicular alignment of domains to the edge normal [31, 32].

Understanding magnetic anisotropy is important for device applications because information can be encoded in the relative orientation of the magnetic moments. Non-volatile

magnetic memory, therefore, requires large enough magnetic anisotropy that thermal fluctuations do not erase the information, but not so large that it becomes energetically costly to write information.

2.3.1 Magnetocrystalline anisotropy

Magnetocrystalline anisotropy is caused by spin-orbit coupling and crystal symmetry. The symmetry of the crystal is imprinted onto the electron orbitals by lifting their degeneracy. The orbital angular momentum of the electron couples with its spin (and magnetic moment), thus mediating the influence of the crystal symmetry on the preferred orientation of the magnetic moment.

If the magnetic moments attempt to rotate away from their preferred orientation, for example, due to an external magnetic field, spin-orbit coupling induces an attempted reorientation of the electron orbital angular momentum. However, the orbit-lattice coupling is much stronger than the spin-orbit coupling and instead the magnetic moments will only rotate when the Zeeman energy from the field exceeds the spin-orbit coupling energy. The magnetocrystalline anisotropy energy is, thus, given by the spin-orbit coupling energy barrier [33–35],

$$\Delta H_{\mathrm{SOC}} = \frac{g\mu_{\mathrm{B}}E}{2\hbar rc^2}[\langle \boldsymbol{S}\cdot\boldsymbol{L}\rangle_{\mathrm{hard}} - \langle \boldsymbol{S}\cdot\boldsymbol{L}\rangle_{\mathrm{easy}}], \tag{2.5}$$

which is the difference in energy between the magnetic moment oriented along the hard and easy axes. In Bruno's model, the magnetocrystalline anisotropy energy is related to the orbital moment anisotropy through second order perturbation theory [33],

$$\Delta H_{\mathrm{SOC}} = \frac{gE}{8\hbar rc^2}[\mu_L^{\mathrm{easy}} - \mu_L^{\mathrm{hard}}], \tag{2.6}$$

where μ_L is the orbital moment along a specified axis. Two important points are concluded from this model; the magnetic easy axis coincides with the maximum orbital moment direction; and the magnetocrystalline anisotropy is expected to be small in the bulk of $3d$ transition metal crystals, because the close packed structure retains a high degree of symmetry (consequently, small energy splitting between d orbitals) [31]. This is the case for tetragonal CuMnAs, where the Mn $3d$ electrons give rise to the magnetic moment, and the in-plane anisotropy is small. The larger c-axis lattice parameter, on

the other hand, lifts the degeneracy of electron orbitals in that axis (electrons have more space to orbit without interacting). This leads to a large out-of-plane anisotropy, where in-plane alignment of the magnetic moments (through spin-orbit coupling) is preferred.

2.3.2 Surface and interfacial magnetic anisotropy

As mentioned in the previous section, Bruno's model suggests that, in the crystal bulk, the magnetocrystalline anisotropy energy is expected to be small due to the close packed structure. When the crystal symmetry is reduced, at a surface or interface for example, the orbital energy splitting will be enhanced compared to the bulk, leading to larger magnetocrystalline anisotropy energy (or surface anisotropy) [35].

At the crystal surface (interface with vacuum), out-of-plane electron orbitals (in-plane orbital moment) experience reduced electrostatic energy from the crystal field, thus favouring an in-plane spin moment through spin-orbit coupling [19, 31]. Likewise, at the interface between a crystal and another electronic medium, such as a substrate, the out-of-plane electron orbitals can hybridize leading to an enhancement of the perpendicular orbital anisotropy. The way in which the orbital anisotropy is enhanced depends on the hybridization mechanism taking place, so tuning interfacial interactions, via doping or oxidation, can result in in-plane or out-of-plane magnetic moment orientation.

Interplay between surface anisotropy, magnetocrystalline anisotropy in the bulk, and exchange coupling can lead to interesting magnetic phenomena, where competing spin and orbital moments settle with magnetic moments in a canted state, stabilizing chiral and helical magnetic structures.

2.3.3 Uniaxial anisotropy

Crystals with a single axis of high symmetry are called uniaxial and have an anisotropy energy of the form [19],

$$H_{\mathrm{u}} = K_0 + K_1 \sin^2\theta + K_2 \sin^4\theta + K_3 \sin^2\theta \cos 4\phi \ldots, \tag{2.7}$$

ignoring higher order terms, which are usually much smaller in magnitude. K_n are energy densities, called anisotropy constants, and K_0 is typically omitted because it is just a scalar offset. In the basis shown in Figure 2.3a, θ and ϕ are the polar and azimuthal angles of the magnetization with respect to the symmetry axis. Uniaxial

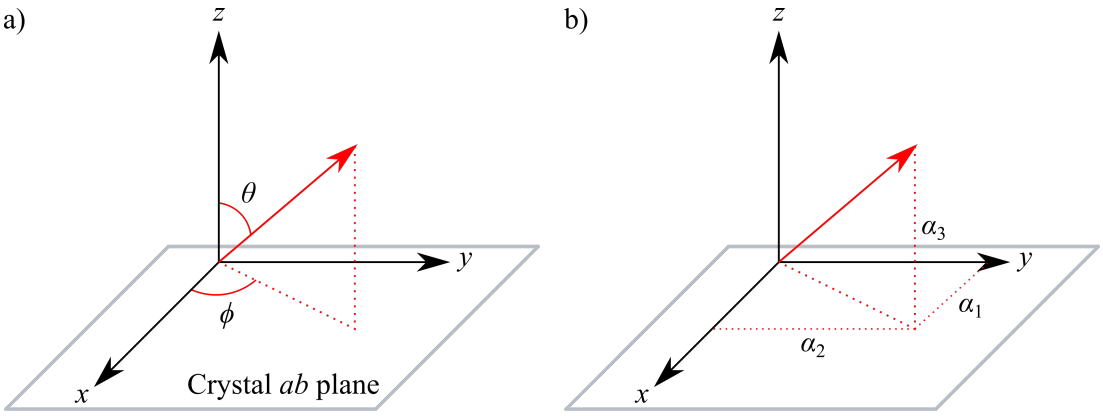

Figure 2.3: *Basis for describing the magnetic anisotropy. a) uniaxial anisotropy is compactly formulated in terms of the azimuthal, ϕ, and polar, θ, angles with respect to the crystal plane. b) cubic anisotropy is more appropriately expanded in terms of the cosine directions, α_n, with respect to the crystal axes.*

anisotropy is present in $L1_0$ phase crystals, such as FePt [36, 37] and CoPt [38], and in hexagonal crystals, such as hcp Co [39, 40].

Considering only the $K_{1,2}$ terms, if $K_{1,2} > 0$, the uniaxial anisotropy energy is minimized when $\theta = 0, \pi$, i.e., the magnetization lies parallel to the high symmetry axis. For $K_{1,2} < 0$, the energy is minimized when $\theta = \pm\frac{\pi}{2}$, which creates an easy plane of magnetization, perpendicular to the axis of high symmetry. More complicated situations, such as an easy cone, arise when K_1 and K_2 are opposite sign [31].

If the K_3 term is present and considerable, there exists a 4-fold symmetric planar contribution, $\cos 4\phi$, which, depending on the sign of K_3, aligns the magnetization along the in-plane crystal axes, or at 45° to them.

2.3.4 Cubic anisotropy

Some crystals have more than one axis of high symmetry, such as bcc Fe and fcc Ni. They possess a cubic anisotropy energy most compactly written in terms of the direction cosines, α_n, of the magnetization with respect to the Cartesian axes [31], as depicted in Figure 2.3b,

$$H_c = K_0 + K_1(\alpha_1^2\alpha_2^2 + \alpha_2^2\alpha_3^2 + \alpha_3^2\alpha_1^2) + K_2(\alpha_1^2\alpha_2^2\alpha_3^2)\ldots. \tag{2.8}$$

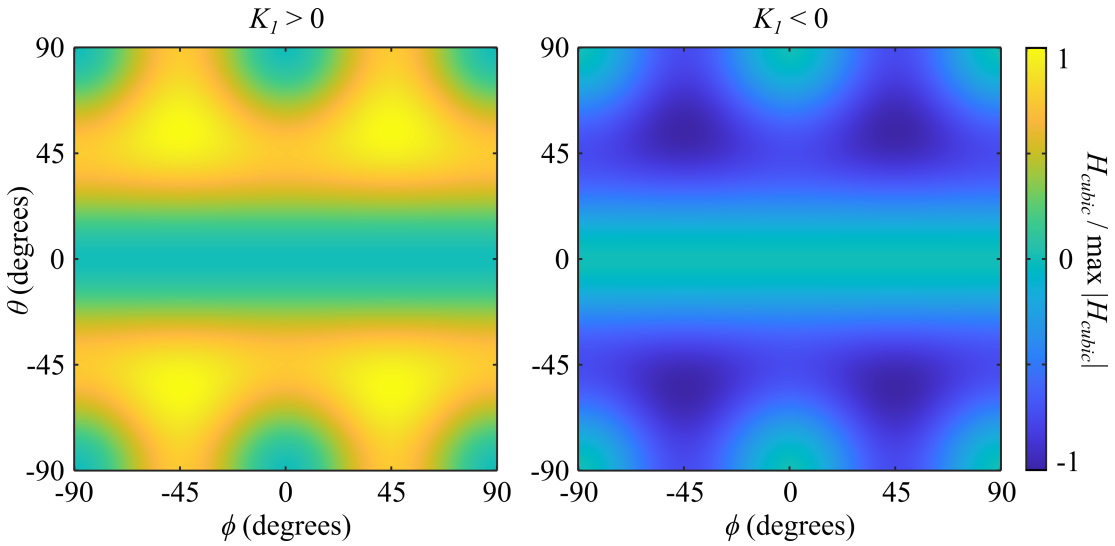

Figure 2.4: *Energy map of the cubic anisotropy as a function of the magnetization vector azimuthal, ϕ, and polar, theta angles for $K_2 = 0$ and $K_1 > 0$ (left) and $K_1 < 0$ (right). Low energy regions correspond to the magnetic easy axes, along which the magnetization preferentially aligns.*

This can be written in terms of the polar and azimuthal angles, where higher order terms are omitted [19],

$$H_c = K_0 + K_1 \left(\frac{1}{4} \sin^2\theta \sin^2 2\phi + \cos^2\theta \right) + \frac{K_2}{16} \sin^2 2\phi \sin^2 2\theta \sin^2\theta \ldots . \tag{2.9}$$

If $K_1 > 0$ and $K_2 = 0$, such as in bcc Fe, the cubic anisotropy energy is minimized given the following circumstances: $\theta = 0, \pi$, which is the uniaxial case with easy axis along the c direction; and $\theta = \pm\frac{\pi}{2}$, $\phi = 0, \pm\frac{\pi}{2}, \pi$, called the biaxial case because there are two orthogonal in-plane easy axes, along the a and b directions. When $K_1 < 0$ and $K_2 = 0$, such as in bcc Ni, the anisotropy energy is minimized for $\theta, \phi = \pm\frac{\pi}{4}, \pm\frac{3\pi}{4}$, corresponding to easy axes along the cubic diagonals. Figure 2.4 shows energy maps as functions of θ and ϕ for the two scenarios, $K_1 > 0$ and $K_1 < 0$ with $K_2 = 0$.

In most systems the cubic anisotropy is very small, because the crystal symmetry is very high, and as discussed in subsection 2.3.1, high symmetry results in small energy splitting between the electron orbitals.

2.4 Equilibrium domain structure in CuMnAs

Magnetic domains are macroscopic regions of homogenous magnetization preferentially pointing along the magnetic easy axes. In a ferromagnet the equilibrium domain structure typically consists of multiple domains, oriented with respect to one another in a

way that minimizes their demagnetization energy, arising from long-range dipole interactions. This is called the closure domain structure.

The boundaries between domains of different orientation are called domain walls, classified by the angle the magnetic moments subtend in the direction of the domain wall width. The two most common types are 90° and 180° domain walls. 180° domain walls can be characterized further: if the magnetic moments rotate about the normal of the domain wall (direction of the width) it is called a Bloch wall; and if the rotation is in the plane of the domain wall normal, it is called a Néel wall.

Due to the rotation of the magnetic moments inside the domain wall, positive energy contributions from exchange coupling, E_{ex}, and magnetic anisotropy, E_{ani}, determine the domain wall energy,

$$E_{\text{DW}} \propto \sqrt{E_{\text{ex}} E_{\text{ani}}}. \tag{2.10}$$

This leads to an expression for the domain wall width,

$$\delta \propto \sqrt{\frac{E_{\text{ex}}}{E_{\text{ani}}}}, \tag{2.11}$$

a competition between the exchange coupling which reduces the rotation between neighbouring spins and the magnetic anisotropy which fixes spins along an easy axis.

In AFs, the mechanism for domain equilibration occurs in the absence of demagnetization fields [41, 42]. As briefly mentioned in section 2.3.3, interfaces can introduce uniaxial anisotropy in a magnetic layer through hybridization of electron orbitals. However, epitaxially grown layers also experience magnetostriction from lattice mismatch at the interface with the substrate. In the absence of demagnetization fields, magnetostriction plays a significant role in establishing the equilibrium domain structure in AFs. Conventionally, antiferromagnetic domains aligned antiparallel are called translational domains and perpendicular domains are called orientational.

Due to spin-orbit coupling, the crystal structure exhibits a spontaneous deformation when transitioning from a paramagnetic to an antiferromagnetic state [41, 42]. The deformation induced strain, $\hat{u}_{\text{s}} \propto \boldsymbol{L} \otimes \boldsymbol{L}$, is a long-range effect and is a function of the Néel vector, $\boldsymbol{L}$. The strain modifies the crystal symmetry and, through spin-orbit coupling, the magnetocrystalline anisotropy - enhancing the uniaxial anisotropy.

Magnetostrictive deformation of the crystal structure causes incompatibility of strains,

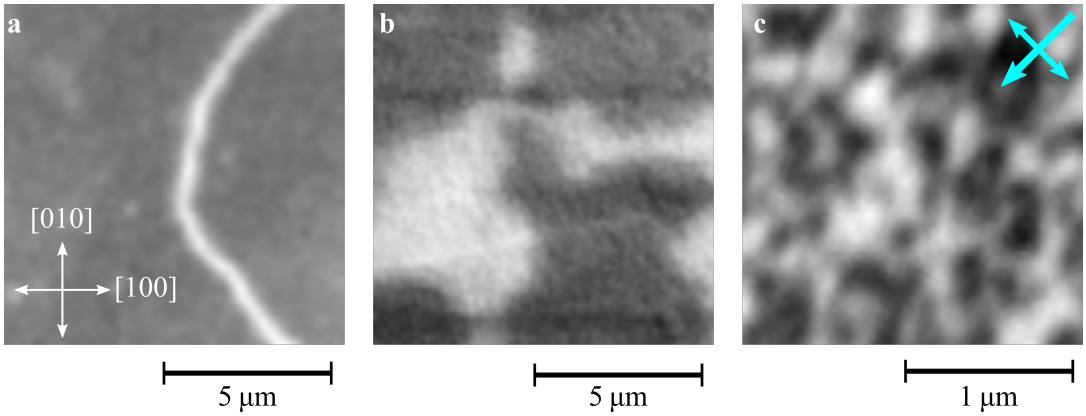

Figure 2.5: *XMLD-PEEM images revealing the AF domain structure in three CuMnAs layers. a)* 20 nm *CuMnAs, epitaxially grown on GaP(001), b)* 50 nm *CuMnAs, epitaxially grown on GaP(001), c)* 80 nm *CuMnAs, epitaxially grown on GaAs(001). The CuMnAs crystal axes, shown in a) are the same for all three samples. The linearly polarized x-rays are incident along the [-1-10] direction, with polarization vector collinear to the [1-10]. Black and white contrast results from Néel vector orientations, in the domains and domain walls, aligned parallel, perpendicular to the x-ray polarization, respectively. Grey contrast, seen in the domains of a) are are Néel vector alignments collinear to the [100] or [010].*

called plastic strains, between the antiferromagnetic epilayer and the substrate [43]. This introduces a destressing energy, analogous to the demagnetization energy in ferromagnets, which is minimized by an even distribution of orientational domains.

Additionally, there is an incompatibility of strains between orientational domains, which determines the phenomenology of the domain walls at their boundaries [43]. Minimization of the domain wall length occurs for directions intermediate to the perpendicular strain vectors of the orientational domains. In biaxial epilayers of tetragonal CuMnAs, for example, the Néel vector of the domains is along the [110] and [1-10] CuMnAs crystal axes and the 90° domain walls form flat along the intermediate, [100] and [010] axes.

In CuMnAs layers <20 nm, grown on GaP(001), the constrictive strains at the interface with the substrate strongly enhance the uniaxial magnetic anisotropy, giving rise to large, >5 µm, domains oriented along the one of the principal, [100] or [010] CuMnAs axes, with 180° domain walls separating antiparallel neighbours. Increasing the CuMnAs layer thickness to ≥45 nm, leads to a large destressing energy and biaxial anisotropy, as described above. Typical domain size in these layers is 1 µm to 5 µm. Growing on GaAs(001) substrates results in a relaxed CuMnAs layer, which forms <1 µm domains with easy plane anisotropy. Figure 2.5 shows example XPEEM images of unpatterned regions in 20 nm (a) and 50 nm (b) layers grown on GaP(001), as well as an 80 nm layer grown on GaAs(001) (c). Note that these are generalized examples and factors, such as substrate surface quality and patterned shapes, have a significant impact on the

resulting CuMnAs domain morphologies. There have been several other examples of thicker layers, >45 nm, grown on GaP(001) with large uniaxial domains.

2.5 Magnetization dynamics

In the simple case of an electron spin in a uniform magnetic field, the energy of the spin is given by,

$$\hat{H} = \mu_{\mathrm{B}} \boldsymbol{S} \cdot \boldsymbol{B}, \tag{2.12}$$

where $\boldsymbol{S}$ is the electron's spin angular momentum (opposite to the electron's magnetic dipole moment) and $\boldsymbol{B}$ is the magnetic field vector. The dynamics of the spin are calculated from Ehrenfest's equation,

$$\frac{\partial \boldsymbol{S}}{\partial t} = \frac{1}{i\hbar}\langle [\hat{H}, \boldsymbol{S}] \rangle = \frac{g\mu_{\mathrm{B}}}{\hbar} \langle \boldsymbol{S} \rangle \times \boldsymbol{B}, \tag{2.13}$$

where $g\mu_{\mathrm{B}}/\hbar = \gamma$ is the gyromagnetic ratio, determining the sense in which the spin precesses around the magnetic field direction. For an isolated electron, whose spin and magnetic moments are antiparallel, $\gamma < 0$ and the precession of the spin is clockwise.
This equation of motion is extended, in the mean-field approach, to systems consisting of large numbers of spins by introducing the magnetization,

$$\boldsymbol{M} = \frac{\mu_{\mathrm{B}}}{V} \sum_i \boldsymbol{S}_i, \tag{2.14}$$

where V is volume over which the spins are integrated. Equation 2.13 becomes the Larmor precession equation,

$$\frac{\partial \boldsymbol{M}}{\partial t} = \gamma \mu_0 \boldsymbol{M} \times \boldsymbol{H}, \tag{2.15}$$

using $\boldsymbol{B} = \mu_0(\boldsymbol{H} + \boldsymbol{M})$, where μ_0 is the magnetic permeability in a vacuum.
In realistic magnetic systems, the interactions involved in the magnetization dynamics are far more complex than just an external magnetic field. As discussed in previous sections, magnetic materials have additional energy density terms,

$$W = \frac{A}{M_{\mathrm{s}}^2}(\nabla \boldsymbol{M})^2 + K(\boldsymbol{M} \cdot \boldsymbol{u})^2 - \frac{1}{2}\mu_0 \boldsymbol{M} \cdot \boldsymbol{H}_{\mathrm{d}} - \mu_0 \boldsymbol{M} \cdot \boldsymbol{H}, \tag{2.16}$$

where the first term in the sum corresponds to the exchange interaction, the second to the

magnetic anisotropy, the third to the demagnetization energy due to dipole interactions (present in ferro- and ferrimagnets, and only in AFs with canted magnetic moments), and the final term is the Zeeman energy. These contributions enter the Larmor precession equation in the form of a thermodynamic force which acts like an effective magnetic field,

$$\boldsymbol{H}_{\text{eff}} = -\frac{1}{\mu_0}\frac{\partial W}{\partial \boldsymbol{M}}, \tag{2.17}$$

giving the field-like term in the Landua-Lifshitz equation,

$$\frac{\partial \boldsymbol{M}}{\partial t} = -\gamma \boldsymbol{M} \times \frac{\partial W}{\partial \boldsymbol{M}}. \tag{2.18}$$

Under time reversal this equation is symmetric and the system conserves energy, resulting in a persistent precession of the magnetization about the effective magnetic field direction. To accommodate for dissipation of the precessional energy, a damping term, which is antisymmetric in time, must be included,

$$\frac{\partial \boldsymbol{M}}{\partial t} = -\gamma_0 \boldsymbol{M} \times \boldsymbol{H}_{\text{eff}} + \frac{\alpha}{M_{\text{s}}} \boldsymbol{M} \times \frac{\partial \boldsymbol{M}}{\partial t}. \tag{2.19}$$

The first term on the right hand side is the field-like term from Equation 2.18 given in terms of the effective magnetic field, where $\gamma_0 = \gamma\mu_0$. The second term, with damping coefficient, α, is the Gilbert damping term, which takes the form of a torque that acts to align the magnetization with the effective magnetic field. This equation of motion is called the Landau-Lifshitz-Gilbert (LLG) equation.

Equation 2.19 is extended to antiferromagnetic systems by considering the two sublattice model with oppositely aligned magnetizations, $\boldsymbol{M}^A$ and $\boldsymbol{M}^B$ [25, 44–46]. The dynamics of the sublattice magnetizations are described by two LLG equations,

$$\begin{cases} \partial_t \boldsymbol{M}^A = -\gamma_0 \boldsymbol{M}^A \times \boldsymbol{H}_{\text{eff}} + \frac{\alpha}{M_{\text{s}}} \boldsymbol{M}^A \times \partial_t \boldsymbol{M}^A - \gamma_0 \boldsymbol{M}^A \times \boldsymbol{H}^A_{\text{ex}} \\ \partial_t \boldsymbol{M}^B = -\gamma_0 \boldsymbol{M}^B \times \boldsymbol{H}_{\text{eff}} + \frac{\alpha}{M_{\text{s}}} \boldsymbol{M}^B \times \partial_t \boldsymbol{M}^B - \gamma_0 \boldsymbol{M}^B \times \boldsymbol{H}^B_{\text{ex}}, \end{cases} \tag{2.20}$$

with the addition of the final term, the homogeneous exchange, $\boldsymbol{H}^{A,B}_{\text{ex}} = \lambda \boldsymbol{M}^{B,A}$, coupling the two sublattices antiferromagnetically (given the exchange parameter, $\lambda > 0$) [44, 47, 48].

Inclusion of the antiferromagnetic inter-sublattice exchange in the coupled LLG equa-

tions leads to an enhancement of the antiferromagnetic resonance frequency by a factor of $\sqrt{H_{\text{ex}}/H_{\text{ani}}}$, where H_{ani} is the magnetic anisotropy field [49, 50]. The resonant frequency is shifted to the THz regime, compared to GHz in ferromagnets.

Pertinent to spintronics is the control of the magnetization (or sublattice magnetizations) using an external magnetic field or spin-polarized current. Whilst an external magnetic field is efficient for manipulating the magnetization of a ferromagnet, it can be seen from the coupled equations in 2.20 that a uniform field produces opposite torques on the two magnetic sublattices, which compensate each other ($\boldsymbol{M}^A = -\boldsymbol{M}^B$, so that $\boldsymbol{M}^A \times \boldsymbol{H} = -\boldsymbol{M}^B \times \boldsymbol{H}$). On the other hand, current-induced spin-transfer torque (STT), originating from the exchange coupling of spin-polarized electrons with the magnetic moments, can rotate the magnetization in ferromagnets between stable states [10, 49]. In AFs, STT also efficiently manipulates the sublattice magnetizations, but their antiparallel alignment keeps them in a precessional state about the polarization vector. This is often called antidamping torque as it opposes the damping torque that dissipates the precessional energy.

Another form of current-induced spin-torque is spin-orbit torque [7, 51].

2.6 Dresselhaus and Rashba spin-orbit coupling

The spin-orbit coupling Hamiltonian, shown in Equation 2.3, describes an electron orbiting a nucleus with a spherical electric potential. In a crystal, this is an adequate description only for electrons localized around the nuclei. There is another contribution to the electric potential experienced by the electron, called the crystal field, which is a consequence of the close packed structure and crystal symmetry. The spin-orbit coupling Hamiltonian is more appropriately expressed as [6, 52, 53],

$$H_{\text{SOC}} = -\frac{g\mu_{\text{B}}}{2c^2}\boldsymbol{\sigma} \cdot (\boldsymbol{E} \times \boldsymbol{v}) = \frac{g\mu_{\text{B}}}{2mc^2}\boldsymbol{\sigma} \cdot (\nabla V \times \boldsymbol{p}) = \boldsymbol{\sigma} \cdot \boldsymbol{U}(\boldsymbol{p}), \tag{2.21}$$

where $\boldsymbol{\sigma}$ is the electron spin in terms of the Pauli matrices, and $\boldsymbol{U}(\boldsymbol{p}) = \frac{g\mu_{\text{B}}}{2mc^2}(\nabla V \times \boldsymbol{p})$ is the spin-orbit field in terms of the gradient of the electric potential, ∇V, (including the spherical potential and the crystal field) and the electron momentum, $\boldsymbol{p}$, and mass, m.

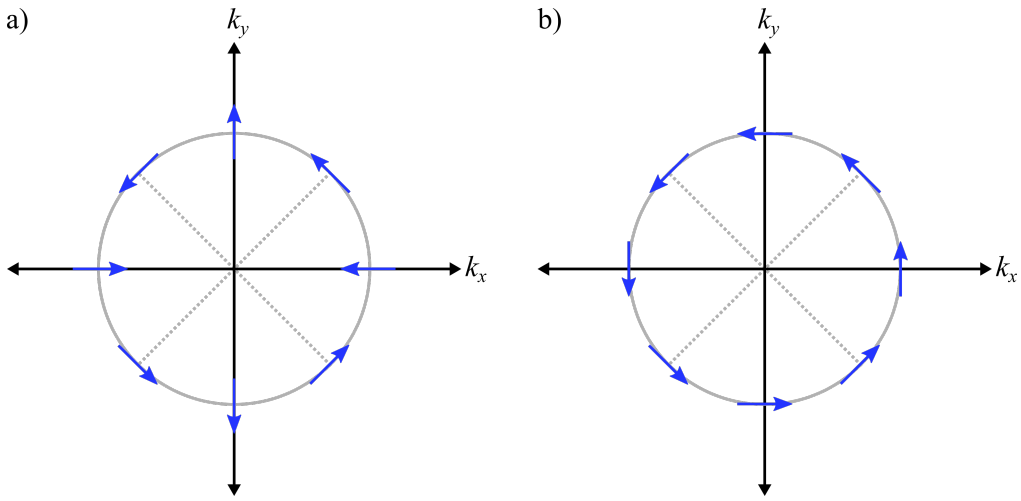

Figure 2.6: *Illustrations of the momentum dependent spin polarization at the Fermi surface due to a) Dresselhaus, and b) Rashba, spin-orbit coupling.*

Spin-orbit coupling preserves time reversal symmetry [52],

$$\begin{aligned} T &: H_{\mathrm{SOC}} = H_{\mathrm{SOC}}, \\ T &: \boldsymbol{\sigma} \cdot \boldsymbol{U}(\boldsymbol{p}) \rightarrow -\boldsymbol{\sigma} \cdot \boldsymbol{U}(-\boldsymbol{p}), \\ \therefore & -\boldsymbol{\sigma} \cdot \boldsymbol{U}(-\boldsymbol{p}) = \boldsymbol{\sigma} \cdot \boldsymbol{U}(\boldsymbol{p}), \end{aligned}$$

which holds if the spin-orbit field vanishes, $\boldsymbol{U}(\boldsymbol{p})$, or the spin-orbit field is an odd function of momentum, $\boldsymbol{U}(-\boldsymbol{p}) = -\boldsymbol{U}(\boldsymbol{p})$. It has been shown that the latter scenario only survives in crystal structures with broken spatial inversion symmetry [6].

Two types of broken spatial inversion symmetry are: structural and bulk inversion asymmetry, which gives rise to Rashba [54–56] and Dresselhaus [57] spin-orbit coupling, respectively. Structural inversion asymmetry requires an atomic site with point group symmetry that leaves a single direction invariant under all symmetry operations (polar), whereas bulk inversion asymmetry requires no invariant direction under all symmetry operations (non-polar) [58, 59].

The linear form of the Dresselhaus spin-orbit coupling, resulting from bulk inversion asymmetry, is given by [6, 57],

$$H_{\mathrm{D}} = \frac{\beta}{\hbar}(p_x\sigma_x - p_y\sigma_y), \tag{2.22}$$

where β is the coupling constant, which can be positive or negative. The electron's linear momentum is coupled to its spin, and the energy bands are spin split in momentum

space. An illustration of the Dresselhaus spin texture at the Fermi surface in the k_{xy} plane is shown in Figure 2.6a. This type of spin-orbit coupling is present in zinc-blende crystal structures that are lacking a centre of inversion symmetry.

The origin of Rashba spin-orbit coupling is conceptualized by considering an electron moving through an electric field, $\boldsymbol{E} = -E_0\hat{z}$, which breaks the spatial symmetry of the system. This generates a spin-orbit field, in the electron's reference frame, which couples to its spin, giving the Rashba spin-orbit coupling term [54, 56],

$$H_{\mathrm{R}} = \frac{g\mu_{\mathrm{B}}}{2mc^2}\boldsymbol{\sigma}\cdot(E_0\hat{z}\times\boldsymbol{p}) = \alpha_{\mathrm{R}}(\sigma_x p_y\hat{x} - \sigma_y p_x\hat{y}), \tag{2.23}$$

where $\alpha_{\mathrm{R}} = g\mu_{\mathrm{B}}E_0/(2mc^2)$ is the Rashba coefficient. This type of spin-orbit coupling is present in crystals with polar symmetry, such as wurtzite structures, and in low-dimensional systems, such as at surfaces and interfaces in heterostructures. The produced spin texture at the Fermi surface is illustrated in Figure 2.6b; the electron's spin is always perpendicular to the direction of momentum.

Both Rashba and Dresselhaus spin-orbit coupling cause spin polarization. For example, the Rashba-Edelstein effect, also called the inverse spin galvanic effect, occurs when a charge current flows through a system with Rashba spin-orbit coupling [60, 61]. The Fermi surface shifts in momentum space, resulting in a non-equilibrium redistribution of spins, so that a non-polarized current becomes polarized with spin perpendicular to the current direction. This mechanism is key to the electrical control of the antiferromagnetic order in tetragonal CuMnAs, although with some additional subtleties [12].

2.6.1 Hidden Rashba spin-orbit coupling

The common conception when looking for systems hosting Dresselhaus and Rashba spin-orbit coupling is that the bulk symmetry (space group symmetry) must be broken. That is the case in materials that exhibit a net spin polarization of the type shown in Figure 2.6. However, consideration of the atomic site point groups leads to local environments with the required symmetry breaking for Dresselhaus and Rashba spin-orbit coupling, that can exist in systems with bulk centrosymmetry [59].

This is the case in tetragonal CuMnAs and Mn_2Au, with crystal symmetry space groups $P4/nmm$ and $I4/mmm$, respectively [12, 13, 62]. Both bulk crystal structures are

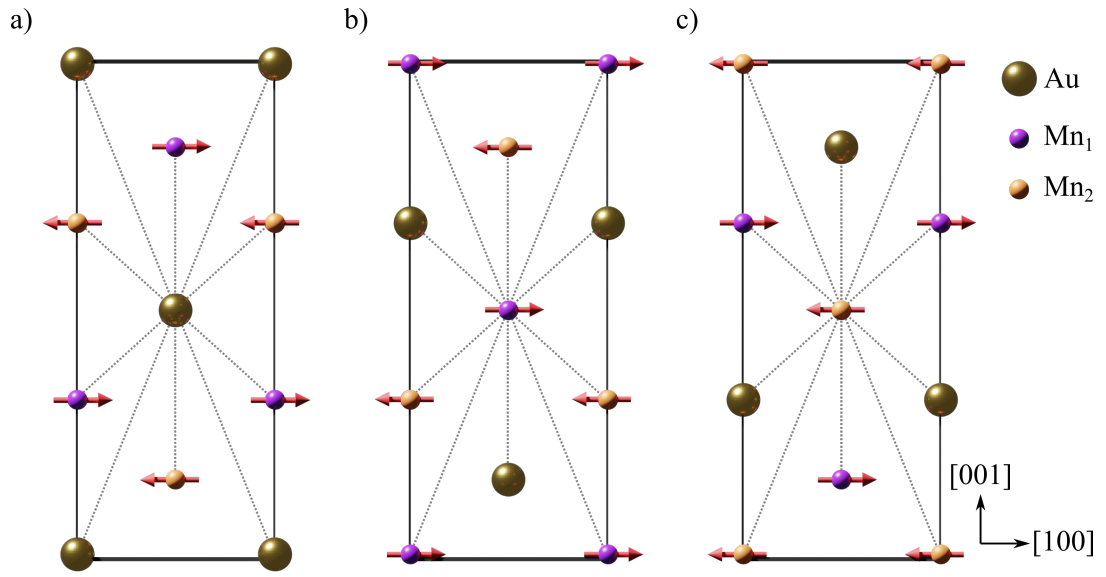

Figure 2.7: *Demonstration of atomic site point group symmetry breaking in centrosymmetric crystal Mn_2Au. a) shows the crystal unit cell with point of inversion symmetry at the central Au atom. Dashed lines illustrate, in this 2-dimensional view, the swapping of sites through inversion. Inversion through the Mn atomic site located on sublattice 1, b), and sublattice 2, c), retrieve a unit cell that is no longer self coincident. Thus the Mn atomic site point group symmetry is inversion asymmetric and the sublattices form inversion partners.*

centrosymmetric, but when the Mn sublattices are considered individually, their atomic site point group symmetry is non-centrosymmetric. This is illustrated in Figure 2.7, which shows the (010) plane of the Mn_2Au unit cell. The inversion centre coincides with the central Au atom in Figure 2.7a. Dashed lines link atomic sites that swap position when applying spatial inversion through the central atom. If the perspective is shifted so that a Mn atom is at the centre (purple for sublattice 1, and orange for sublattice 2), inversion no longer returns the original unit cell, as shown in Figure 2.7b and c. Resulting local asymmetric environments on each Mn sublattice give rise to Rashba spin-orbit coupling, which is compensated globally because the sublattices form inversion partners.

2.6.2 Néel-order spin-orbit torque

Figure 2.8 depicts a charge current polarized by the inverse spin galvanic effect on the Mn sublattices as it passes through the tetragonal CuMnAs unit cell. The non-equilibrium spin densities, oriented perpendicular to the current direction, have opposite sign on the two sublattices and compensate each other globally (shown by the red and blue arrows). The spin of the itinerant electrons exchange couples to the localized Mn

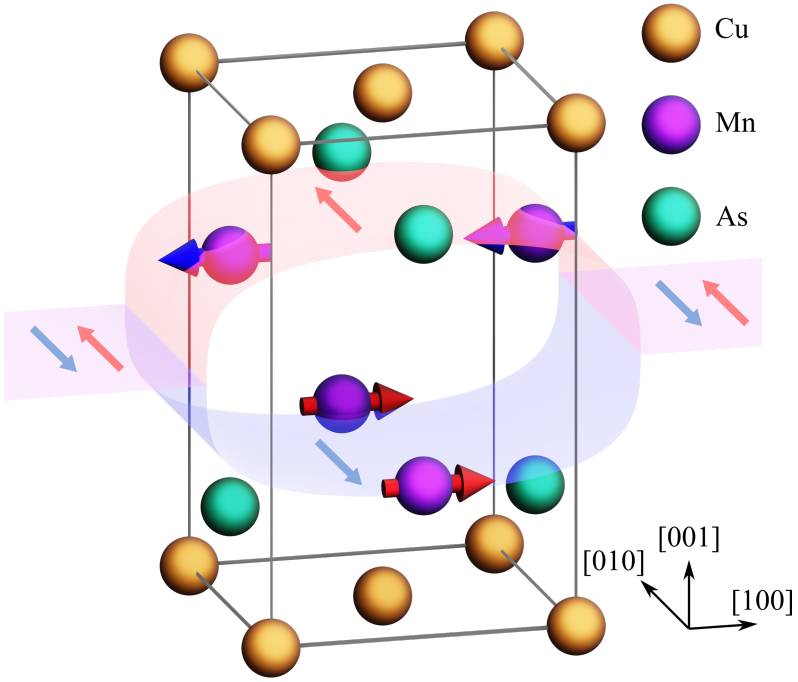

Figure 2.8: *A charge current (translucent planes) with no initial spin polarization flowing through the unit cell of tetragonal CuMnAs. Local Rashba spin-orbit coupling causes the current to spin split with opposite sign on the two Mn sublattices. Spin polarization exhibits Rashba-like texture with spins (red and blue arrows) directed perpendicular to the current direction.*

3*d* electrons (which are responsible for the magnetic moment), acting like an effective magnetic field in the direction of polarization (opposite sign on the Mn sublattices). Provided sufficient current density, the effective magnetic field induces a Néel-order spin-orbit torque (NSOT) on the Mn magnetic moments, rotating them, in the same sense on the two sublattices, perpendicular to the current direction [12]. This Néel-order torque is a (relativistic) spin-orbit torque because it arises from Rashba spin-orbit coupling induced spin polarization.

The current generated NSOT in CuMnAs (and Mn_2Au) has the field-like form [12],

$$\boldsymbol{T}_{A,B} \sim \boldsymbol{M}_{A,B} \times \boldsymbol{B}_{A,B}, \tag{2.24}$$

where $\boldsymbol{B}_A \sim +\hat{z} \times \boldsymbol{J}$ and $\boldsymbol{B}_B \sim -\hat{z} \times \boldsymbol{J}$ are the effective magnetic fields on the sublattices, related to the applied current density, $\boldsymbol{J}$. Thus, the antiparallel magnetizations, $\boldsymbol{M}_A = -\boldsymbol{M}_B$, experience equivalent torques, which rotate them in the same sense. The dynamics of the sublattice magnetizations are summarized in Figure 2.9, which shows the damped precessional motion of the magnetization vectors in the direction of the

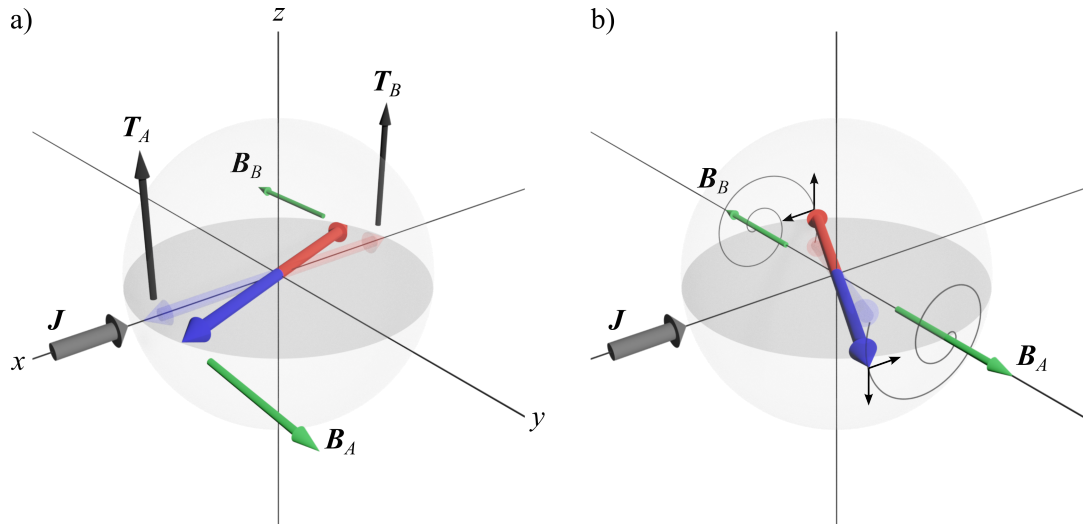

Figure 2.9: *Current-induced staggered effective fields, $\boldsymbol{B}_{A,B}$ (green arrows), generate a torque, $\boldsymbol{T}_{A,B}$ on the spin sublattices, A (blue) and B (red), a) rotating them perpendicular to the current direction, $\boldsymbol{J}$, and b) instigating damped precessional motion about the effective field directions.*

sublattice effective fields. As NSOTs are a function of the current direction, the Néel vector can be switched between orthogonal axes by applying perpendicular currents. Furthermore, the staggered effective magnetic field is an odd function of the current polarity.

2.7 Anisotropic magnetoresistance

Pertinent to the design of practical magnetic memory devices is an efficient method for detecting the reorientation of the magnetization. Spin-orbit coupling introduces intrinsic magnetoresistance effects where the ohmic resistance of the magnetic material depends on the angle between an applied electrical current, the magnetization direction, and the crystal axes [19, 25, 31].

Two coefficients of the magnetoresistance are the anomalous Hall effect (AHE) and the anisotropic magnetoresistance (AMR) [29]. The AHE is characterized by a transverse resistance induced by an out-of-plane magnetization. It is an odd function of the magnetization vector, $\rho_{\mathrm{T}}(\boldsymbol{M}) = -\rho_{\mathrm{T}}(-\boldsymbol{M})$, and is therefore not present in collinear AFs. Conversely, the anisotropic magnetoresistance is an even function of the magnetization vector, arbitrarily oriented, with longitudinal and transverse components,

$$\rho_{\mathrm{L}}(\boldsymbol{M}) = \rho_{\mathrm{L}}(-\boldsymbol{M}),$$

$$\rho_{\mathrm{T}}(\boldsymbol{M}) = \rho_{\mathrm{T}}(-\boldsymbol{M}),$$

and is, therefore, equally present in FMs and AFs.

The AMR has a non-crystalline part, originating from spin-orbit coupling mediated anisotropic scattering of s electrons, with light effective mass, into d states with heavy effective mass [63, 64]; and a crystalline part inherent to the symmetry of the crystal lattice (transport equivalent to magnetocrystalline anisotropy discussed in subsection 2.3.1) [29]. In systems with in-plane uniaxial and biaxial anisotropy, the longitudinal AMR is decomposed into four terms [65],

$$\frac{\Delta\rho_{xx}}{\bar{\rho}} = C_{\mathrm{I}}\cos 2\phi + C_{\mathrm{U}}\cos 2\psi + C_{\mathrm{C}}\cos 4\psi + C_{\mathrm{I,C}}\cos(4\psi - 2\phi), \tag{2.25}$$

where $\Delta\rho_{xx} = \rho_{xx} - \bar{\rho}$ given that,

$$\bar{\rho} = \int_0^{2\pi} \frac{\rho_{xx}}{2\pi}\mathrm{d}\phi, \tag{2.26}$$

is the average ρ_{xx} over the full set of angles, ϕ, in the plane between the magnetization vector, $\boldsymbol{M}$ (or Néel vector, $\boldsymbol{L}$), and the current, $\boldsymbol{I}$. The first term on the right-hand side of equation 2.25 is the non-crystalline term, coupling the itinerant electrons spins to the local magnetic moments. The second and third terms are the 2nd and 4th order crystalline terms, which are functions of the angle, ψ, between the magnetization vector (or Néel vector) and the [110] crystal axis. The final term is the crossed non-crystalline/crystalline term, coupling the itinerant electrons spins and orbital angular momentum to the crystal lattice and the local magnetic moments.

Purely crystalline terms are excluded through symmetry constraints from the transverse AMR,

$$\frac{\Delta\rho_{xy}}{\bar{\rho}} = C_{\mathrm{I}}\sin 2\phi + C_{\mathrm{I,C}}\sin(4\psi - 2\phi), \tag{2.27}$$

leaving just the non-crystalline and crossed non-crystalline/crystalline terms.

2.8 X-ray Magnetic Microscopy

The chemical and magnetic properties of a material can be spatially resolved using a combination of spectroscopy and microscopy [66]. An example of a powerful spectroscopy technique involves the absorption of x-rays (XAS) and subsequent liberation of bound core electrons to empty valence band states just above the Fermi level [67–69].

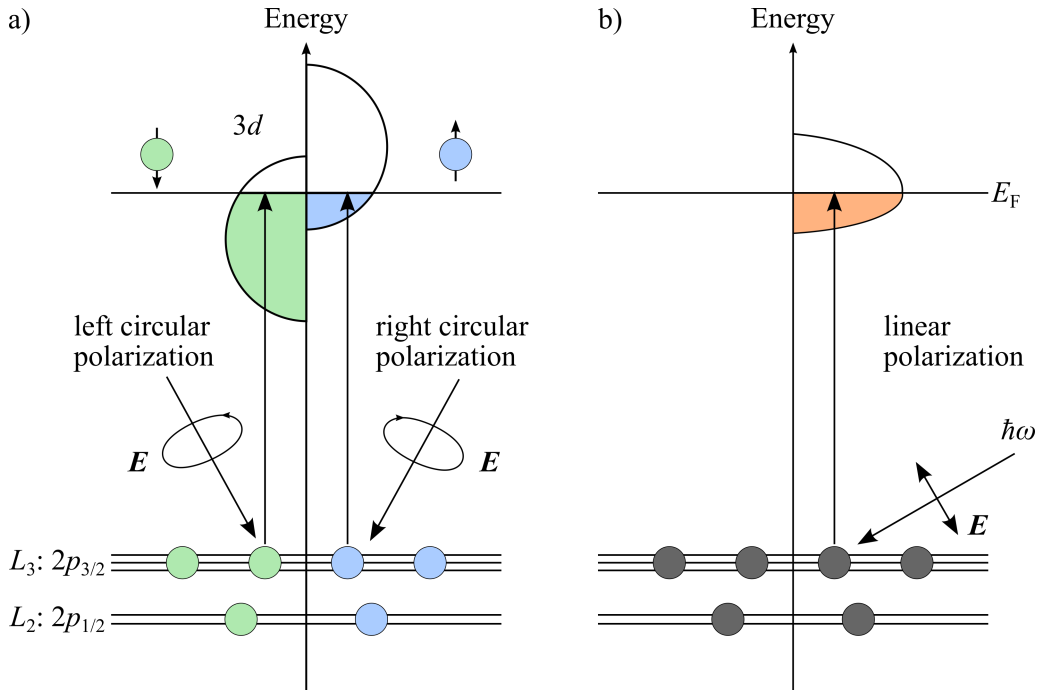

Figure 2.10: *Illustration of 2p to 3d electron orbital transitions instigated by a) circularly polarized x-ray absorption, and b) linearly polarized x-ray absorption.*

The transition of electrons between bands is governed by the selection rule, $\Delta l = \pm 1$, and the conservation of the electron spin, allowing for probing of the $2p \rightarrow 3d$ transition in $3d$ band transition metals, as well as the $3p \rightarrow 4f$ transition in rare earths [66–71]. At x-ray energies corresponding to the element specific binding energies of the core electrons, the absorption spectrum exhibits resonances, known as absorption peaks/edges. The $2p \rightarrow 3d$ transition has two absorption edges, L_2 and L_3, associated with the spin-orbit split, $J = 1/2$ and $J = 3/2$, hole states created in the $2p$ band, respectively. The degeneracy $(2J + 1)$ of the $J = 3/2$ state is twice that of the $J = 1/2$ state and so the L_3 absorption edge is twice the amplitude of the L_2 absorption edge.

2.8.1 X-ray Magnetic Circular Dichroism

Using polarized x-rays, magnetic properties of materials can be detected. Circularly polarized x-rays possess a rotating electric field vector, $\boldsymbol{E}$, around the direction of propagation, k. Depending on the rotation sense of $\boldsymbol{E}$, the photons are said to be right circularly polarized (anticlockwise about k), with $+\hbar$ angular momentum, or left circularly polarized (clockwise about k), with $-\hbar$ angular momentum. Transfer of angular momentum from the absorbed x-ray photon to a $2p$ electron is imparted to the electron spin through spin-orbit coupling [70, 71]. Opposite angular momentum of right and left

circularly polarized x-rays, therefore, induces photoelectrons (liberated electrons) with opposite spin. The photoelectron spin polarization is further mediated by the $J = 1/2$ and $J = 3/2$ states at the L_2 and L_3 absorption edges, which have opposite spin-orbit coupling ($l - s$ and $l + s$, respectively), and so produce photoelectrons with opposite spin polarization. In transition metals with an imbalance of spin-up and spin-down d band hole states, there is an asymmetry between the absorption spectra (called magnetic dichroism) measured for two different x-ray polarizations,

$$\Delta\mu = \frac{\mu_1 - \mu_2}{\mu_1 + \mu 2}, \tag{2.28}$$

where μ is the absorption coefficient and μ_1 and μ_2 are absorption coefficients of two different x-ray polarizations. Circularly polarized x-rays produce a dichroism that reveals magnetic information (XMCD) of systems with time-reversal symmetry breaking. This is not the case in AFs, but in ferro- and ferrimagnets where the symmetry is broken by the local magnetic moment. The absorption spectra varies a function of the XMCD,

$$I = I_0 + I_{\mathrm{XMCD}}, \tag{2.29}$$

given that,

$$I_{\mathrm{XMCD}} \propto \langle M \rangle \cos\theta, \tag{2.30}$$

where $\langle M \rangle$ is the expectation value of the local magnetic moment and θ is the angle between the moment and the photon angular momentum. The maximum XMCD is calculated by measuring the difference in absorption spectra for photon angular momentum parallel and antiparallel to the direction of the local magnetic moment.

2.8.2 X-ray Magnetic Linear Dichroism

Linearly polarized x-rays have a biaxial polarization vector with $\boldsymbol{E}$ oscillating in a plane along the direction of propagation. Perpendicular polarization vectors correspond to two types of linear polarization – horizontal, with $\boldsymbol{E}$ oscillating in a horizontal plane, and vertical, with $\boldsymbol{E}$ oscillating in a vertical plane. The absorption of linearly polarized x-rays is sensitive to the charge anisotropy of a material. This allows detection of the local magnetic anisotropy, in the x-ray magnetic linear dichroism (XMLD). Alignment of the local magnetic moments along a preferential axis creates a charge anisotropy due

to spin orbit coupling, i.e. a distortion of spherically symmetric charge distribution to elliptical charge distribution. The XMLD signal is maximum with the x-ray polarization vector parallel, compared to perpendicular, to the local magnetic moment direction. The absorption spectra varies as,

$$I = I_0 + I_{\mathrm{XMLD}}, \tag{2.31}$$

given that,

$$I_{\mathrm{XMLD}} \propto \langle M^2 \rangle \cos^2 \phi, \tag{2.32}$$

where ϕ is the angle between the linear polarization vector and the magnetic moment. Due to the M^2 dependence of the XMLD, the effect is equally present in antiferromagnets, as well as ferro- and ferrimagnets [72, 73].

2.8.3 Photoemission Electron Microscopy

Holes created in the core shell during transitions are rapidly filled, resulting in an avalanche of secondary (Auger) electrons emitted from the sample surface via the Auger-Meitner effect. Detecting the secondary electron emission gives the total electron yield, which closely follows the x-ray absorption spectrum. Due to the electron mean free path in the sample, the probing depth (5 nm in transition metals) is limited to the surface [73–76].

The method for producing spatial resolution from the emission of secondary electrons from the sample surface, called photoemission electron microscopy (PEEM), is analogous to the principle of an optical microscope [73, 77, 78]. X-rays illuminate the sample surface and the emitted electrons are focused, using electrostatic or magnetic lenses, onto a detector, typically consisting of a phosphor screen or multichannel plate imaged by a CCD camera. Optimum lateral resolution ($\leq$25 nm) is achieved when the electrons are accelerated to large velocities, which requires voltages of 10 kV to 20 kV between the sample and the microscope [79–81]. It is also required that the energy distribution of the emitted electrons be as narrow as possible to reduce image aberration. However, due to scattering events before secondary electrons are emitted from the sample surface, the focused electron beam can have a wide dispersion of kinetic energy. This is countered in aberration corrected PEEM systems, which employ curved electron mirrors to remove the lowest order aberrations and can achieve lateral resolutions 4 nm [80].

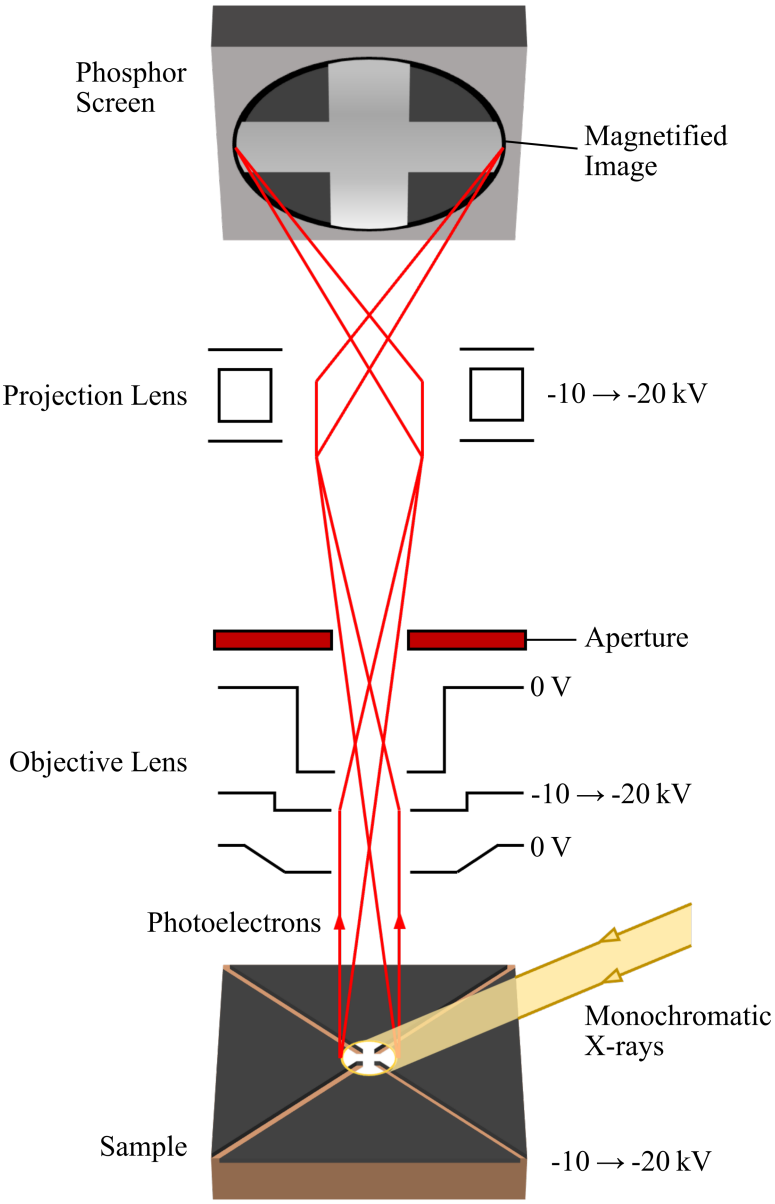

Figure 2.11: *Schematic of a photoemission electron microscope. Monochromatic X-rays, incident on the sample surface, liberate electrons via the photoelectric effect. Photoelectrons emitted from the sample surface are accelerated through a column of lenses and apertures, which focus the electron beam onto a phosphor screen or multichannel plate. The result is a magnified image with high intensity regions where the X-ray absorption coefficient of the sample is largest.*

Chapter 3

Literature Review

Antiferromagnets are a class of magnetically ordered material with zero net magnetization. A swathe of recent experimental studies have shown that electrical control of antiferromagnetic order is possible by two distinct mechanisms: field-like and damping-like torques. This could be revolutionary for the next generation of computing technologies, as the properties of antiferromagnets are advantageous for high speed, high density memory applications. Here, we review the electrical control of antiferromagnets via field-like and damping-like torques, as well as distinguishing from pervasive non-magnetic effects that have raised questions about the origins of the electrically measured switching signals.

Antiferromagnetic (AF) spintronics has gained a lot of interest since the prediction [12] and experimental demonstration [13] of electrical switching by current-induced torques in AF materials. The surge in interest is justifiable as switchable AF devices offer properties that are attractive for high speed, high density memory applications [82, 83]. These include a non-volatile order, terahertz frequency dynamics, no device cross-talk, and a robustness against external magnetic fields. Furthermore, AF order is found in a wide range of materials, from insulators and semiconductors, to conductors and superconductors. They may also be coexistent with symmetries and topologies not found in their ferromagnetic counterparts [84].

Key to fast and efficient switching of AF moments are current-induced Néel-order spin-orbit torques (NSOTs), where the torques induce the same sense rotation of each AF sublattice. It is well established that in conductors lacking spatial inversion symmetry, a charge current can induce a non-equilibrium spin polarization [85], and the resulting

effective magnetic field can manipulate the magnetization in a ferromagnetic crystal [86, 87]. Analogous effects can arise in AF crystals with particular symmetries. CuMnAs [15] and Mn_2Au [88] are collinear antiferromagnets in which the Mn spin sublattices form space-inversion partners, such that a charge current generates an alternating spin polarization that coincides with the sublattices [12]. This is illustrated in Fig. 3.1(a). The resulting local effective fields are directed perpendicular to the current direction [13, 62].

Current-induced torques have also been realized in heterostructures of insulating AF layers and Pt, a heavy metal with a large spin Hall conductivity. Charge current in the Pt layer injects a spin current into the AF layer due to the spin Hall effect [89], as depicted in Fig. 3.1(b). Once injected into the AF, the spin current triggers excitations of the magnetic order by inducing damping-like torques which are an even function of the sublattice magnetic moment [12, 90, 91]. Making use of an external spin current allows for a broader choice of AF material as it does not require specific crystal symmetry. However, the damping-like torque switching is more complex than the Néel order field-like torque due to the dependence of the effective magnetic field on the sublattice magnetic moment orientation [92].

Experimental demonstrations of current-induced switching in AF films typically utilized 8-arm or 4-arm device structures, as illustrated in Fig. 3.2. These geometries allow current pulses to be applied along the biaxial easy magnetic axes of the AF film, with the aim of inducing 90° reorientation of the magnetic moments. For the 8-arm device, current pulses are applied between orthogonal pairs of contacts, whereas for the 4-arm device, to achieve a net current at 45° to the arms in the centre of the device, pulses are sent through all four contacts. Reorientation of the AF moments is detected in the transverse voltage, V_{xy}, with a weak probing current applied at 45° to the current pulse directions. This measures the anisotropic magnetoresistance (AMR) for conducting AFs, or spin Hall magnetoresistance (SHMR) for Pt-capped insulating AFs. Both effects have the same symmetry which is related to the difference in conductivity for probing currents parallel and perpendicular to the magnetic moment orientation.

The first experimental demonstration of reversible current-induced AF switching and electrical readout was performed in biaxial CuMnAs using the geometry illustrated in Fig. 3.2(a) [13]. Later studies showed reversible and reproducible electrical switching

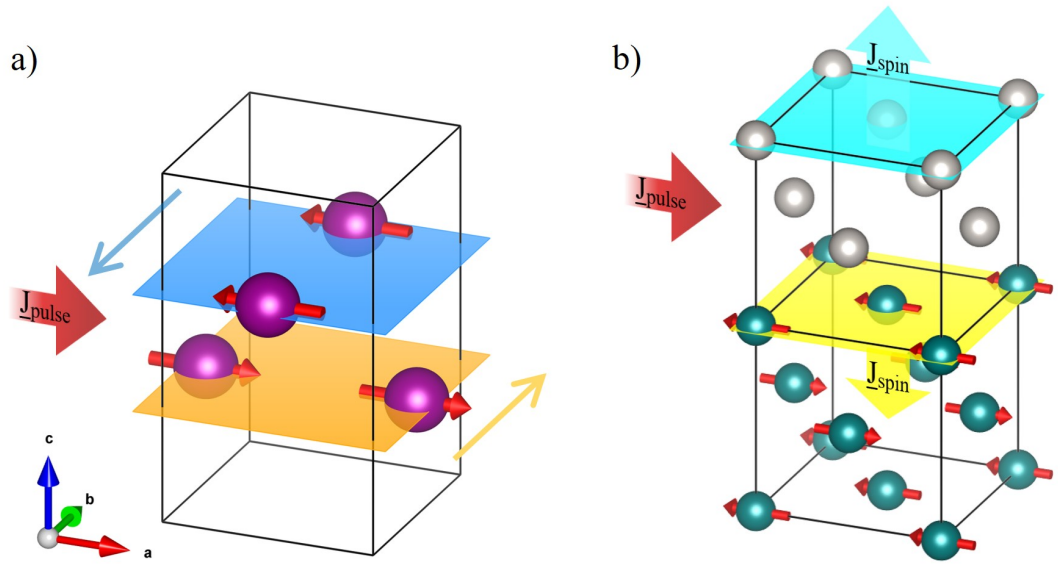

Figure 3.1: *Illustrations of current-induced torques in antiferromagnetic materials. a) Magnetic Mn sites in tetragonal CuMnAs unit cell (shown as purple spheres with red arrows indicating the spin direction) couple antiferromagnetically between sublattices (blue and yellow planes), which are space-inversion partners. An applied current pulse generates a staggered effective field coinciding with the magnetic sublattices (blue and yellow arrows). This creates a field-like torque on the Mn spins, rotating them with the same sense perpendicular to the pulse direction. b) In a bilayer of Pt and NiO, a charge current flowing through the Pt layer (silver spheres) generates a spin current, perpendicular to the charge current direction, due to the spin Hall effect. The spin current is injected into the antiferromagnetic NiO layer which rotates the Ni spins (green spheres with red arrows) via anti-damping torques.*

with current pulse lengths down to ∼100 ps [93] as well as with terahertz electromagnetic pulses [94]. The same approach was used to demonstrate reproducible electrical switching in Mn_2Au [62, 95, 96], and in a wide range of insulating AF/Pt bilayers [92, 97–100]. Table 3.1 summarizes the different physical systems studied with the current amplitudes, pulse lengths, and measurement techniques included.

Multi-level switching has been observed in AF systems, where multiple current pulses or increasing pulse lengths results in an increasing electrical readout signal. This may be attributed to the multi-domain nature of the switching, and the memristive response suggests potential applications in neuromorphic computing [101]. However, qualitatively similar "sawtooth-like" switching signals have also been observed in non-magnetic thin films [102, 103], and in these cases the measured signal has been attributed to electromigration [97, 101, 104], annealing [100] or anisotropic thermal gradients [102]. Electromigration and Joule heating may result in an anisotropic conductivity with the same symmetry as AMR and SHMR. In contrast, thermal gradients may be important on short timescales but are unlikely to produce signals that persist for longer than a few seconds.

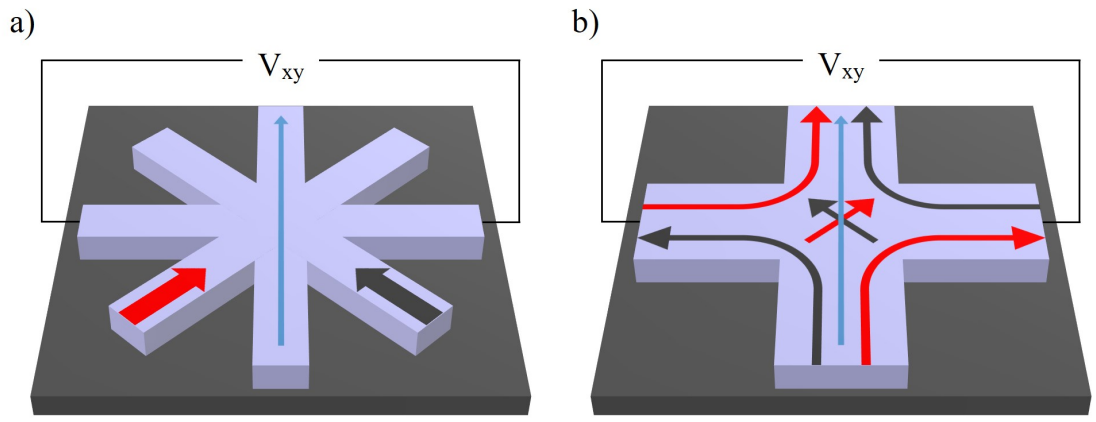

Figure 3.2: *Schematics of pulsing device geometries. Orthogonal current pulses (red and black arrows) rotate the magnetic moments* 90° *between the magnetic easy axes. After each pulse, re-orientation of the magnetic moments is probed by applying a relatively small current (blue arrow) at* 45° *to the pulse directions and measuring the transverse voltage,* V_{xy}*. a) 8-arm geometry, where current pulses are applied between orthogonal pairs of contacts. b) 4-arm geometry, where orthogonal current pulses,* 45° *to the main arms, in the centre of the device are achieved by pulsing between all four contacts.*

It is important to distinguish between AF switching and spurious non-magnetic effects that might contribute to the measured readout signal. Magnetic field-dependent and temperature-dependent studies provide methods to do so, for example, in α-Fe_2O_3 a large applied field fixes the orientation of the AF magnetic moments and suppresses the switching signal [97, 99]. Similarly, the AF metal dichalcogenide, $Fe_{1/3}NbS_2$, shows a switching signal only below its Néel temperature (42 K) and the signal is suppressed by applying a large magnetic field [105]. It has also been shown that electric field induced strain in Mn_2Au can alter the ability to electrically switch between magnetic easy axes due to changing the magnetic anisotropy energy barrier. This is supported by studies of switching in layers grown with different crystallography [95, 106].

A more direct way to assess the effect of current-induced torques in AFs is imaging the sub-micron AF domain structure using X-ray photoemission electron microscopy (XPEEM). Utilizing the polarization dependent absorption of soft x-rays is an established technique for measuring AF domain structures with a spatial resolution of a few tens of nm [72]. Current-induced modification of individual AF domains has been demonstrated using XPEEM in several studies [13, 96, 98, 107–109], but it is essential to establish the reversibility and reproducibility of the microscopic domain switching in order to compare with electrical measurements. This was done in CuMnAs and it was shown for 8 successive pairs of orthogonal pulses, reproducible switching occurs of the

AF domain orientation averaged over a 10 µm area, which clearly correlated with the electrical readout signal [107]. However, at a sub-micron level the switching behaviour was inhomogeneous and stochastic, highlighting the complex behaviour of AF multi-domain switching. In CuMnAs films with larger domains, reproducible current-induced motion of 90° domain walls between two pinning points was observed, with the direction of the domain wall motion determined by the polarity of the current pulse [108]. Several examples of combined XPEEM and electrical switching studies in CuMnAs are shown in Fig. 3.3, which includes reversible domain switching, 90° domain wall manipulation, an example of electromigration, and the time-evolution of the transverse electrical signal after orthogonal current pulses.

XPEEM is an extremely powerful technique for imaging AF domain structure, but it is not easily accessible. This has led to the development of several benchtop tools for imaging the AF order. A promising approach generates thermoelectric voltage with local thermal gradients using a focused laser beam [110, 111]. The spin Seebeck imaging of AF domains in Pt/NiO bilayers revealed both domain rotation and domain wall motion induced by current pulses [111]. Another method uses scanning nitrogen-vacancy center (NV) magnetometry to measure the very weak magnetic stray fields from the layered AF structure and with this method current-induced switching in CuMnAs was imaged [112]. A suppression of the magnetic stray field contrast was observed in the first few seconds following a current pulse, with a recovery on a timescale of hours or days. This behaviour, attributed to a fragmentation of relatively large AF domains into nanoscale textures, was found to be correlated with transient changes in the electrical readout signal [112, 113]. These transient electrical signals can be 'frozen in' at lower temperatures, with a characteristic activation energy of around 0.7 - 0.8 eV [113]. Moreover, the electrical signal can be much larger than the typical $\sim$ 0.2% AMR found in CuMnAs [114], and can also be induced by 100 fs laser pulses [113]. *Ab initio* calculations indicate that in tetragonal CuMnAs the resistivity can depend strongly on the local magnetic order [18]. A connection between the electrical readout, with a large and temperature-dependent relaxation behavior, and the nanoscale AF order can be inferred. However, its micromagnetic origins and relationship to magnetoelastic stresses and defects remain unknown.

A benchtop technique for imaging AF domains which has had recent success involves

the magneto-optical birefringence effect. This method was used to image NiO and CoO thin films [115, 116], as well as a NiO/Pt, 8-arm device in combination with measuring the SHMR signal after orthogonal pulses[117]. A clear distinction was made between electrical signals of magnetic and non-magnetic origin and the magnetic signal was shown to be linearly proportional to the area of domain switching in the center of the device. This result confirms the origin of the electrical signal as corresponding to the AF domain switching, allowing reversible electrical writing and reading to be unambiguously demonstrated in this AF insulator system.

The potential applications for AF spintronic devices are substantial. Their ultra-fast dynamics under field-like and damping-like torques lend themselves to the development of nano-oscillators and detectors in the 'terahertz gap' between electrical and optical sources [118, 119]. The ability to control AF domains electrically extends their usefulness to magnetoelectric memories [120] and magnonic logic devices [121], and it is anticipated that purely AF magnetic random-access memory (MRAM) will exceed the performance of ferromagnetic MRAM [122], which is one of the leading candidates for 'beyond Moore's law' information technologies [94]. The demonstrated multi-level behaviour of electrical switching in AFs allows them to be used as artificial neurons in spiking neural networks (SNNs), something that was previously unattainable using silicon-based hardware, and is of interest due to their ability for writing and speech recognition [101].

While much of the experimental work so far has demonstrated the rotation of the AF domains due to spin-orbit torques, non-magnetic contributions to the electrical signals can occur. This has increased the importance of magnetic field and temperature dependent studies, as well as direct magnetic imaging, in elucidating the role of current-induced spin-orbit torques. However, characterization of the AF order with high spatial and temporal resolution remains a considerable challenge, especially for buried layers and interfaces [123]. Overall, the micromagnetics and timescales of switching need to be investigated further.

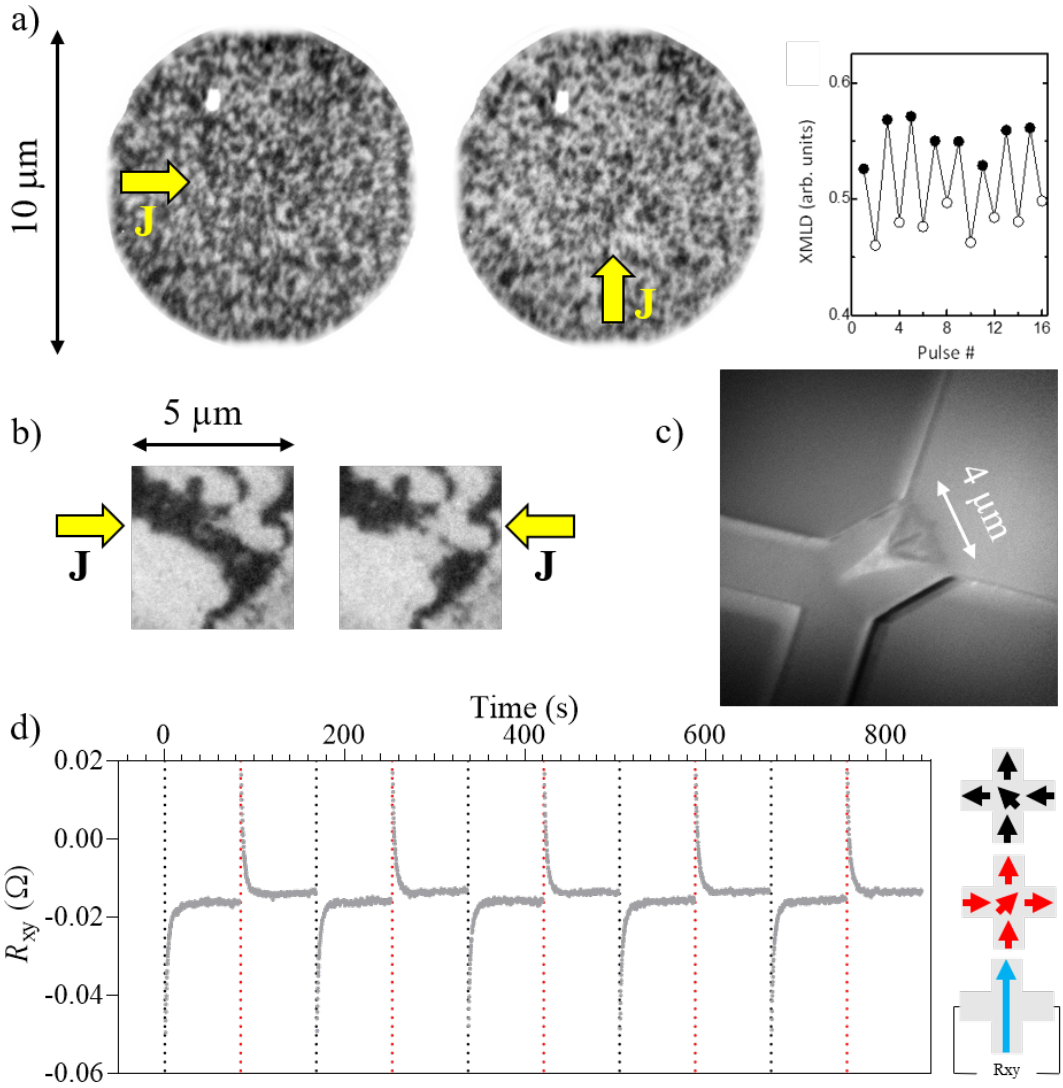

Figure 3.3: *Examples of the effects of electrical pulsing in biaxial CuMnAs. In (a), XPEEM images are taken after applying* $6.1\,\mathrm{MA\,cm^{-2}}$ *current pulses along two orthogonal directions to a film with a granular domain microstructure. The accompanying XMLD signal shows the average domain changes after 16 successive pulses. In b), XPEEM is used to demonstrate switching of a micron-sized domain for* $4.5\,\mathrm{MA\,cm^{-2}}$ *current pulses with opposite polarity. c) demonstrates a nonreproducible electromigration effect in a CuMnAs device after a* $27\,\mathrm{MA\,cm^{-2}}$ *pulse. d) shows the time evolution of the transverse electrical signal in a cross-shaped CuMnAs device. The dashed red and black lines on the plot correspond to the application of* $12\,\mathrm{MA\,cm^{-2}}$ *current pulses, applied in the direction of the red and black arrows shown in the pulsing geometries to the right of the plot. The measurement geometry is also shown, with the blue arrow indicating the direction of the probe current.*

Table 3.1: A summary of experimental electrical switching studies in antiferromagnetic materials, showing material systems, ranges of pulse amplitudes and pulse widths investigated, and detection methods. In the detection method column the abbreviations are as follows: anisotropic magnetoresistance (AMR), spin Hall magnetoresistance (SHMR), X-ray magnetic linear dichroism (XMLD), photoemission electron microscopy (PEEM), and nitrogen-vacancy center magnetometry (NV magnetometry).

Material	$\mathbf{J}_{\text{pulse}}$ (MA cm^{-2})	Pulse width	Detection method	Ref.
CuMnAs/GaAs	4.5	50 - 275 ms	Transverse AMR	[13]
CuMnAs/GaAs	6.1	50 ms	XMLD PEEM	[107]
CuMnAs/GaP	160	100 ps - 10 ms	Transverse AMR	[93]
CuMnAs/GaP	9	50 ms	Transverse AMR, XMLD PEEM	[108]
CuMnAs/GaP	12	10 µs	Resistivity, Optical reflectivity, NV magnetometry, XMLD PEEM	[113]
CuMnAs/GaP	24	10 µs	Transverse AMR, NV magnetometry	[112]
$Mn_2Au(001)/Al_2O_3$	18	1 ms	Transverse AMR	[62]
$Mn_2Au(110)/MgO$	20	100 ns	Transverse AMR	[96]
$Mn_2Au(103,101,204)/MgO$	21	1 ms	Transverse AMR	[95]
$Mn_2Au(001)/Al_2O_3$	13	1 ms	XMLD PEEM	[109]
$Mn_2Au(103)$/PMN-PT	12	500 ms	Transverse AMR, XMLD	[106]
$Pt/Mn_2Au(103)/MgO$	71	1 ms	Transverse AMR, SHMR	[124]
$Pt/NiO(001)/SrTiO_3$	40	1 ms	SHMR	[92]
Pt/NiO(111)/Pt/MgO	54	3 s	SHMR	[97]
Pt/NiO(001)/MgO	150	1 ms	SHMR, XMLD PEEM	[99]
Pt/NiO(001)/MgO	115 - 150	100 µs	SHMR, Magneto-optical birefringence effect	[117]
Pt/α-Fe_2O_3/α-Al_2O_3	150	10 ms	SHMR	[98]
Pt/α-Fe_2O_3/α-Al_2O_3	90	1 ms	SHMR	[100]
$Fe_{1/3}NbS_2$	0.054	10 ms	Transverse AMR	[105]
Ta/MnN/Pt	80 - 100	4 µs	SHMR	[125]
Pt/NiO, Pt	40	10 ms	SHMR	[103]
Nb/MgO	110	1 - 10 ms	Transverse resistivity	[102]

Chapter 4

Electrical Transport Measurements of Current-induced Effects in CuMnAs

4.1 Introduction

CuMnAs has been subjected to intense study due to the experimental demonstration of current-induced NSOT magnetic domain switching [13]. In that study, a 45 nm layer of CuMnAs, epitaxially grown on lattice matched GaP(001), was fabricated into an 8-arm star device with 28 µm arm width. At 273 K and 150 K, current pulses of width 1 ms to 275 ms and current density 4×10^6 A cm^{-2} were applied along orthogonal arms of the device and changes to the equilibrium magnetic domain population were detected in the AMR, probed at 45° to the pulse directions. Measured changes in the transverse resistance (R_{xy}) were congruent with expected AMR symmetry and the signal persisted for long timescales at low temperature, ruling out the possibility of transient thermal effects. It was also shown that consecutive pulses along the same arm caused multilevel behaviour of the R_{xy} signal, which was attributed to saturation of sub-micron domain switching, inaccessible with a single pulse. This was confirmed in a later study using XPEEM to image the AF domain structure [107]. A 4-arm cross device with 10 µm arm width was fabricated from an 80 nm thick layer of CuMnAs, epitaxially grown on

GaAs(001), which, due to larger lattice mismatch than GaP(001), is known to induce a relaxed tetragonal phase of CuMnAs [14, 15]. The XPEEM images revealed sub-micron AF domains with biaxial anisotropy. After application of $6 \times 10^6\,\mathrm{A\,cm^{-2}}$, 1 ms pulses along orthogonal arms of the device at room temperature, reconfiguration of the domain structure was imaged and correlated with simultaneous electrical AMR measurements. After application of pairs of orthogonal pulses, magnetic domains in the central region of the device were shown to reversibly switch perpendicular to the pulse direction, with some domains pinned by local strains and defects. The grainy nature of the magnetic texture and inhomogeneous switching behaviour provided evidence that the multilevel signal, measured in [13], was cumulative switching of previously pinned domains by thermal activation as the pulse train progressively heated the device.

Electrical readout signal of the multilevel regime in CuMnAs was thoroughly investigated as a function of pulse width, duty cycle and integrated pulse time [93]. The results highlighted device durability. A 4-arm cross device with 2 µm arm width, fabricated from a 60 nm layer of CuMnAs on GaP(001), was subjected to 100's of current pulses in each pulse train with individual pulse widths spanning 10 ms down to 100 ps. Using a fixed pulse current density of $3 \times 10^7\,\mathrm{A\,cm^{-2}}$, a universal trend of the readout signal as a function of the integrated pulse time was revealed for pulse widths >50 µs. At shorter pulse widths, it was determined that the current-induced heating of the device did not saturate, alluding to the fact that the multidomain switching was thermally assisted. A later study by the same group extended the pulsing regime to terahertz frequencies using linearly polarised optical laser pulses [94]. The incident electric field was influenced by the Au contact pads to generate a current in the centre of the device with a direction parallel to the electric field polarisation. Therefore, by rotating the linear polarisation between two orthogonal directions, the current induced in the device was rotated, equivalent to the electrical contact experiments. Comparing the multilevel signal for the two pulse methods, it was shown that increasing the pulse frequency to terahertz using a noncontact setup produced a quantitatively identical response to that of the traditional electrical contact pulsing method and confirmed the potential benefit of using AFs instead of FMs for high speed MRAM devices.

As well as CuMnAs layers grown using MBE, orthogonal electrical pulse switching was performed on layers grown by magnetron sputtering [102]. In that study, the temper-

ature dependence of the multilevel switching signal in an 8-arm star device with 8 µm pulse arm width, fabricated from a 68 nm layer of CuMnAs on GaAs(001), was investigated, including the relaxation of the switched state back to equilibrium after pulsing was stopped. It was noticed that the shape of the switching and relaxation phases was altered depending on the sample base temperature. A macroscopic thermal activation model described the experimental observations in terms of a distribution of magnetic grain volumes overcoming an anisotropy energy barrier with attempt rate given by the Néel-Arrhenius equation [96, 102]. The experimental data was fitted with a sum of exponential decays indicating an ensemble of independently relaxing systems. Joule heating during application of the current pulse contributed to the switching of a larger distribution of grain volumes with varying decay rates. Overall, the model reinforced the idea of multidomain switching, indicated in earlier studies [13, 93, 94, 107], enabled by increased pulse amplitude and width (larger Joule heating effect), as well as by pulse trains applied along a single direction.

The story changed when a high resistive state was induced, using optical and unipolar voltage pulses, in microbar devices and Wheatstone bridges fabricated from a 50 nm layer of CuMnAs, epitaxially grown on GaP(001) [126]. This "quench switched" state was probed in the longitudinal resistivity (R_{xx}), as well as the optical reflectivity of the devices, and reached sizes $> 20\%$ at room temperature, indicating an origin independent from orthogonal switching induced AMR changes. The decay of the resistive signal, immediately after pulsing, followed the stretched exponential (or Kohlrausch exponential) that was used in the thermal activation model. Decreasing the device temperature below 200 K "locked in" in the quenched state, whereby the characteristic decay time, extracted from the model, approached years. Furthermore, application of subsequent lower amplitude pulses sped up the decay process, giving rise to a falling edge in the signal, which reaffirmed an origin independent from transient thermal effects. Instead, three magnetic imaging techniques, scanning NV magnetometry, magneto-Seebeck microscopy, and XPEEM, alluded to a nano-fragmentation of the magnetic domains (10 nm in size) after application of high current density pulses [112, 126, 127]. In this state, the increased domain wall density contributed to the increase in device resistivity, and the decay of the electrical signal was ascribed to relaxation of the nano-fragmented domains back towards the pristine state.

Recently, the quench switched state was investigated in high magnetic field [128]. By applying field sweeps up to 14 T, it was shown that hysteretic phenomena in the magnetoresistance exists in the switched state, but not the relaxed state. These experiments were done using 10 µm Hall bar devices, fabricated from 50 nm layers of CuMnAs, epitaxially grown on GaP(001). The results were attributed to the interplay between ∼100 nm scale 90° and 180° domain walls and atomically sharp 180° domain walls, which act like pinning sites. As imaged using XPEEM in a previous field dependent study, large fields (7 T) were able to reorient the AF domains in CuMnAs, but the domain walls were left mostly unaffected [129]. This was shown to be the case also, measured electrically in the switched state magnetoresistance, after application of 60 T field pulses [128]. Whilst significant effort has been made in correlating electrically measured resistive signals with imaged current-induced AF domain alteration in CuMnAs, less focus has been given to exploring switching effects under conditions within the remit of everyday functionality. In this chapter we investigate switching signals in the range of temperatures, 270 K to 320 K, in three layers of CuMnAs: a 46 nm layer grown on GaP, which is known to exhibit large biaxial domains, a 20 nm layer on GaP which is uniaxial, and a 60 nm layer on GaAs, with 10 % As→Sb substitution, which has much smaller domain size and is relatively easy plane.

4.2 Method

The methodology used in the switching experiments presented in this chapter resembles that of earlier studies [13, 93, 94, 102, 130]. Figure 4.1a shows an optical micrograph of the device design used. In this image an 8-arm device with 10 µm arm width was fabricated via chemical etching from a 60 nm layer of $CuMnAs_{1-x}Sb_x$ ($x = 0.1$), epitaxially grown on GaAs(001). Light regions indicate areas of CuMnAs, and dark regions where the layer was etched away to reveal the substrate. The same fabrication procedure and device design were used for all layers investigated (see fabrication section).

The devices were mounted onto in-house made headers, consisting of a PEEK disk, 12 brass pins around the circumference and a cylindrical copper slug at the centre. The devices were adhered to the copper slug using GE varnish, ensuring excellent thermal contact. Al wire bonds were bonded from the device contact pads to the brass pins using a wedge bonder. Once a device was mounted and bonded the header was inserted

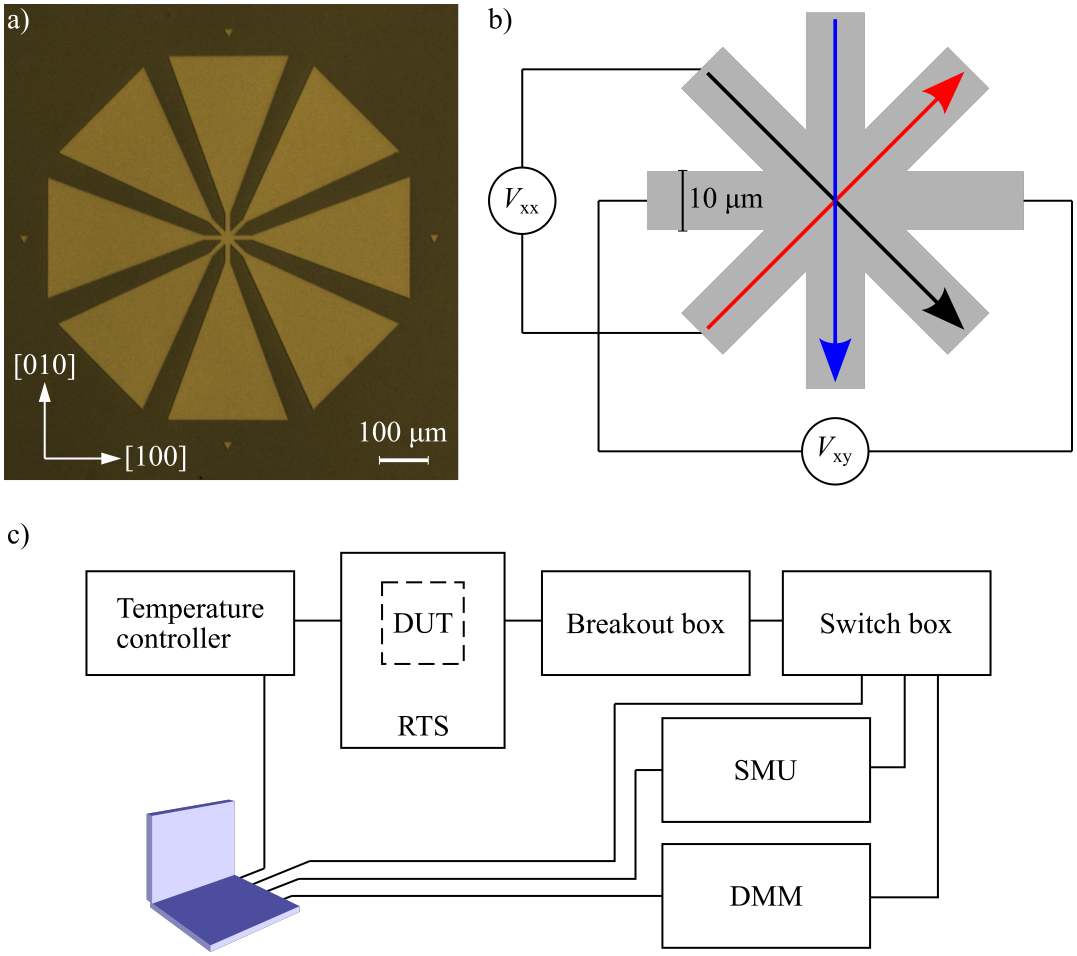

Figure 4.1: *Overview of the device design and experimental setup used in electrical switching experiments. The optical micrograph, a), shows the 8-arm device fabricated from a* 60 nm *layer of CuMnAs doped with 10% Sb, epitaxially grown on GaAs. The device had* 10 µm *arm width with the diagonal arms aligned along the [1-10] and [110] CuMnAs crystal axes. The schematic in b) shows the pulse and probe geometry, where black and red arrows indicate the pulse directions and the blue arrow represents the probe applied after each pulse. For* ∼250 s *during probing, the longitudinal voltage, V_{xx}, and transverse voltage, V_{xy}, were measured simultaneously. The experimental setup is illustrated in c).*

into an in-house built room temperature system (RTS), so called because of its precise temperature stability between 270 K to 320 K. The system was evacuated to pressures $<1 \times 10^{-6}$ mbar before measurements were made. This was important for preventing thermally induced oxidation of the device when applying high current density pulses.

At each temperature, 270 K to 320 K in steps of 10 K, the devices were pulsed with three pairs of orthogonal pulses along the diagonal arms, corresponding to the [1-10] and [110] CuMnAs crystal axes. The schematic in Figure 4.1b shows the electrical pulse and probe configuration used. 1 ms wide current pulses, illustrated by the black and red arrows, were supplied by a Keithley 2461 Source Meter Unit (SMU). After each pulse, the SMU was used to provide a continuous probe current along the vertical [0-10] arm of the

device, illustrated by the blue arrow, and the longitudinal voltage, V_{xx}, and transverse voltage, V_{xy}, were simultaneously measured at a rate of 10nplc for ∼250 s. The 4-wire V_{xx} and V_{xy} measurements were made by the Keithley 2461 SMU and a Keithley 2000 digital multimeter (DMM), respectively.

Figure 4.1c presents a schematic overview of the experimental setup. The device under testing (DUT) is shown housed within the RTS. To the left of the RTS is the temperature controller, which connected to a computer for remote operation. To the right, the DUT was electrically connected to a 12 pin breakout box. A relay switch box enables remote configuration of the source and measure pin assignments. The SMU was connected to $I+$ and I- input channels of the switch box as well as the $V_{xx}+$ and V_{xx}- measurement channels, and the DMM was connected to the $V_{xy}+$ and V_{xy}- measurement channels. The switch box, SMU and DMM were remotely operated by a computer.

4.3 Results

4.3.1 Resistive switching signal relaxation

Above a sample dependent threshold current pulse amplitude, the R_{xy} and R_{xx}, measured after each pulse, displayed a multi-component relaxation behaviour. Within the 250 s measurement window after each pulse, two components of the relaxation were clearly visible. Figure 4.2 shows, for the three measured samples, the R_{xy}, shifted by the mean value, $\bar{R}_{xy} = \frac{|R^1_{xy}|+|R^2_{xy}|}{2}$, after each pulse, 1 and 2, during 3-pairs of orthogonal pulses at temperatures 270 K to 320 K. The pulse and probe geometry used was as shown in Figure 4.1b, with pulse 1 along the direction of the black arrow and pulse 2 along the red arrow. The R_{xy} has been plotted with colours corresponding to the direction of the preceding applied pulse. Each plot corresponds to one of the samples, stacked vertically in order of CuMnAs layer thickness (20 nm top, 46 nm middle, and 60 nm bottom). Data sets for different temperatures are demarcated by vertical dashed lines. The probe current used was 0.1 mA for the 20 nm sample and 1 mA for the 46 nm and 60 nm samples. Current densities of the applied pulses were within the range $1.2 \times 10^7\,\mathrm{A\,cm^{-2}}$ to $1.4 \times 10^7\,\mathrm{A\,cm^{-2}}$ for the 20 nm sample, $1.0 \times 10^7\,\mathrm{A\,cm^{-2}}$ to $1.2 \times 10^7\,\mathrm{A\,cm^{-2}}$ for the 46 nm sample, and $0.4 \times 10^7\,\mathrm{A\,cm^{-2}}$ to $0.5 \times 10^7\,\mathrm{A\,cm^{-2}}$ for the 60 nm sample. These ranges of current density were typical of switching amplitudes in thin-film CuMnAs and

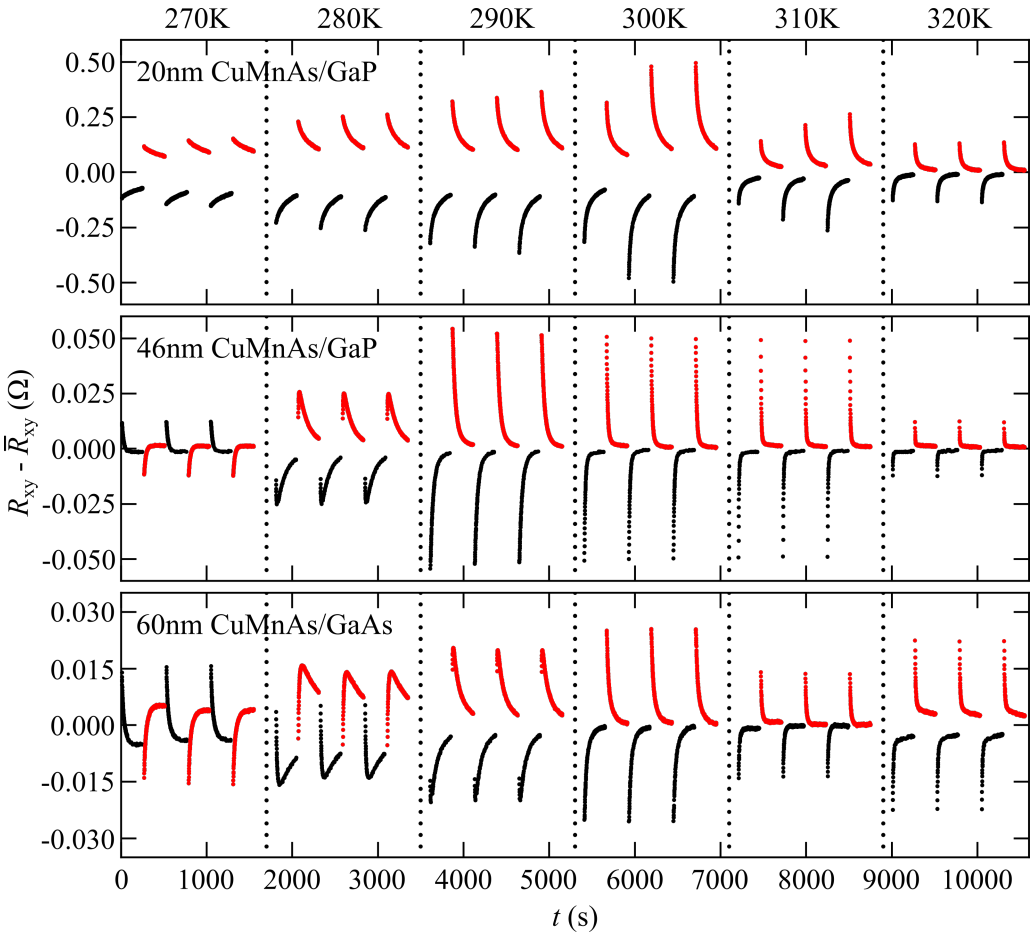

Figure 4.2: *Temperature dependence of the current pulse induced R_{xy} relaxation in CuMnAs samples of thickness* 20 nm *(top),* 46 nm *(middle),* 60 nm *(bottom). The pulse and probe geometry used is shown in Figure 4.1. 3-pairs of* 1 ms *pulses were alternately applied along orthogonal arms of the device and the R_{xy} was measured for* 250 s *after each pulse. The R_{xy} values are centred around 0 by subtracting the mean value for each set of pulses, $\bar{R}_{xy}$. Pulsing sets were conducted at temperatures,* 270 K *to* 320 K*, demarcated by vertical dashed lines.*

were well below the onset of damaging effects, such as electromigration [13, 93, 94, 96]. Effects of device damage, signalling too large a current density, were usually identified as sharp, persistent changes in the R_{xy}.

Shown in Figure 4.2, the R_{xy} relaxed from an initial resistive state towards an equilibrium base value (0 on the shifted scale). Note that these plots show the measured signal after the maximum current pulse amplitude at each temperature. The R_{xy} relaxation changed sign after orthogonal pulses, as a result of asymmetric regions of high current density. This is distinct from the AMR detected 90° reorientation of domains. As temperature was increased, the time for the R_{xy} to relax to equilibrium decreased. This appeared clearest in the 20 nm sample (top plot), whose relaxation components were the same sign, towards equilibrium. Conversely, the 46 nm and 60 nm samples (middle and bottom plots) exhibited a secondary component, apparent at temperature $\leq$290 K,

with shorter relaxation time and opposite sign to the primary component. Most clearly visible at 280 K, the transient secondary signal diverged the R_{xy} away from equilibrium during the first 20 s after the pulse, after which, the slower primary relaxation component (towards equilibrium) began to dominate. For 270 K sample temperature, the secondary component relaxation time elongated to ∼125 s before the primary relaxation, which appeared stationary at this time scale. This gave the impression of the R_{xy} relaxation reversing sign as temperature was decreased from 290 K to 270 K. The presence of multiple relaxation components and a lengthening of the relaxation time at lower temperature is compounding evidence that the measured signal is not dissipation of remnant heat induced by the current pulse. It is shown in section 5.3.3 and other studies [126] that the sample temperature returns to equilibrium within microseconds after the pulse.

Measured simultaneously, the R_{xx} signal is shown in Figure 4.3. As a result of the pulse and probe geometry, the R_{xx} relaxation did not change sign after orthogonal pulses. To accommodate for the temperature dependent equilibrium R_{xx} value, the mean value of 10 data points, R_0, measured before each set of pulses, was subtracted from the raw R_{xx} values. Figure 4.3a shows R_0 at each temperature for the three samples, which increases from 270 K to 320 K, as expected of the metallic layer, CuMnAs. Figure 4.3b shows the R_{xx}, with R_0 subtracted, measured during the pulsing sequence. The shape of the temperature-dependent relaxation was qualitatively equivalent to the R_{xy}, except for in the 20 nm sample at 270 K, where the signal size was within the measurement noise. Noticeable in the 20 nm and 46 nm samples at ≥300 K, the base R_{xx} value increased (and plateaued for the 46 nm sample) during the set of pulses. This was likely due to a drift in the system temperature during the measurement.

To explore the R_{xy} relaxation quantitatively, the difference signal, $\Delta R_{xy} = \frac{R^1_{xy} - R^2_{xy}}{2}$, averaged over the set of 3-pairs of orthogonal pulses was considered. This is plotted in Figure 4.4 for the three samples (columns) pulsed with increasing current pulse amplitude (colours) and at each temperature (rows). As pulse amplitude was increased in the three samples (green to black), the signal size increased for all temperatures.

The onset of the distinguishable relaxation components occurred at different pulse amplitudes. The (opposite-sign) secondary component relaxation, present in the 46 nm and 60 nm samples, occurred at a lower current pulse amplitude than the primary compo-

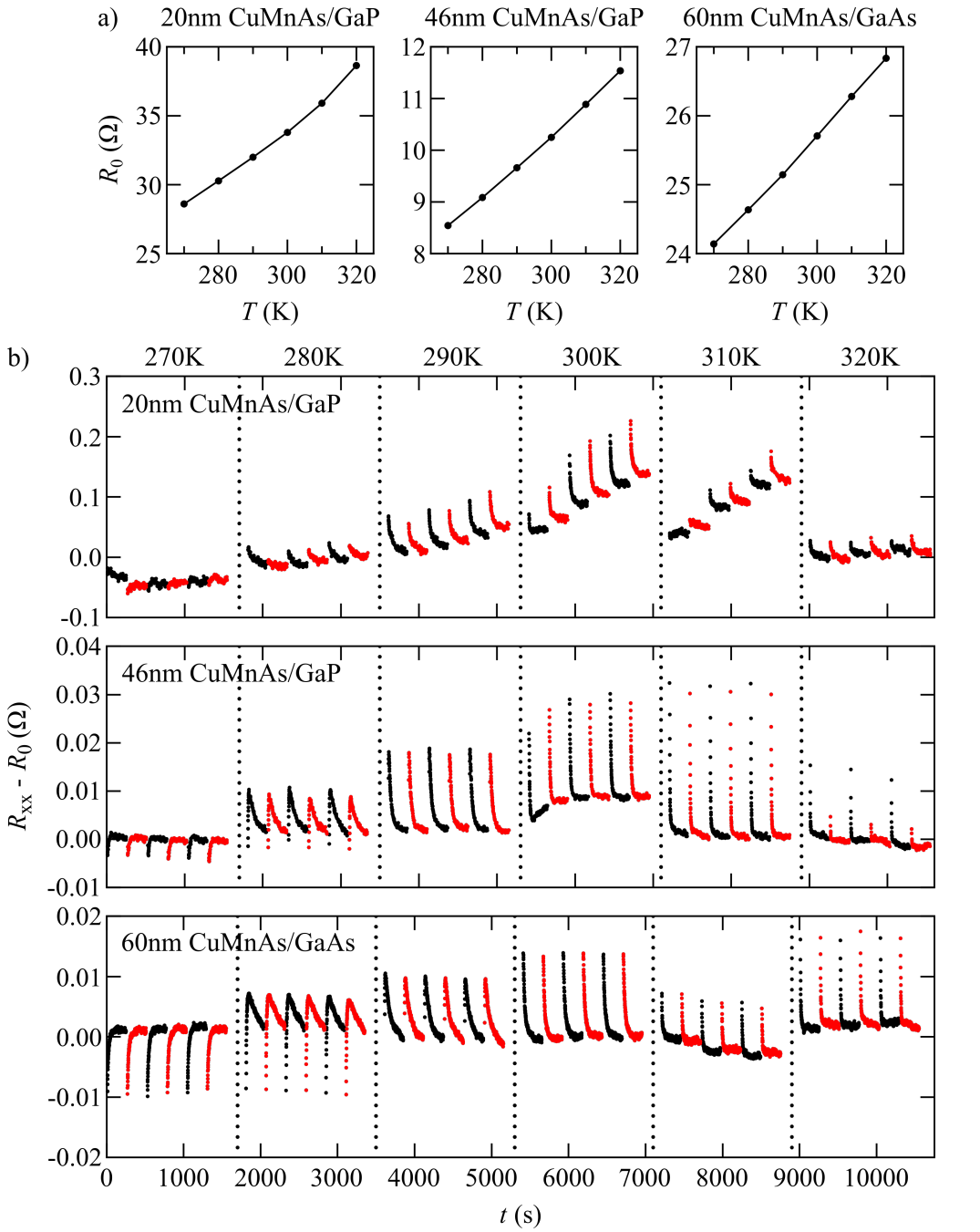

Figure 4.3: *a) R_{xx} base value, R_0, of the three samples measured at* 270 K *to* 320 K. *b) Current pulse induced R_{xx} relaxation measured simultaneously to the R_{xy} shown in Figure 4.2. The R_{xx} value is shifted towards 0 by subtracting R_0 at each temperature.*

nent. This is most clearly seen in the 280 K plots, where the secondary, shorter relaxation time component had a larger contribution at lower current pulse amplitudes and as the pulse amplitude was increased the primary, longer relaxation time component became more prominent.

This behaviour was reversed in the 20 nm sample. Instead, the R_{xy} relaxation shown at temperatures 270 K to 290 K were well described by a single exponential relaxation

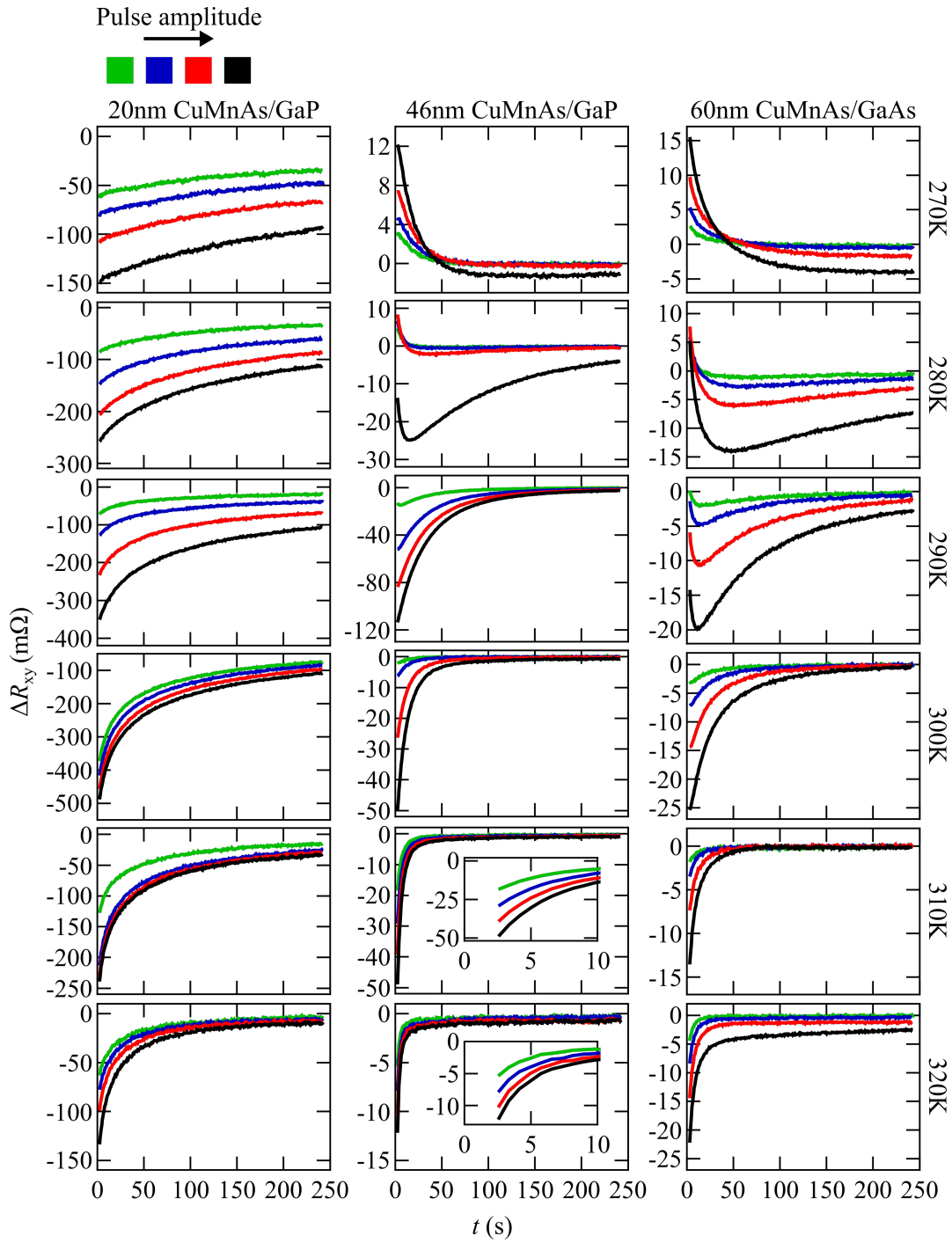

Figure 4.4: *The difference between R_{xy} relaxations measured after orthogonal* 1 ms *pulses, $\Delta R_{xy} = \frac{R^1_{xy} - R^2_{xy}}{2}$, averaged over 3-pairs of pulses. Shown are the three samples (columns) of varying CuMnAs layer thickness, pulsed with increasing current amplitudes (green to black) at temperatures between* 270 K *to* 320 K *(rows). Note that the absolute values of the pulse amplitudes, represented by the different colours, varies for different samples and temperature. Inset plots show the ΔR_{xy} signal during the first* 10 s *after the pulse.*

term (as discussed further below), analogous to the primary component identified in the 46 nm and 60 nm samples. At temperatures >290 K, a secondary, same sign relaxation appeared with a much longer decay time, phenomenologically distinguishable from the secondary relaxation components observed in the 46 nm and 60 nm samples.

4.3.2 Kohlrausch stretched exponential fitting

The Kohlrausch stretched exponential relaxation is ubiquitous in complex magnetic interacting systems, such as spin glasses and superparamagnetism in collections of magnetic nanoparticles [131–134]. The functional form of the two-component relaxation is given by,

$$a_1 \exp\Big\{-(t/\tau_1)^{\beta}\Big\} + a_2 \exp\Big\{-(t/\tau_2)^{\beta}\Big\} + c, \tag{4.1}$$

where $a_{1,2}$ are amplitudes of the primary relaxation component, 1, and secondary relaxation component, 2; $\tau_{1,2}$ are the relaxation times; $\beta = d/(d+2)$ where d reflects the dimensionality of the system; and c is a constant offset corresponding to the remnant signal after ∼250 s. Note that, the definition of primary and secondary relaxation for the 46 nm and 60 nm samples refer to the component of the signal that decays over the period of the measurement window at room temperature (∼250 s at 290 K) and the more transient signal decay that decays, with opposite sign, within the first 20 s at room temperature, respectively. This is more arbitrarily defined for the 20 nm sample, which exhibits relaxation components with the same sign decay. In this case, the more transient relaxation is simply defined as the secondary component.

It is expected that the relaxation is made up of a larger ensemble of stretched exponential components which have relaxation times far exceeding the measurement window. In this case, the constant offset, c, is justified as $a \exp\{-(t/\tau)^{\beta}\} \rightarrow a$ for $\tau >> t$. Within the framework of relaxing complex systems, the exponent, $\beta = 0.6$, is fixed by the dimensionalities of the diffusion equation [134], where $d = 3$ from our experimental observations.

Figure 4.5 shows, for the three samples, the R_{xy} relaxation after varying current pulse amplitudes at 290 K, fitted with a Kohlrausch stretched exponential function of the form given in Equation 4.1. Fitting was done using non-linear regression software, cftool, designed and implemented by Dr Richard Campion. The trust-region method was used, enabling parameter constraints to be made. These included specifying $\tau_{1,2} > 0$ and $\mathrm{sgn}(a_{1,2}) = -1$ for the 20 nm sample and +1 for the 46 nm and 60 nm samples. The data is plotted with $\log_{10}$ time scale to highlight the compatibility of the fit with both components of the relaxation (the transient secondary component relaxes within the first 20 s for the 46 nm and 60 nm layer).

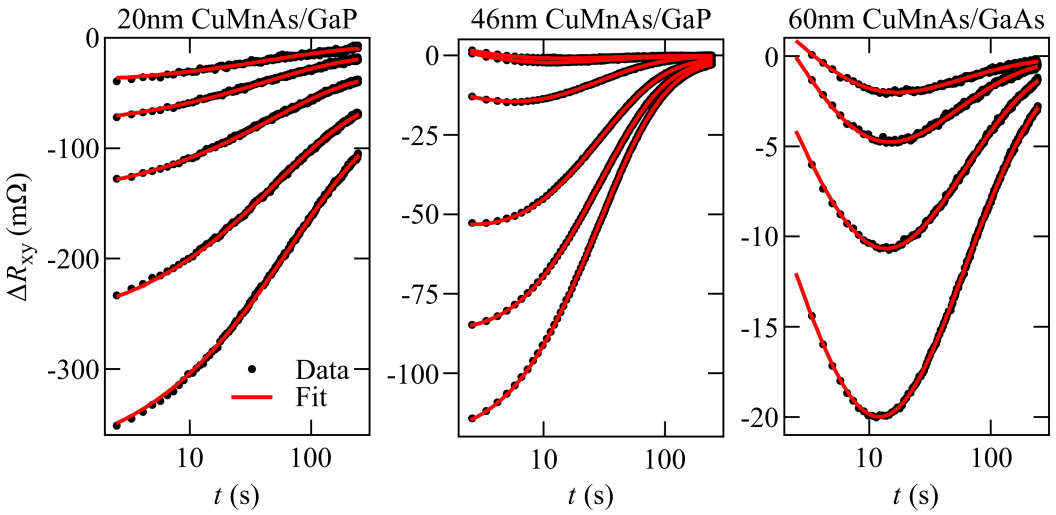

Figure 4.5: *Kohlrausch stretched exponential fitting of the ΔR_{xy} relaxation measured, after current pulses of varying amplitude, in the three CuMnAs samples at* 290 K.

Relaxation dynamics

Congruent with theory, the relaxation times $\tau_{1,2}$ followed a temperature dependence given by the Néel-Arrhenius equation, in the form of a simple exponential,

$$\tau_{1,2} = \tau_0 \exp\{E_{1,2}/k_{\mathrm{B}}T\}, \tag{4.2}$$

where τ_0 is a material dependent attempt time, $E_{1,2}$ is an energy barrier between two spin states associated with each relaxation component, k_{B} is the Boltzmann constant, and T is the sample temperature. Figure 4.6a shows $\tau_{1,2}$ measured at each temperature for the three samples following the Néel-Arrhenius trend. The labelling of parameters $\tau_{1,2}$ and $E_{1,2}$ is consistent with the definition of the primary, 1, and secondary, 2, relaxations outlined in the description of the Kohlrausch stretched exponential fitting. The data was linearized by plotting on a logarithmic scale axis against $1000/T$ and fitted with a robust regression linear fit. The extrapolated fit line intercepts the vertical axis at the point, τ_0. As shown in the left-hand plot of Figure 4.6b, τ_0 was estimated, for the three samples, to be picoseconds (3×10^{-13} s to 6.5×10^{-12} s), typical of antiferromagnetic dynamics [126, 135]. Previous studies of ferromagnetic nanoparticle systems measured τ_0 three orders of magnitude larger, in the nanosecond range [136, 137].

The right-hand plot in Figure 4.6b shows the energy barrier, $E_{1,2}$, measured from the gradients of the $\tau_{1,2}$ fit lines in Figure 4.6a for the three samples. There were observed distinct energy barriers associated with the two relaxation components. $E_{1,2}$ follow

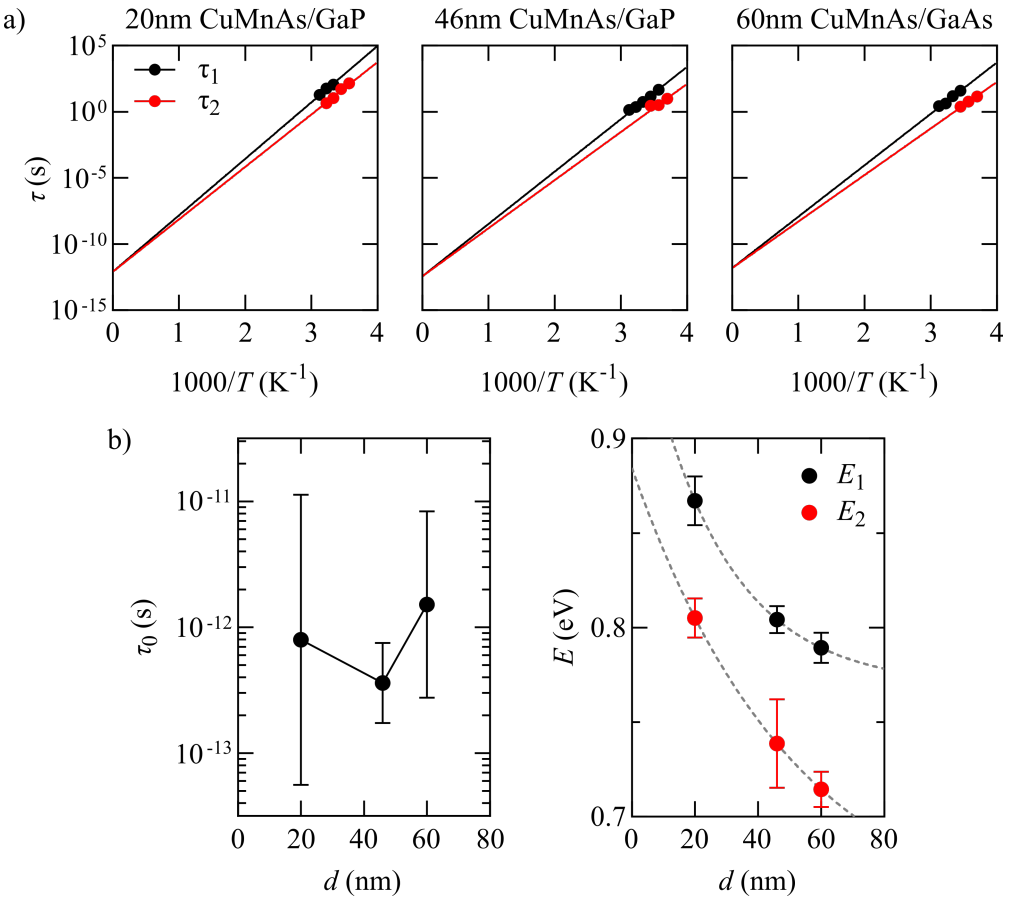

Figure 4.6: *a) $\tau_{1,2}$, measured for the three CuMnAs samples, plotted on a logarithmic scale as a function of $1000/T$. Néel-Arrhenius exponential fits appear as straight lines. Both $\tau_{1,2}$ fit lines are constrained so that the vertical intercept, corresponding to a material dependent attempt time, τ_0, is the weighted average of the unconstrained fits. Shown in b), the weighted average τ_0 (left), and energy barrier, $E_{1,2}$ (right), calculated from the gradient of the fits in a). Dashed curves, plotted to guide the eye, are exponential fits of $E_{1,2}$ as a function of sample thickness.*

from the phenomenological description of the two relaxation components measured in the three samples. The relative size of E_1 compared with E_2 describes the decay times of the corresponding relaxation components. $E_1 > E_2$, as seen in the 46 nm and 20 nm samples, suggests a smaller distribution of spins overcoming the E_1 energy barrier due to thermal fluctuations and, consequently, a longer decay time of the primary, compared with secondary, relaxation. Conversely, $E_1 < E_2$, measured in the 20 nm sample dictates a longer secondary relaxation component.

Signal amplitude and threshold current density

The relaxation components amplitudes, $a_{1,2}$, and remnant signal, c, were extracted from the Kohlrausch stretched exponential fits. The plots in Figure 4.7 show $a_{1,2}$ and c as a function of current pulse amplitude. Each sample corresponds to a column of plots, with a_1 shown in the top row, a_2 in the middle row and c in the bottom row. The

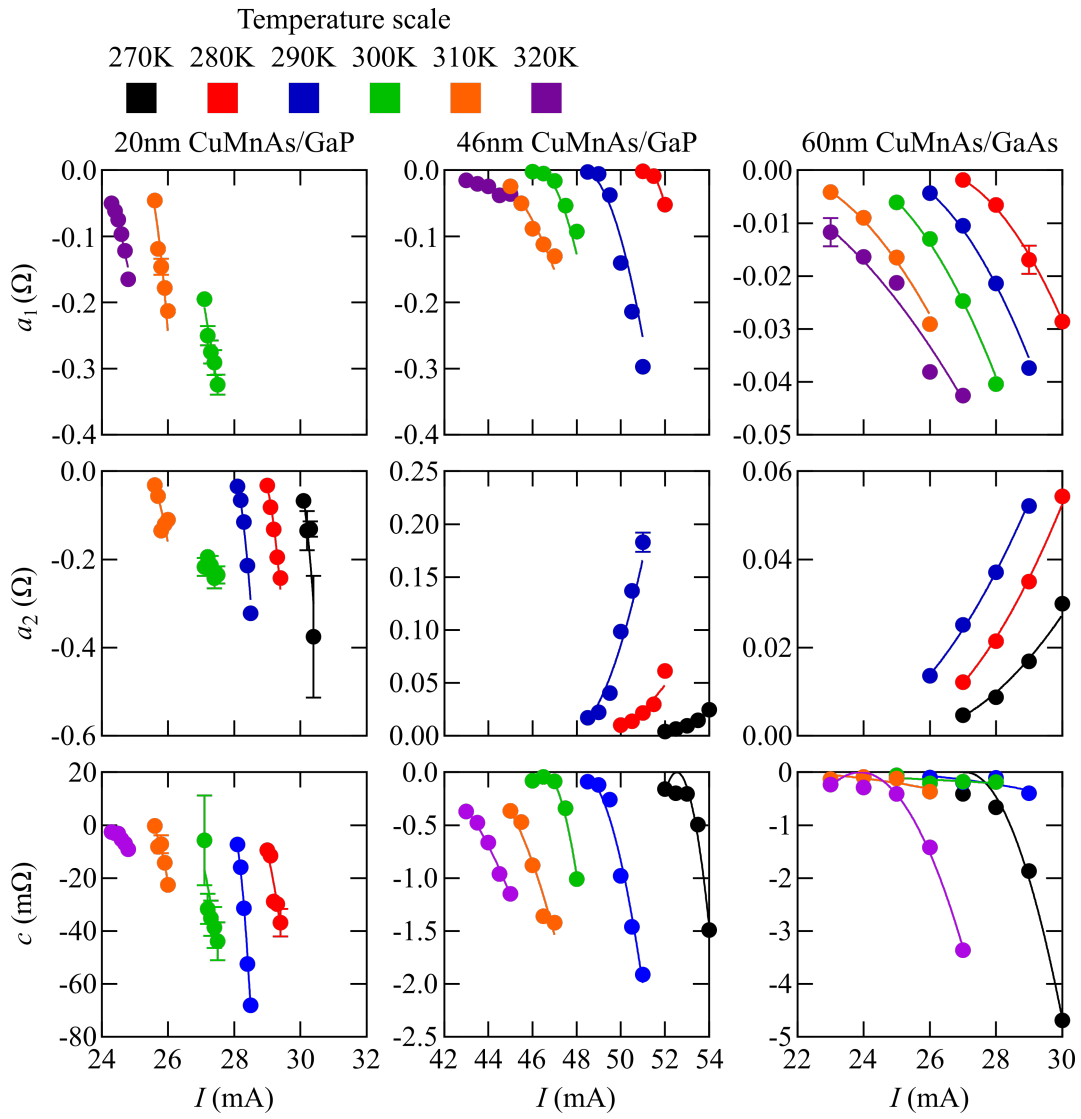

Figure 4.7: *Amplitudes, $a_{1,2}$, of the two relaxation components and remnant signal, c, measured in the three CuMnAs samples as a function of current pulse amplitude. The colour of each data set corresponds to the sample temperature at which the pulsing was conducted, indicated by the key above the plots. The amplitudes and remnant signal followed a parabolic dependencies on the current pulsed amplitude, as shown by the solid fit lines.*

colour scale indicates the sample temperature. The relaxation amplitudes and remnant signal at each temperature varied parabolically as a function of the applied current pulse amplitude. Equivalent functions of the form,

$$a_{1,2} = A_{1,2}(f \cdot I - J_{1,2})^2, \tag{4.3}$$

and,

$$c = A_c(f \cdot I - J_c)^2, \tag{4.4}$$

were fitted to the relaxation amplitudes and remnant signal, respectively. $A_{1,2}$ and A_c are the parabola steepnesses, which describe the response of the relaxation amplitudes and remnant signal to the current pulse amplitude, I. The coefficient, $f = 1/(100 \times d)$, dependent on the sample thickness, d, scales the units of I from mA to Acm^{-2}. Thus, $J_{1,2}$ and J_c are the threshold current densities associated with the onset of the two relaxation components and remnant signal. Fitted curves are plotted in Figure 4.7 as solid lines.

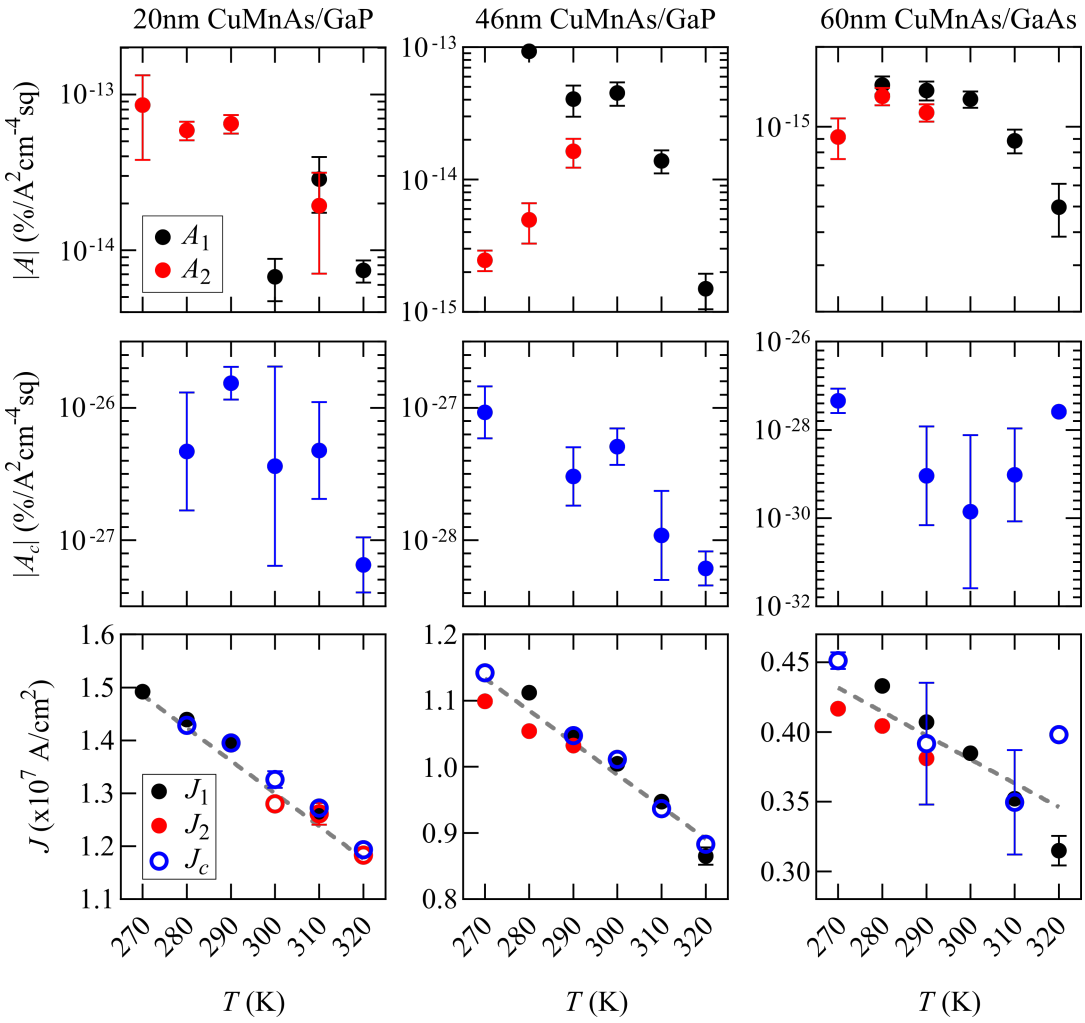

Figure 4.8: *From the parabolic fits of $a_{1,2}$ and c, shown in Figure 4.7, the absolute value of the parabola steepness, $A_{1,2}$ (top), A_c (middle), and pulse threshold current densities, $J_{1,2}$ and J_c (bottom), were measured as a function of sample temperature, between* 270 K *to* 320 K. *Dashed best fit lines in the bottom plots are through the combined data of $J_{1,2}$ and J_c.*

The top and middle rows of Figure 4.8 show the absolute value of the parabola steepnesses, $|A_{1,2}|$ and $|A_c|$, scaled with the sample sheet resistance, R_{sq}, measured at each temperature using the standard Van der Pauw method [138]. Measured values of $|A_2|$ in the 20 nm and $|A_1|$ in 46 nm and 60 nm samples exhibit congruent temperature dependencies. The size of $|A_{1,2}|$ in the 20 nm and 46 nm samples were the same order of

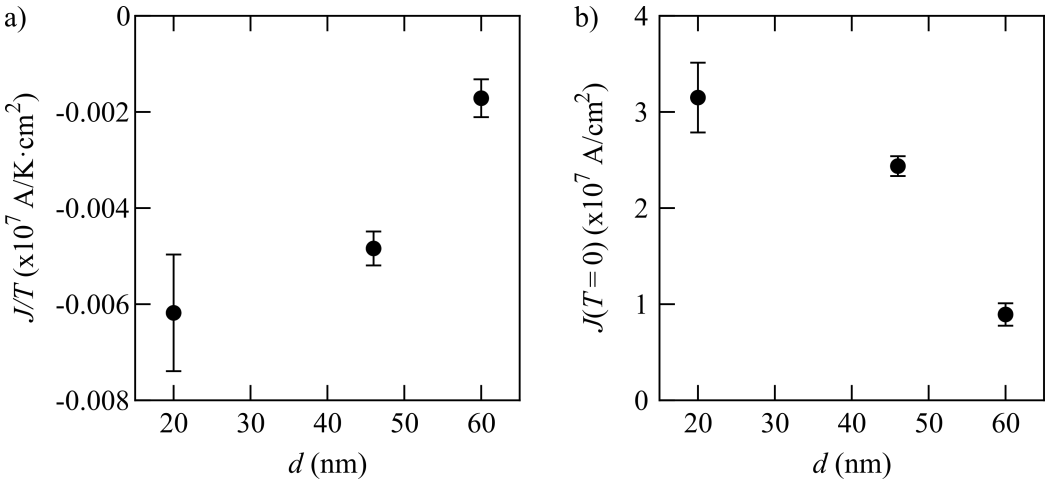

Figure 4.9: *Linear fit parameters of the threshold current densities as a function of sample thickness. a) shows the gradient of the fit line, and b) shows the interpolated value of J at $T = 0$.*

magnitude, whereas the 60 nm sample showed values of $|A_{1,2}|$ two orders of magnitude smaller at 280 K. The 46 nm and 60 nm samples, had similar temperature dependent trends in $|A_{1,2}|$; $|A_1|$ decreased in the temperature range 280 K to 320 K; and $|A_2|$ increased in the range 270 K to 290 K. This behaviour was swapped between $|A_{1,2}|$ in the 20 nm sample, and $|A_1|$ was present at a higher temperature range, 300 K to 320 K.

The absolute parabola steepness, $|A_c|$, of the remnant signal fits, shown in the middle row of Figure 4.8, displayed congruent decreasing value as a function of temperature for all three samples. An exception occurred for the 60 nm at 320 K, where $|A_c|$ increased away from the trend. The size of $|A_c|$ for the three sample was comparable within an order of magnitude, but was $>$ 13 orders of magnitude smaller that the values of $|A_{1,2}|$. The threshold current densities, $J_{1,2}$ and J_c, were the points at which measurable relaxation components, 1 and 2, and a remnant signal after $\sim$250 s were measured, respectively. The bottom row of plots in Figure 4.8 show $J_{1,2}$ and J_c overlayed. Commensurate values of $J_{1,2}$ and J_c showed a decreasing dependence on the sample temperature for all three samples. The 60 nm sample showed the lowest threshold current density, comparable to previously studied CuMnAs layers grown on GaAs [13, 93, 102, 107]. Likewise, the measured threshold current for the 20 nm and 46 nm samples were typical of similar layers grown on GaP [93, 94, 126].

Lines of best fit through $J_{1,2}$ and J_c, shown by the grey dashed lines, reveal the temperature dependence of the threshold current as a function of sample thickness, which is plotted in Figure 4.9a. As the sample thickness increased, the temperature dependence

of the threshold current density had a shallower gradient. Conversely, the interpolated threshold current density at $T = 0$, shown in Figure 4.9b, showed an increase as sample thickness decreased.

4.4 Discussion and conclusion

The CuMnAs layer thickness, sample temperature and current pulse amplitude play a significant role in determining the shape of the magnetoresistance relaxation. Within the explored temperature range, 270 K to 320 K, the relaxation times spanned several orders of magnitude, from fractions of a second to hours. Furthermore, the primary relaxation, which exhibited the largest signal amplitude, showed an increase in size with current pulse amplitude as temperature was lowered. CuMnAs layers grown on GaP(001) produced equivalent signal amplitude temperature dependence, whereas the layer on GaAs was two orders of magnitude smaller.
Whilst the relaxation behaviour was generally universal across the samples, some key differences were identified:

- Threshold current density decreased with increasing layer thickness.
- Signal size was up to two orders of magnitude smaller in the 60 nm layer grown on GaAs.
- Primary and secondary relaxation components of the 46 nm and 60 nm layers were opposite sign, whereas the components of the 20 nm layer were the same sign.
- Decay time of the 20 nm layer relaxation components were an order of magnitude longer than the 46 nm and 60 nm.

The multicomponent relaxation was fitted with a two term Kohlrausch stretched exponential. The first term described the primary relaxation and the second term described the secondary relaxation. A constant offset was included to measure the remnant signal after 250 s, and encompassed relaxation components with relaxation times far exceeding the measurement window. The fit function described the relaxation well, with exponent set to 0.6, reflecting the observed dimensionality of the system. Extracted from the fits were the relaxation times of the two components, which exhibited temperature dependent Néel-Arrhenius behaviour. The relaxation time, interpolated to T =0 K gave the

material dependent attempt time, measured for all three samples to be in the picosecond range, intrinsic of antiferromagnetic spin dynamics.

A complimentary study of electrically pulsed CuMnAs devices provides further evidence that the resistive change and subsequent relaxation immediately after pulsing is associated with changes to AF order [126]. Three magnetic imaging techniques independently revealed current-induced nano-fragmentation and proceeding reformation of AF domains on the timescale of the electrically measured resistive relaxation [112, 127]. The resistive contribution was associated with an increased density of AF domain walls. The mechanism of domain nano-fragmentation was attributed to ohmic heating during the pulse, in proximity of the Néel temperature. However, there is also evidence of NSOT induced 90° reorientation of fragmented domains as well.

Overall, it is difficult to establish the origin of the resistive switching and multicomponent relaxation in tetragonal CuMnAs solely from electrical measurements. Preliminary magnetic imaging has provided some elucidation. However, the precise dynamics of the AF domain reformation from the nano-fragmented state has not been conclusively linked to the resistive signal relaxation. In particular, no conclusions have been made about the origin of the multiple decay components which can have opposite sign, although ubiquitous in complex relaxing systems. A more thorough investigation, using magnetic imaging combined with electrical measurements, is required to confirm the magnetic origin of the relaxing resistive signal.

Chapter 5

Electrical Control of Antiferromagnetic 180° AFDWs

5.1 Introduction

In Chapter 4, electrical current pulses were used to rotate the Néel vector of magnetic domains 90° between magnetic easy axes in CuMnAs. This method of domain manipulation is convenient because changes in the domain population can be measured electrically in the AMR. However, for purposes in high density and low power memory devices, magnetic domain walls (DWs) are better candidates for active components. Racetrack memory is a memory architecture based on moving DWs, using electrical currents, along thin strips [139]. The presence (or absence) of a DW at specific locations, defined by pinning sites or notches along the track, can be encoded into bits of information. The original design was based on ferromagnetic DWs driven by spin-transfer torque and was motivated by many early studies of DW control in ferromagnetic materials [140–144]. However, at high current densities the FM DW velocity becomes limited by the Walker breakdown, which occurs when the driving torque oscillates the DW between Bloch and Neel type [145–149]. This limitation does not exist in AF DWs, because the exchange torque between the magnetic sublattices is much larger than current-induced torques [150]. This leads to stiff AFDWs, with low effective mass, and no breakdown. The effective mass, $M_s \propto {}^1/_{H_{\text{ex}}}$, where H_{ex} is the exchange field. For a 10 nm thick layer of CuMnAs the exchange field was estimated from the canting angle at the spin-flop field $H_{\text{ex}} \sim (700 \pm 200)$ T [129]. The AF DW relaxation time is

also defined, $\tau \propto {}^{1}/_{a_G \gamma H_{ex}}$, where a_G is the Gilbert damping coefficient and γ is the gyromagnetic ratio. The relaxation time is related to the inertial motion of the domain wall after the field is reduced to zero (see Figure 4 of reference [82]). The upper limit of AF DW velocities is determined by the magnon velocity, $c = \gamma\sqrt{{AH_{ex}}/{M_s}}$, which is orders of magnitude faster than in FMs [150–152].

A large body of theoretical work has explored driving AF DWs using various methods, including spin-currents induced by a scanning tunnelling microscope tip [153], spin waves [151, 154, 155], external fields [156–160], electric field induced anisotropy gradients [161], and temperature gradients [162–164]. Current-induced NSOT has been predicted to move AF DWs with high efficiency and high velocity [150, 152, 165, 166]. This was demonstrated experimentally in CuMnAs; using a combination of XPEEM and AMR measurements, the electrical control of 90° DWs was seen [108]. The current density required to drive the DW movements was an order of magnitude smaller than is required for orthogonal switching of magnetic domains in the same material. This reiterates the relevance of AF DWs for low-power spintronic devices.

There have been few examples of 180° DW control in AFs, partly due to a lack of understanding about their contribution to AMR and SHMR measurements, making electrical detection difficult [167]. Recent studies have shown 180° AF DWs driven at speeds up to $750\,\mathrm{m\,s^{-1}}$ via exchange coupling torque in a synthetic AF [168]; manipulated by topographical features and imaged using nitrogen-vacancy centre magnetometry [169]; nucleated, displaced and detected DWs in non-collinear AF, Mn_3Sn [170].

The importance of studying AF DW dynamics extends beyond possible applications. DWs carry information about the magnetic microstructure of materials and can have fundamentally different properties from domains. The widths and separations of AF DWs can indicate about magnetostrictive strains caused by crystal deformations, local defects, and device geometries [169, 171]. There has been a recent observation of atomically sharp AF DWs in CuMnAs, where the Néel vector rotation between opposite domains occurs abruptly over the scale of neighbouring atomic sites [172]. This type of domain wall cannot be described by the continuum micromagnetic theories that predict dynamics and morphology, and could give rise to new interesting physics [126].

In this chapter we show the electrical control of 180° AF DWs in CuMnAs, imaged using XPEEM. DWs are seen to move reversibly between pinning sites, depending on

the applied current pulse amplitude and polarity. The driving mechanism is attributed current-induced NSOTs acting on the DWs.

5.2 Methods

The device design used, as shown in Figure 5.1a, was a 10 µm wide, 150 µm long channel that traverses all crystal axes in a continuous manner. This design means that, for applied current pulses, the current density normal subtends all angles relative to the CuMnAs crystal axes. The magnetic domain structure of the device was expected to be more responsive to current-induced NSOT in sections of the channel where the angle between the effective field and magnetic moments were perpendicular.

The device was made from a 50 nm thick layer of CuMnAs epitaxially grown on GaP(001). Fabrication was done by Jasbinder Chauhan using the procedure outlined in Chapter A. Au contact pads were added for improved electrical contact. The device was mounted onto a pulsing cartridge, designed for XPEEM, using silver paint. Al wire was bonded, using an MPP 4526 wedge wire bonder at Diamond, from the device contact pads to brass pins on the cartridge that connect to Ta feet. The Ta feet allow for electrical contact to be made to the device through the manipulator arm in the XPEEM chamber.

The antiferromagnetic domain structure of the device was imaged using XPEEM combined with x-ray magnetic linear dichroism (XMLD) at the Mn L_3 absorption edge, which shows maximum contrast between domains with Néel vectors collinear and perpendicular to the x-ray linear polarization. By rotating the device with respect to the x-ray beam, the variation in the Néel vector across 180° domain walls can be determined.

5.3 Results

Figure 5.1b and c show an overview image of the antiferromagnetic domain structure in the device for x-ray polarization (cyan double-headed arrows) collinear to along the [100] and [1-10] CuMnAs crystal axes, respectively. The [010] crystal axis corresponds to 45° between the two magnetic easy axes; with x-rays collinear to this axis (Figure 5.1b) the Néel vector rotation between the domains is resolved. 180° domain walls appear as adjacent black and white lines, where the left to right order of the two colours indicates the direction of the Néel vector rotation across the wall. This dipolar contrast

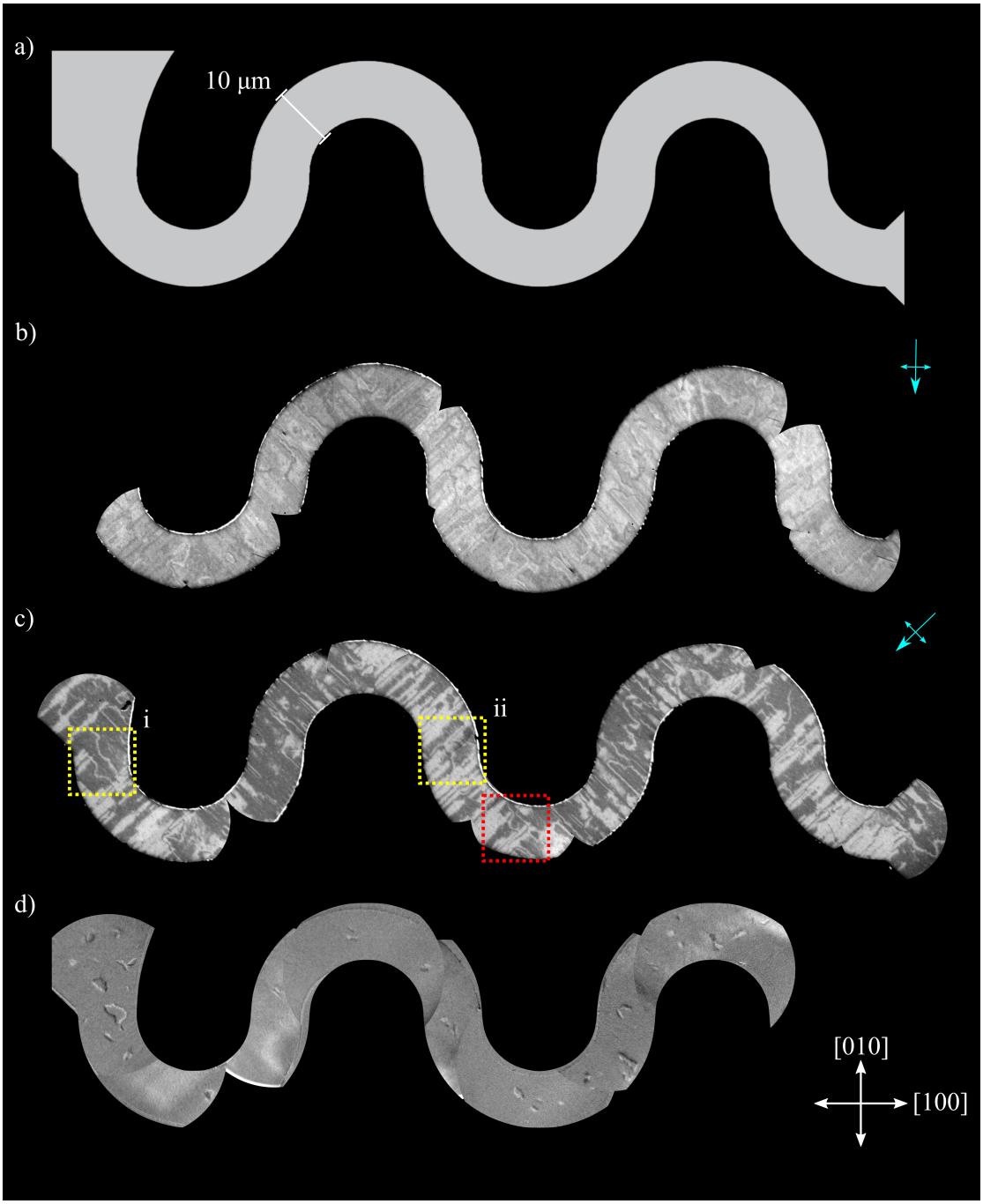

Figure 5.1: 10 µm *wide channel shown a) schematically; b) as* 30 µm *field-of-view stitched XPEEM images with x-ray direction (cyan arrows) along the [010] CuMnAs crystal axis, resolving Néel vector variation in the magnetic domain walls. When the x-ray direction is rotated* 45°*, c), XPEEM images show white and black contrast corresponding to magnetic domains with Néel vector parallel and perpendicular to the x-ray polarization (cyan double headed arrows), respectively. d) shows the difference between XPEEM images after current pulses are applied along the channel, where black and white lines are positions of* 180° *domain walls before and after the pulse, respectively. The red box in c) highlights a region of the channel where a* 180° *domain wall was seen moving between three positions. Yellow boxes highlight two additional regions of the device where* 180° *domain wall movements were observed.*

indicates that the 180° domain walls are Néel type, as the Néel vector in the wall rotates in the plane of the magnetization. When the x-ray direction is along the [-1-

10] crystal axis (Figure 5.1c), the antiferromagnetic domains appear as black, for Néel vector perpendicular to the x-ray polarization, and white when parallel. In this scenario, 180° AFDW centres are also resolved, appearing as thin black or white lines within a contrasting background (domain). The large black and white domains shown in Figure 5.1c indicate that the CuMnAs layer has a biaxial magnetic anisotropy with magnetic easy axes collinear to the [110] and [1-10] crystal axes.

A Keithley 2461 source meter was used to supply 1 ms wide rectangular current pulses through the device. An in-house built relay switchbox was used to control the connection between the source meter and the device contacts. To prevent the device from sparking, the XPEEM high voltage supply is switched off during pulses. The time between pulsing and imaging the device was >30 s, so only persistent current-induced changes to the magnetic domain structure were imaged. Figure 5.1d shows an overview of AFDW movements in the device after applying several current pulses. The overview image was produced by taking the difference between images prior to pulsing and after the pulsing experiment was finished. The white lines in regions of the channel indicate movement of a 180° AFDW to that position. Black lines are positions AFDWs have moved from. The red box in Figure 5.1c highlights a region of the device where a 180° AFDW was seen to reversibly move between three positions; controlled by the current pulse amplitude and polarity.

The region outlined by the red box in Figure 5.1c is shown in Figure 5.2. The sequence of images in Figure 5.2a and c show movement of a 180° AFDW after successive current pulses of varying amplitude and polarity (indicated by the yellow text and arrows). The moving 180° AFDW in Figure 5.2a appears as a vertical white line on a black domain. The Néel vector of the black domain points perpendicular to the x-ray polarization (cyan double headed arrow), along the [110] crystal axis. The Néel vector of the white 180° AFDW centre points parallel to the x-ray polarization, along the [1-10] crystal axis. The first image in the sequence shows the 180° AFDW at its starting position. After a 28 mA, 1 ms pulse (yellow arrow) is applied along the [100] direction, the AFDW moves to a "fully closed" position, shown in the second image. A 10 mA pulse with opposite polarity causes the AFDW to move back to its starting position. When a 15 mA pulse is applied again along the [100] direction, the AFDW moves from the starting position to an intermediate position, shown in the fourth image. A subsequent 28 mA pulse in

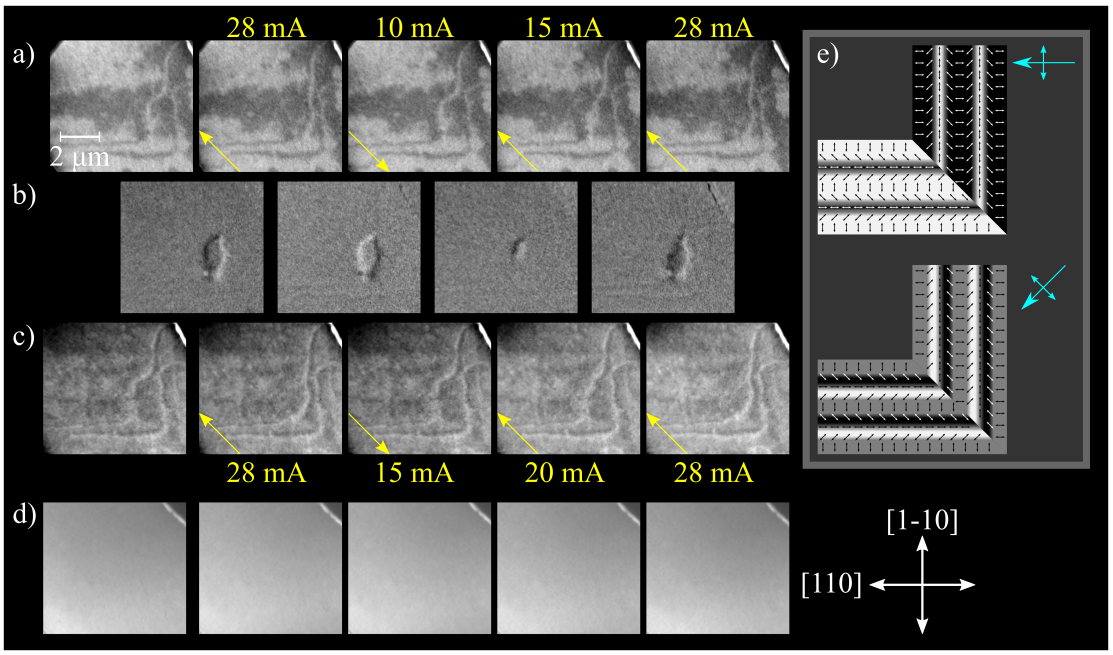

Figure 5.2: *XPEEM images of the region highlighted by the red box in Figure 5.1c, with x-ray direction (cyan arrows) along the a) [-1-10] crystal axis and c) [010] crystal axis. White and black contrast in a) shows magnetic domains with Néel vector oriented parallel and perpendicular to the x-ray polarization (cyan double headed arrows), respectively.* 180° *AFDWs are also resolved as white or black lines on a contrasting background. When the x-ray direction is rotated* 45°*, as shown in c), Néel vector variation across AFDWs is resolved. The sequence of images in a) and c) show a* 180° *AFDW moving between three positions dependent on the polarity and amplitude of the current pulse, directed along the [100] and [-100] axes. The differences between XPEEM images in a) are shown in b), where black and white lines correspond to positions the* 180° *AFDW moves from and to, respectively. Absorption images for the sequence of images in a) are shown in d). The illustrations in panel e) show the Néel vector variation across two parallel, horizontal and vertical* 180° *AFDWs, and the corresponding black/white contrast for the two x-ray directions.*

the same direction moves the AFDW from the intermediate position to the fully closed position.

Figure 5.2b shows the difference between the sequence of XPEEM images in Figure 5.2a. The black and white lines indicate positions the AFDW moves to and from, respectively. Inverted contrast between the first and second image of Figure 5.2b show the reversible movement of the AFDW after current pulses of opposite polarity. The AFDW movements were seen in an isolated $\sim 4\,\mu m^2$ region of the device.

Figure 5.2c shows the same sequence of AFDW movements as in Figure 5.2a, but with x-rays incident along the [010] crystal axis. The vertical 180° AFDWs are seen, from left to right, as white/black. It is inferred from the order of the colour (white/black) for the moving AFDW that the Néel vector rotates anitclockwise through 180°. Absorption images in Figure 5.2d show the device surface structure at the region of interest. Flat and uniform contrast indicates that no surface structure changes occur during the puls-

ing sequence and AFDW pinning is not due to surface defects. However, the pinning sites are attributed to local bulk defects, possibly caused by crystal deformation which cause magnetostrictive strains [171]. Illustrations of the Néel vector rotation across the AFDWs, with resulting XPEEM contrast, are shown in Figure 5.2e.

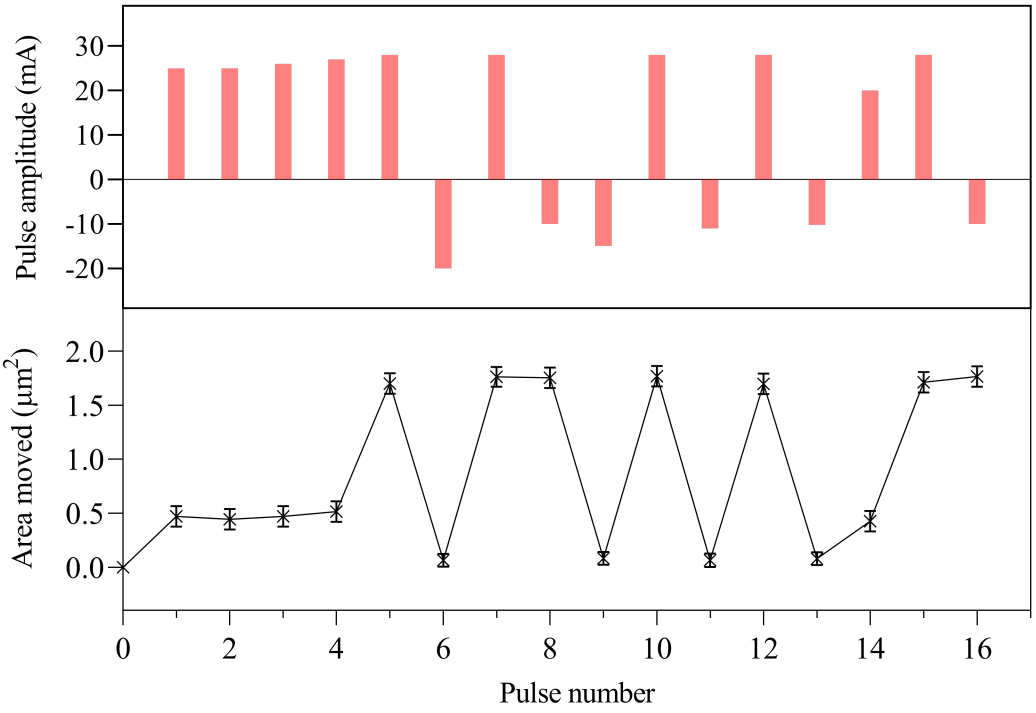

Figure 5.3: *Area moved by the* 180° *AFDW shown in Figure 5.2 during a sequence of 16,* 1 ms *current pulses. Positive current amplitude corresponds to current direction along the [100] crystal axis, and negative amplitude along the [-100]. The AFDW moves between three positions depending on the current pulse amplitude, and is moved in the opposite direction by reversing the pulse polarity.*

The area moved by the 180° AFDW with reference to its starting position was measured during a sequence of 16 current pulses of varying amplitude and polarity (see section 5.3.2). The top plot in Figure 5.3 shows applied current pulse amplitude, with positive amplitude (polarity) corresponding to current direction along the [100] crystal axis, and negative amplitude along the [-100] axis. The bottom plot in Figure 5.3 shows the area moved by the AFDW relative to its starting position during the pulse sequence. The intermediate position at $\sim 0.5\,\mu m^2$ is achieved for current pulse amplitudes $+20\,mA < I < +28\,mA$ and the fully closed position for amplitudes $\geq +28\,mA$. Negative pulse polarity required currents as low as 10 mA ($\sim 2.5 \times 10^{10}\,A\,m^{-2}$) to move the AFDW back to the starting position. Temperature increase during the 10 mA current pulse is

less than 10 K, as indicated by finite element calculations discussed in Section 5.3.3.

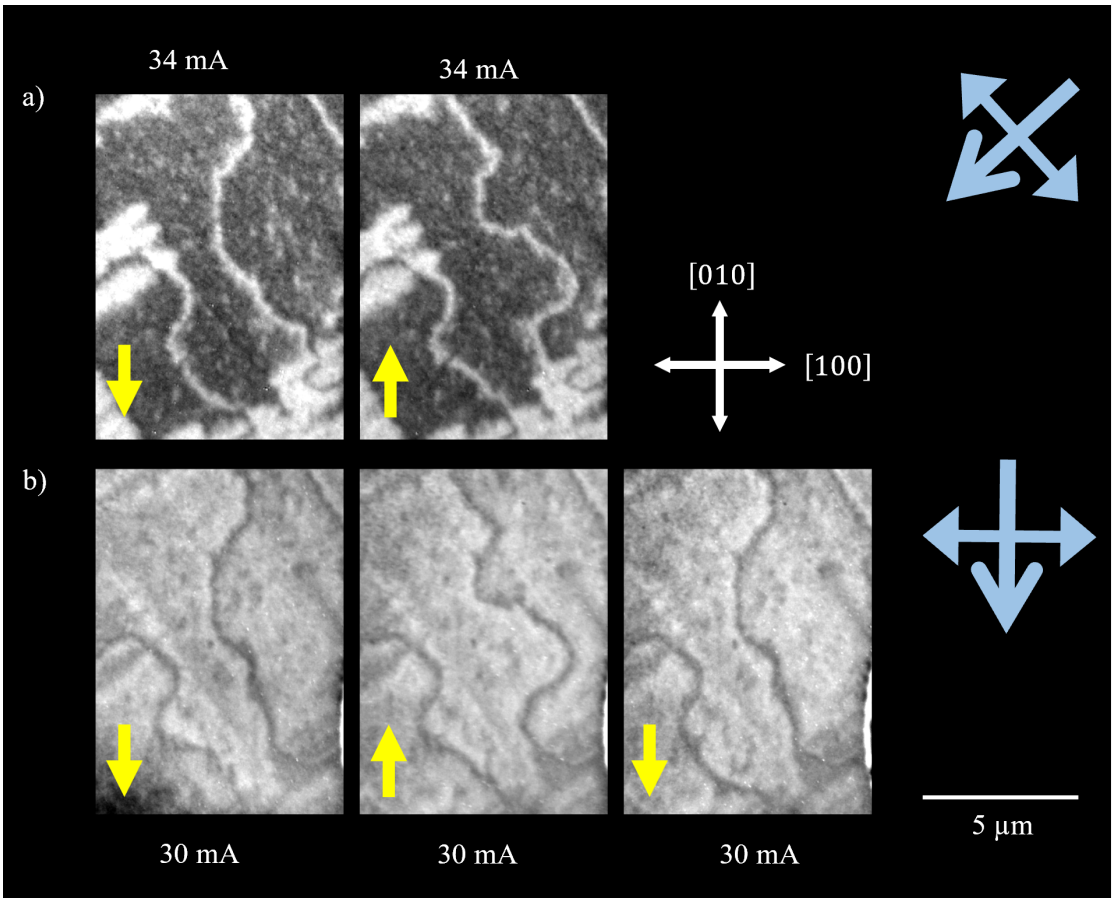

Figure 5.4: *Position i highlighted by the yellow box in Figure 5.1c.* 180° *AFDWs move dependent on the polarity of the applied current pulse (yellow arrows). Images taken with x-ray polarization collinear to the [1-10], a), show magnetic domains as black and white contrast, whereas x-ray polarization collinear to the [100] show AFDWs as dipolar with black and white contrast for either side of the wall.*

There were two additional regions of the device where current-induced reversible 180° AFDW movements were observed. These correspond to the areas, i and ii, highlighted by yellow boxes in Figure 5.1c. Figures 5.4 and 5.5 show the imaged sequence of movements at each position. The maximum AFDW displacement in all cases was ∼2 µm.

Current-induced thermal gradients, local heating and magnetoelastic effects can cause changes to magnetic domain structure in antiferromagnets. However, these effects are independent of the current polarity and would not produce reversible AFDW motion. Instead, the proposed driving mechanism for the polarity-dependent 180° AFDW motion is field-like NSOTs, as discussed in the next section.

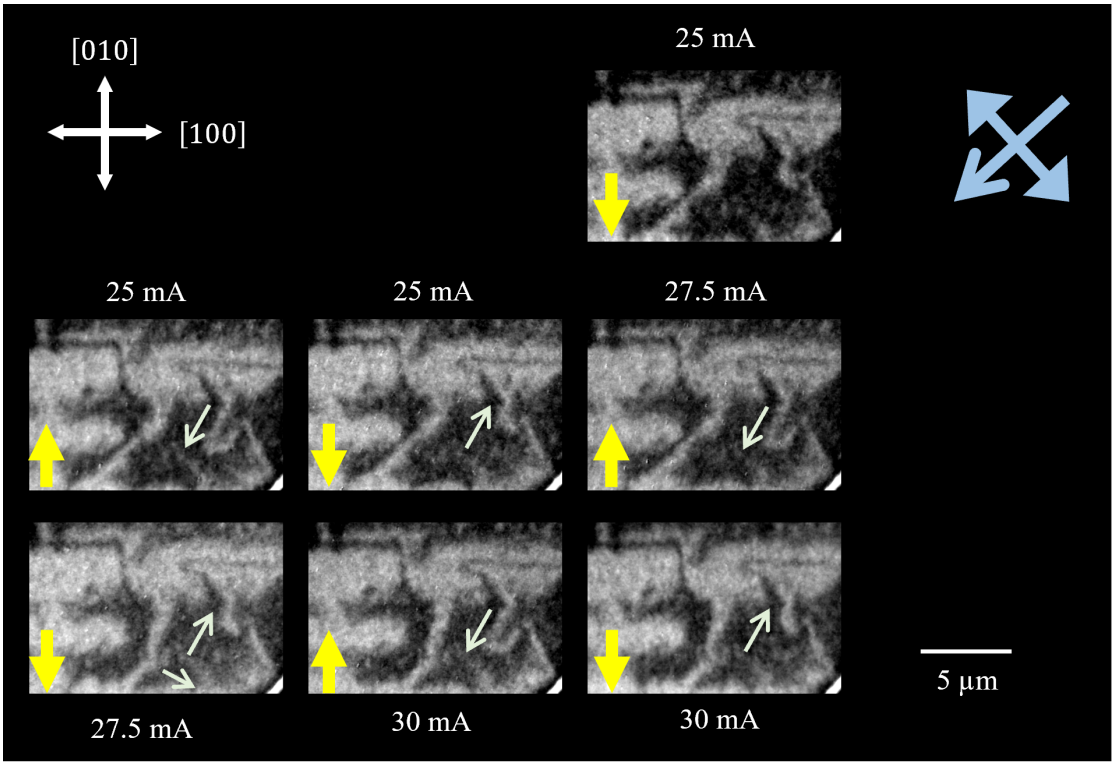

Figure 5.5: *Position ii highlighted by the yellow box in Figure 5.1c. Movement of a* 180° *AFDW (light green arrows) dependent on the polarity of the applied current pulse (yellow arrows).*

5.3.1 Domain wall driving mechanism

Figure 5.6 shows an illustration of the energy density across 180° AFDW configurations under the action of a current pulse. The current-induced effective magnetic field $\boldsymbol{B}_{\text{eff}}$ is perpendicular to the current direction and alternates sign between the two magnetic sublattices. The Zeeman energy of the spins is $E = -\boldsymbol{M} \cdot \boldsymbol{B}_{\text{eff}}$, where $\boldsymbol{M}$ is the sublattice magnetization vector. The resulting field-like NSOT is $\boldsymbol{T} \sim \boldsymbol{M} \times \boldsymbol{B}_{\text{eff}}$. A ponderomotive force, as a result of the NSOT, drives the AFDW towards the domain with higher energy. When the current pulse direction is reversed, the effective magnetic field changes sign on both sublattices, generating the opposite ponderomotive force on the AFDW. In the case of the current pulse direction parallel or antiparallel to the domains either side of the AFDW, the energy density favours no movement; instead, the AFDW would expand or contract.

5.3.2 Domain wall tracking in MATLAB

The area moved by the 180° AFDW in Figure 5.2 was measured computationally using MATLAB R2020b. XPEEM images with x-rays incident along the [110] crystal axis were used so that the Néel vector in the centre of the AFDW appears white and the

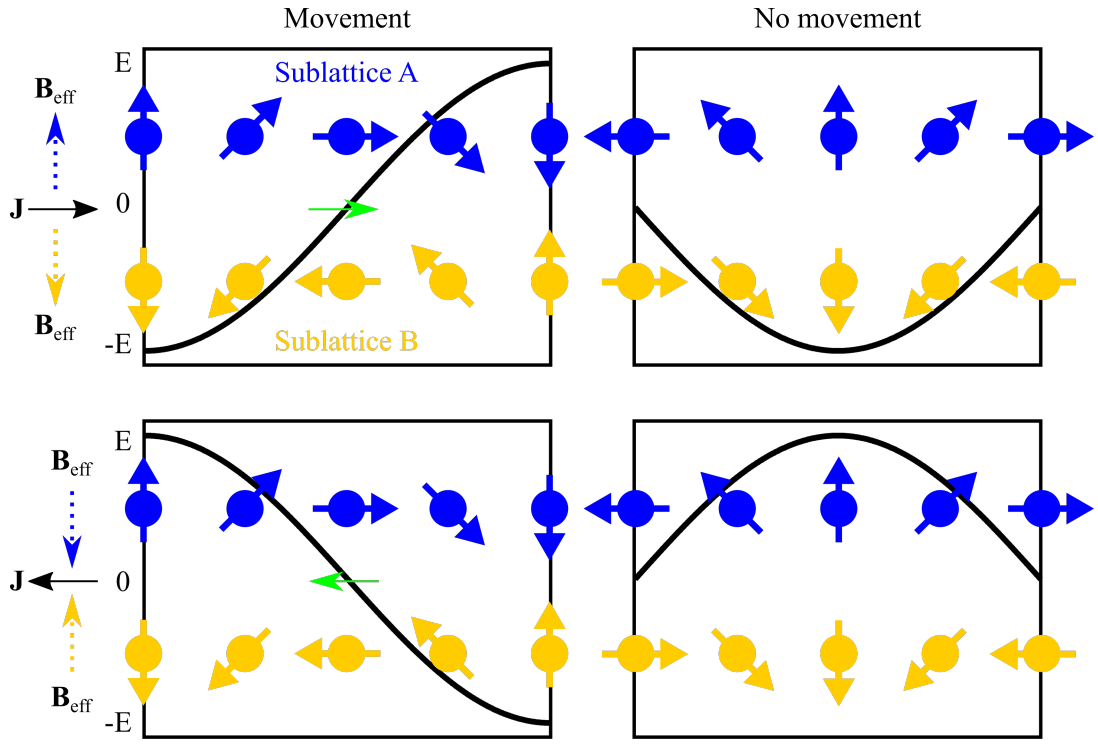

Figure 5.6: *Antiferromagnetic* 180° *AFDW configurations which exhibit movement and no movement with an applied current pulse,* $\boldsymbol{J}$*. The current pulse generates a staggered effective magnetic field* $\boldsymbol{B}_{eff}$*, on the magnetic sublattices, which produces a ponderomotive force that drives the AFDW towards the high energy side (indicated by green arrows). The direction of the movement is opposite with reversed pulse polarity. In the case of no movement, the current pulse lower/raises the AFDW energy, causing it to expand/contract.*

domain as black. A user defined polyline was traced over the AFDW in each image using the MATLAB function *drawpolyline*. Straight line segments of the polyline were bisected by $5n$ equally spaced lines of length $\sim$ 14 pixels. The pixel values of the bisectors were averaged in n batches to give 5 mean line profiles of the AFDW along each straight line segment of the polyline. These line profiles were fitted with a single term Gaussian of the form $a \cdot \exp\left\{-\frac{(x-b)^2}{2c^2}\right\}$, where a is the Gaussian amplitude, b is the centroid coordinate, and c is the standard deviation relating to the peak width. The AFDW centre coordinate for each line profile was taken as b, with error in the position given by c. This gave a more accurate detection of the AFDW position when compared with just using the user defined polyline trace.

MATLAB's *polyarea* function was used to calculate the area moved by the AFDW relative to the starting position. This was repeated four times with a ± 2 pixel shift in the AFDW coordinates in the x and y axes, and the average of repeats was taken. The purpose of the pixel shift was to account for any alignment offset between images. The mean area in pixels^2 was converted to µm^2 using the pixel width of the channel; 58.8

pixels $\sim 10\,\mu m$, so that $1\,\mu m^2 \sim 2.9 \times 10^{-4}$ pixels^2. The errorbars in the bottom plot of Figure 5.3 were calculated as the error on the mean area.

5.3.3 Finite element modelling of current-induced heating in the channel

A model of the Joule heating in the device was created by Luke Barton in the commercial finite element analysis package, COMSOL Multiphysics. A 3D geometry of the device on top of the substrate was constructed, as shown in Figure 5.7, consisting of a 50 nm thick, 10 µm wide CuMnAs channel on top of an 800 µm (in $\hat{x}$) × 500 µm (in $\hat{y}$) × 300 µm (in $\hat{z}$) GaP block. Within the 10 µm wide device, a free triangular mesh of minimum length, 160 nm, is swept through $\hat{z}$ to produce five coupled 2D mesh layers in the device. The GaP substrate has a free tetrahedral mesh with 160 nm length at the interface with the device, and 80 µm length away from small features to minimise computational load. Due to limits in the mesh size, the device was modelled without a 2.5 nm Al capping layer; this assumes conduction occurs entirely within the 50 nm CuMnAs channel. The geometry environment is a high vacuum, with a pressure of 1×10^{-9} mbar to simulate similar pressure achieved in the XPEEM chamber.

COMSOL's proprietary Electromagnetic Heat Source Multiphysics couples solutions to the Electric Currents (EC) physics PDE with variables in the Heat Transfer (HT) in Solide physics PDE. In the former, the PDE to solve is a static equation of the form

$$\nabla \cdot \boldsymbol{J}_\mathrm{c} = -\nabla \cdot (\sigma \nabla V - \boldsymbol{J}_\mathrm{e}) = 0, \tag{5.1}$$

where $\boldsymbol{J}_\mathrm{c}$ is the conduction current density in the bulk of the device, σ is the scalar electrical conductivity, V is the electric potential being solved for, and $\boldsymbol{J}_\mathrm{e}$ is the externally generated current density. Using a static equation for the electric currents is justified as the external time scale (1 ms pulse width) and time step resolution (0.1 ms) are much larger than the charge relaxation time. Boundary conditions for the EC module were set such that an inward normal current density with a top-hat function of width 1 ms and amplitude 28 mA enters the material at one flat side surface and exits at the other, which is set to ground. All other faces for both the device and chip are electrically insulating with boundary conditions $-\boldsymbol{n} \cdot \boldsymbol{J}_\mathrm{e} = 0$.

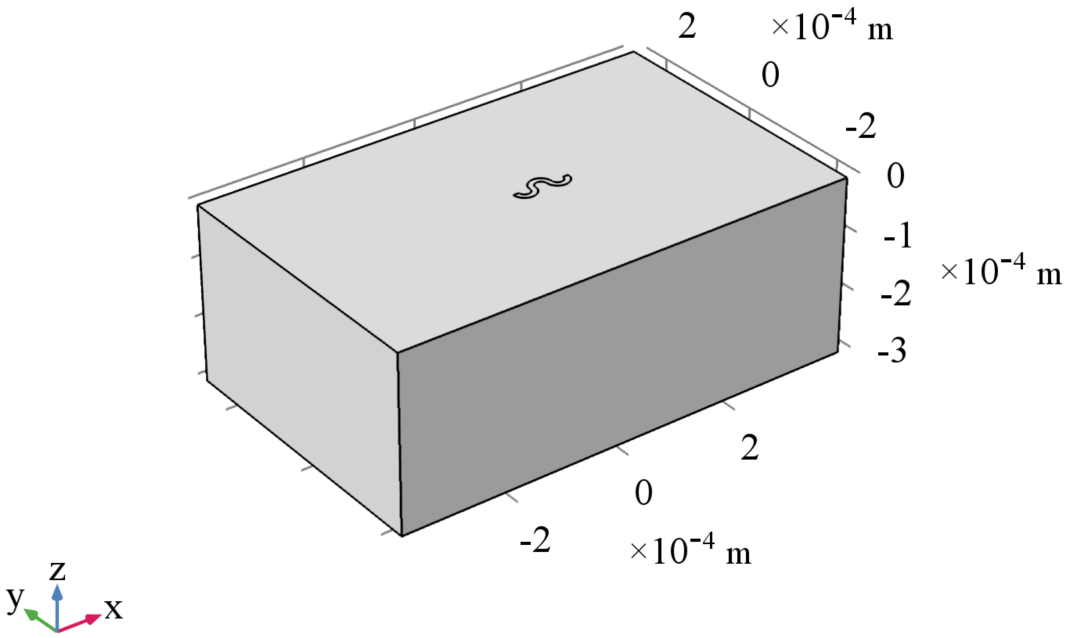

Figure 5.7: *A schematic of the device and substrate COMSOL geometry used for finite element calculations. The* 10 µm *wide channel device,* 50 nm *thick, and* 90 µm *long, was situated in the centre of the top surface of the substrate. The substrate dimensions were* 800 µm *in* $\hat{x}$, 500 µm *in* $\hat{y}$, *and* 300 µm *in* $\hat{z}$. *A free triangular mesh of minimum length* 160 nm *was used for the channel. A tetrahedral mesh was used for the substrate with* 160 nm *length at the interface with the device, and* 80 µm *away from small features. The environment was set to high vacuum conditions of pressure* 1×10^{-9} mbar.

The PDE to solve for the HT is the heat equation of the form

$$\rho C_p(\frac{\partial T}{\partial t}) + \nabla \cdot (\boldsymbol{q} + \boldsymbol{q}_\mathrm{r}) = \boldsymbol{Q}, \tag{5.2}$$

where ρ is the material density, C_p is the specific heat capacity in vacuum, $\boldsymbol{q} = -k\nabla T$ is conductive heat flux at the interface between the device and substrate, and $-\boldsymbol{n} \cdot \boldsymbol{q}_\mathrm{r} = \epsilon\sigma(T^4_{\mathrm{ambient}} - T^4)$ is the radiative heat flux, normal to the surface, between the device and the environment (σ here is the Stefan-Boltzmann constant). $\boldsymbol{Q}$ defines a power source coupled to the conduction current density by the Joule heating relation $\boldsymbol{Q} = \boldsymbol{J}_\mathrm{c} \cdot \boldsymbol{E}$, where $\boldsymbol{E}$ is the electric field. The bottom surface of the GaP substrate is defined as insulating because heat transfer from the bottom surface via conduction is negligible. All domains have an initial temperature of 293.15 K.

The system remains at equilibrium for the first 1 ms of the study. The current pulse

Table 5.1: Material constants used for the CuMnAs device and GaP substrate in COMSOL's coupled Electric Currents and Heat Transfer PDE solver.

Constant	Symbol	CuMnAs value	GaP value	Units
Electrical conductivity	σ	5.05×10^5	1×10^{-6}	S/m
Specific heat capacity	C_p	350	430	J/(kg·K)
Material density	ρ	6960	4140	kg/m^3
Thermal conductivity	k	100	110	W/(m·K)
Relative emissivity	ϵ	0.1	0.1	

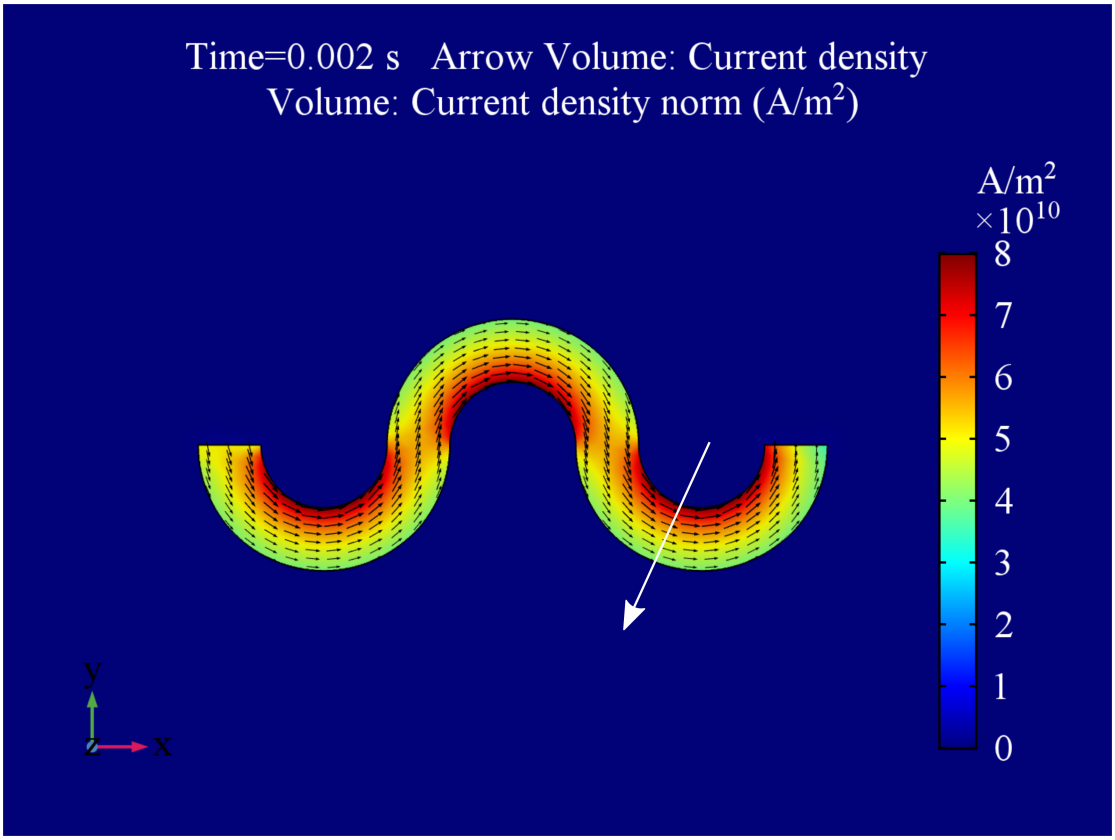

Figure 5.8: *Solutions to the Electric Currents PDE in the* 10 µm *wide channel during the last time step of a* 1 ms, 28 mA *pulse. The current density is shown as a heat map and overlayed quiver plot. Highest current density is measured on the inside bend of the channel. The white arrow shows the line profile through the position of the device corresponding to the region in which the three stage moving AFDW was seen.*

is then simulated from 1 ms to 2 ms, after which the system is allowed to equilibrate towards ambient conditions. The temporal resolution of the study is 0.1 ms. The heat map snapshot (Figure 5.9) of the device during the last time step (2 ms) of the current pulse shows the maximum temperature reached (380 K) due to Joule heating. The temperature gradient along the white dashed line is shown in Figure 5.12. The current density along the same line profile (Figure 5.12) shows a maximum at the inside bend of the channel. Despite this, the temperature reached at the point of maximum current density is lower than the maximum, because of thermal dissipation from the inside

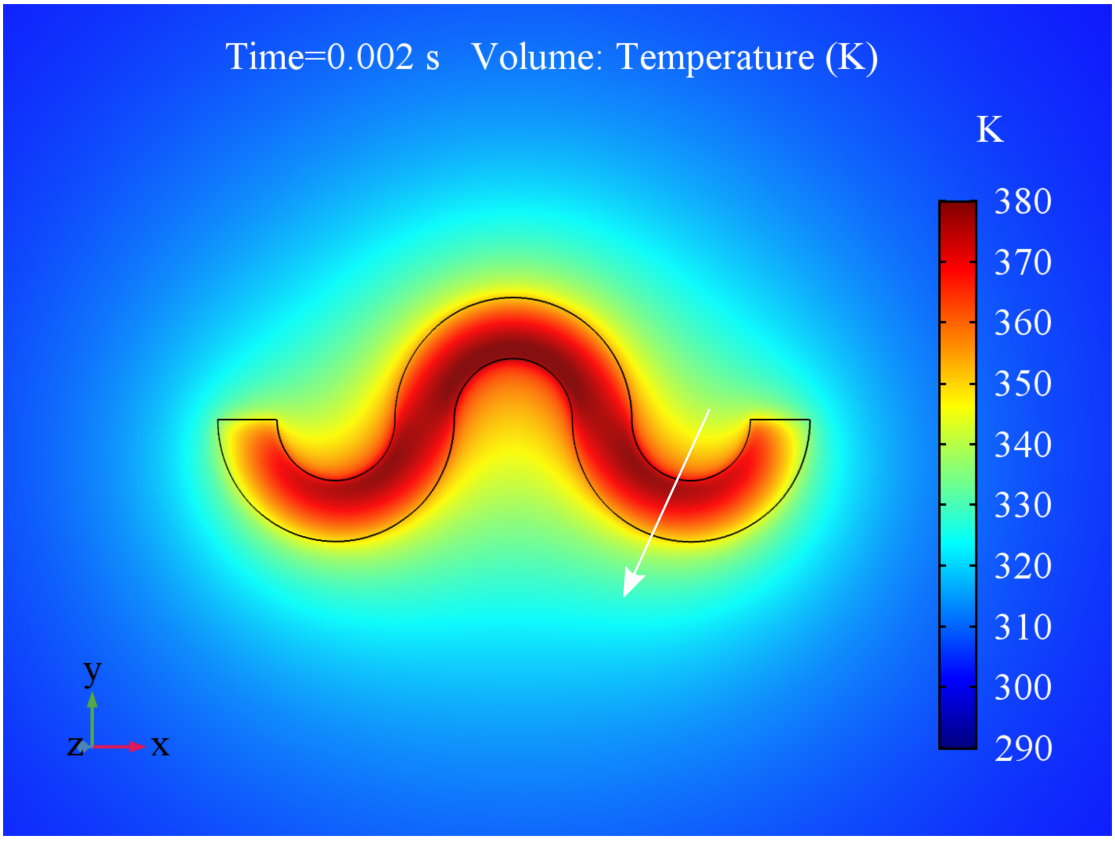

Figure 5.9: *Solutions to the Heat Transfer PDE shows Joule heating in the* 10 µm *wide channel during the last time step of a* 1 ms, 28 mA *pulse. Thermal dissipation via conduction can be seen in the surrounding substrate.*

face to the environment. Within one time step after the current pulse the device and substrate already cool to 300 K.

The maximum temperature reached in the device was measured for varying current pulse amplitudes. Figure 5.13 shows COMSOL solutions to the HT PDE at pulse current amplitudes from 5 mA to 30 mA. The maximum temperature was measured during the last time step of the current pulse, so that cumulative heating is taken into account. The current amplitude dependence of the maximum temperature was fitted with a polynomial function of the form $a \cdot I^2 + 293.15$, where $a = 1.1 \times 10^{-1}\,\mathrm{K/mA^2}$, I is the current amplitude, and the offset 293.15 K is the ambient temperature of the system. Thus, there is a linear dependence of the maximum temperature reached and input power from the current pulse, $P \propto \rho I^2$, where ρ is the material resistivity. Figure 5.13 shows that for a 1 ms pulse, the lowest current pulse amplitude, of 10 mA, required to move the AFDW heats the device to a temperature of ∼307 K and the maximum applied pulse amplitude of 30 mA heats the device to ∼395 K. This is well below the 480 K Néel temperature expected of this material, demonstrating that magnetic domain

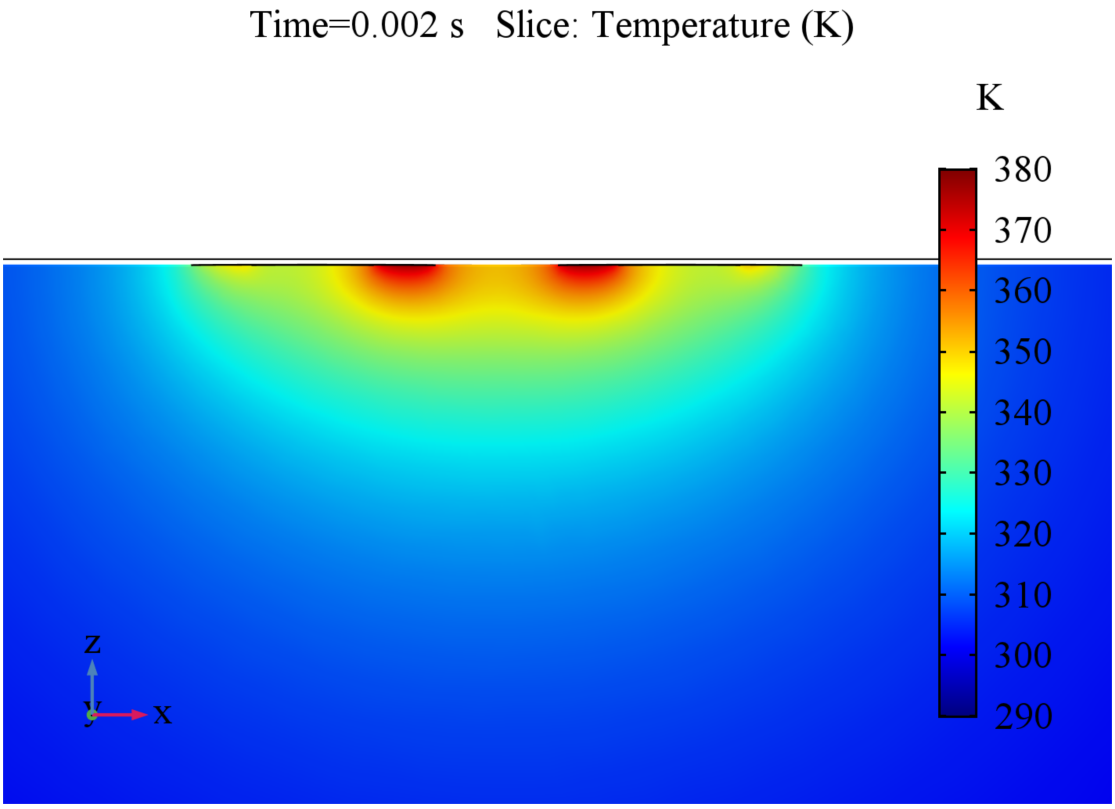

Figure 5.10: *Side profile view of the heat map shown in Figure 5.9. Thermal conduction between the device and the substrate interface causes heat to dissipate into the bulk of the substrate.*

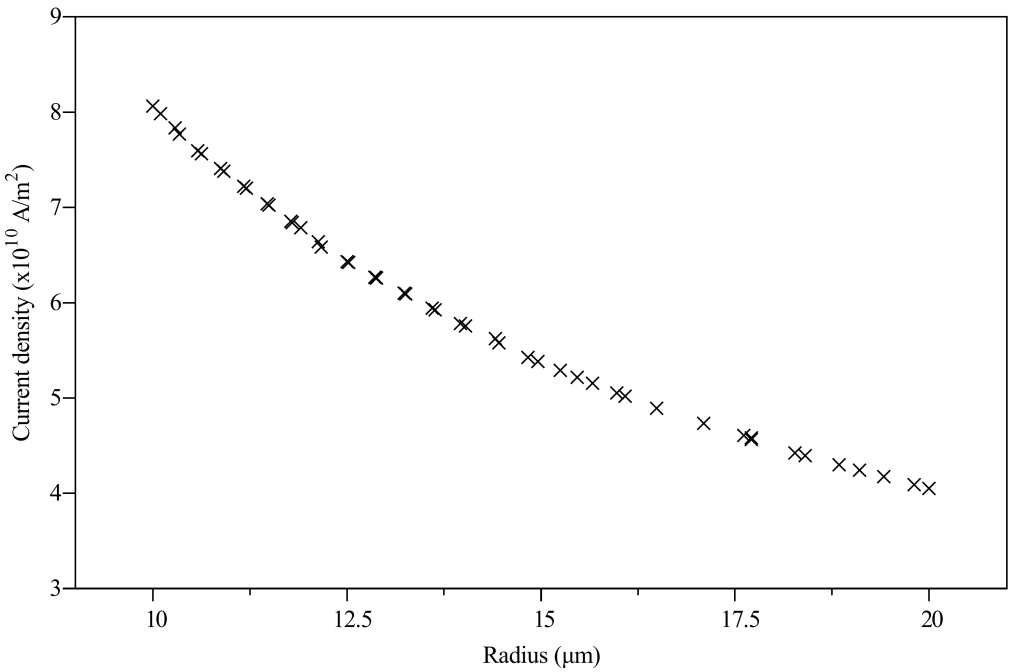

Figure 5.11: *Current density measured along the line profile indicated by the white arrow in Figure 5.8. The radial length is referenced from the centre of the arc.* 10 µm *on the line profile corresponds to the inside bend of the channel where the current density is maximum. This section of the channel is the region in which the three stage AFDW movements were seen.*

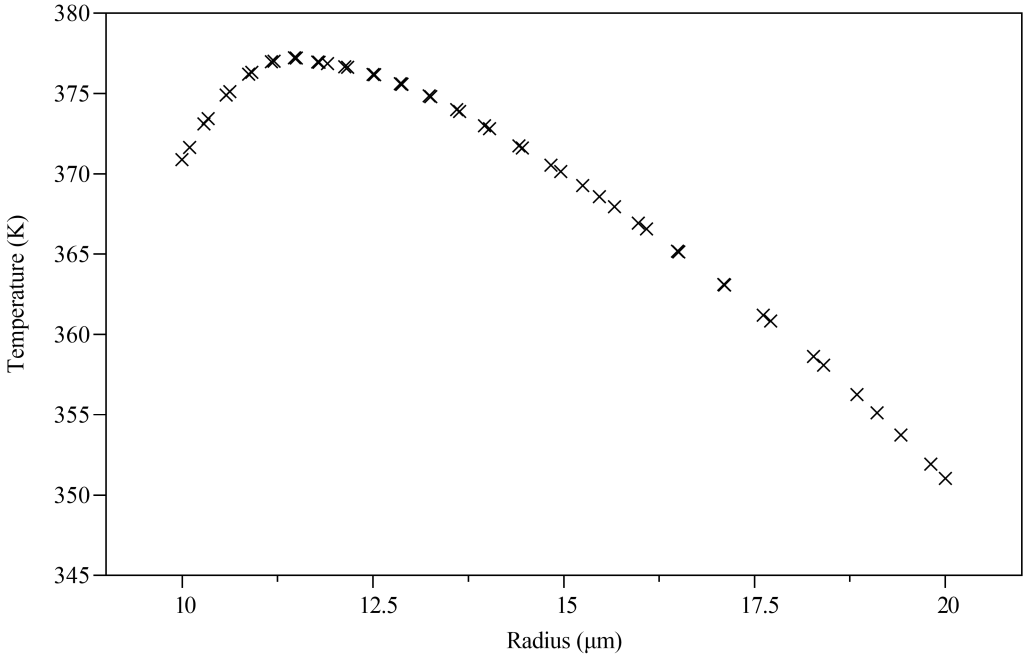

Figure 5.12: *Temperature measured along the line profile indicated by the white arrow in Figure 5.9. The radial length is referenced from the centre of the arc. The inside bend of the channel is the point of maximum current density, but not maximum temperature because thermal dissipation via radiation occurs from the inside face of the device to the environment.*

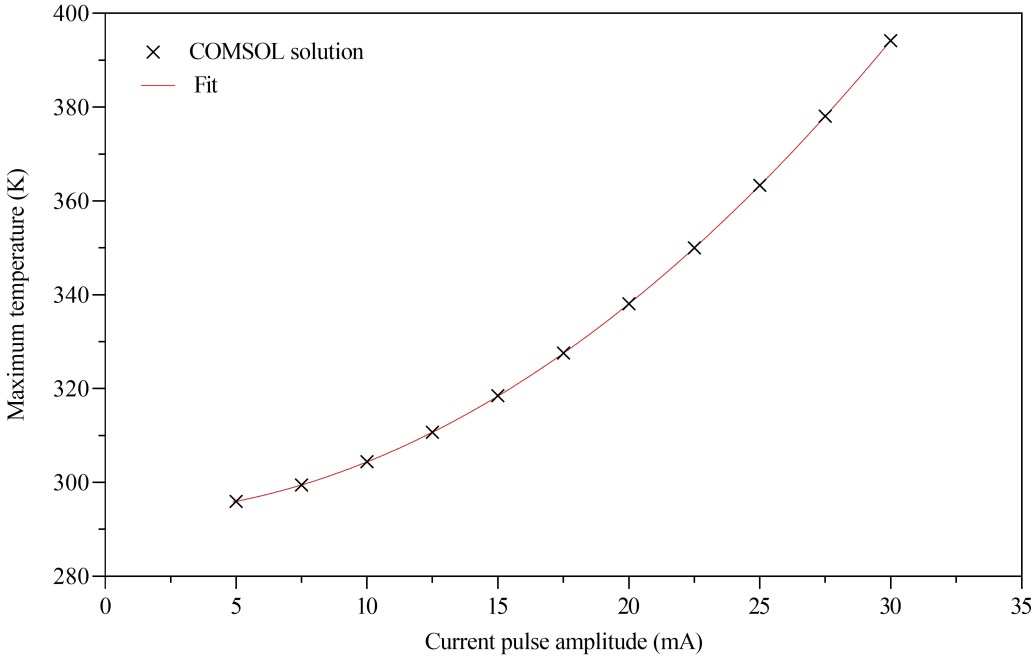

Figure 5.13: *Measured maximum temperature reached in the device during* 1 ms *current pulses of amplitudes* 5 mA *to* 30 mA*. The COMSOL solutions were fitted with a second order polynomial of the form* $a \cdot I^2 + 293.15$*.* $a = 1.1 \times 10^{-1}\,\mathrm{K/mA^2}$*,* I *is the current amplitude, and the offset* 293.15 K *is the ambient temperature of the system.*

changes in the device are not simply due to heating. Instead, heating during the applied current pulse contributes to depinning the AFDWs and NSOT determines the direction in which they move.

5.4 Conclusion

The results shown demonstrate the ability to controllably move 180° AF DWs using current pulses. NSOT, which arises due to the particular crystal symmetry of CuMnAs, lifts the degeneracy between domains rotated 180°. The resulting energy gradient across the 180° AFDW drives it in the direction towards the higher energy domain. Joule heating during the current pulse was calculated to be well below the Néel temperature, and the pulse polarity dependent movements of the DW cannot be explained by temperature gradients because they are independent of the current polarity.

Device geometry and local defects are known to induce magnetostrictive strains that cause DW pinning [169, 171]. The DW movement shown happens between three such pinning sites which have different depinning current density thresholds. Further investigation into engineering pinning sites is required to understand the mechanism that causes them.

Overall, this work confirms the prediction of AF DWs driven by NSOT [150]; it corroborates the existence of NSOT in CuMnAs; and it sets the starting point to further study 180° DW dynamics in AF materials.

In terms of applications, control of AF DWs is considered an important goal for future memory architectures, such as racetrack memory. AFs offer many benefits over FMs for high speed, high density memories and their micromagnetic dynamics are not restricted by dipole interactions or weak exchange fields.

Chapter 6

Electrical Generation and Control of Antiferromagnetic Vortices

6.1 Introduction

Magnetic vortices, also called half-skyrmions or merons, are planar whirls in the magnetic texture of in-plane magnetized samples with a core spin directed out of the sample plane [173–180]. They constitute the smallest possible magnetic texture, with size controlled by the magnetic exchange and anisotropy. A characterizing feature of magnetic vortices is their topological charge, Q, a conserved quantity that provides them protection against defects and perturbations, as well as enormous stability even at small sizes [181–184]. The topological charge is analogous to a winding number, which is an integral of the solid angle swept out by the vortex spins. Written as a function of the magnetization field, $\boldsymbol{m}$,

$$Q = \frac{1}{4\pi} \iint \boldsymbol{m} \cdot \left(\frac{\partial \boldsymbol{m}}{\partial x} \times \frac{\partial \boldsymbol{m}}{\partial y}\right) \mathrm{d}x \, \mathrm{d}y \,, \tag{6.1}$$

which is more usefully written in terms of the azimuthal angle, θ, and polar angle, Φ, of spins at radial coordinate $\mathbf{r} = r(\cos\phi, \sin\phi)$,

$$Q = \frac{1}{4\pi} \int_0^1 \mathrm{d}r \int_0^{2\pi} \sin(\theta(r)) \frac{\mathrm{d}\theta(r)}{\mathrm{d}r} \frac{\mathrm{d}\Phi(\phi)}{\mathrm{d}\phi} \, \mathrm{d}\phi = -\frac{\cos(\theta(r))}{2}\Big|_{r=0}^{r=\infty} \cdot \frac{\Phi(\phi)}{2\pi}\Big|_{\phi=0}^{\phi=2\pi}. \tag{6.2}$$

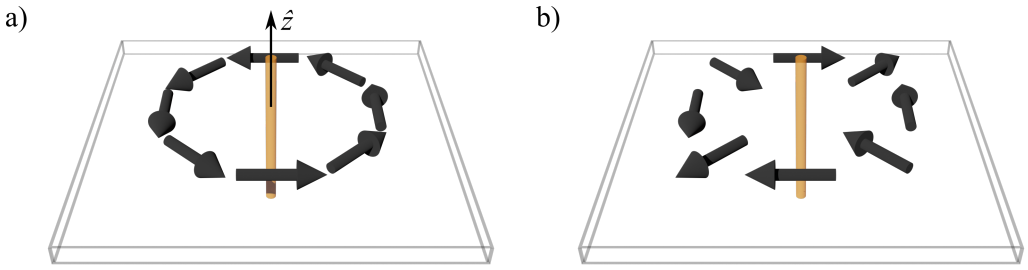

Figure 6.1: *Illustrations of Bloch-type vortices, with spins (black arrows) rotating in the sample plane. Vortex, a), and anti-vortex, b), have opposite vorticity. The vortex polarity depends on the direction of the core spin (orange cylinder) along the $\hat{z}$ direction. If the vortex and anti-vortex have opposite polarity, their topological charges are equivalent.*

On the right-hand side, the first term is the vortex polarity,

$$p = -\frac{\cos(\theta(r))}{2}\Big|_{r=0}^{r=\infty} = \pm\frac{1}{2}, \tag{6.3}$$

which measures the out-of-plane spin component at the core compared to the surroundings. The second term is the vorticity,

$$m = \frac{\Phi(\phi)}{2\pi}\Big|_{\phi=0}^{\phi=2\pi} = \pm 1, \tag{6.4}$$

which evaluates the in-plane rotation of the spin along a circular path surrounding the core. Thus, for a magnetic vortex, a fractional polarity and integer vorticity gives a topological charge of $\pm\frac{1}{2}$, earning the name half-skyrmion.

There is a third classifier called the helicity, $\gamma = \Phi - m\phi$, a constant offset in-plane spin rotation, which does not contribute to the topological charge, but differentiates Néel and Bloch-type vortices [179]. Figure 6.1 shows illustrations of a Bloch-type vortex, a), and anti-vortex, b), characterized by opposite vorticities and a helicity of $\frac{\pi}{2}$. Following an anticlockwise path around the core, it can be seen that the spins rotate in the same sense for the vortex, and in the opposite sense for the anti-vortex. Given the case where the core spins point in opposite directions, the vortex and anti-vortex have equivalent topological charges.

Vortices are one type of many non-trivial topological magnetic textures that have been identified [179, 183, 184]. They have generated significant interest in recent years due to desirable properties for spintronic applications. They exhibit particle-like behaviour and can be driven to high velocities using current-induced spin orbit torque and spin

transfer torque. Furthermore, their topological charge gives rise to an emergent electrodynamic signature, the topological Hall effect, which can be used to electrically detect their presence [185–187]. This makes them ideal candidates for low power, high-density, high-speed memory applications, as has been proposed with racetrack nanodevice architectures [188–191].

Ferromagnets (FMs) have, so far, been the primary source of experimental studies of magnetic vortices. In circular dot geometries, with sub-micron diameter, fabricated from ferromagnetic thin films [176, 192–194] and multiferroic heterostructures [195], vortices are stabilized in the absence of an externally applied field. It has been demonstrated that, in these geometries, the vortex polarity can be switched using ac currents [196–199], and the vortex can be gyrated around an equilibrium position when driven at resonance [200, 201].

Other systems exhibit vortices in less confined geometries. In permalloy nanowires, subjected to current pulses, vortex domain walls were nucleated, displaced, and annihilated [144, 202, 203]. A different system, thin film $Co_8Zn_9Mn_3$, which is a chiral FM, exhibited a vortex/anti-vortex lattice phase under the action of an out-of-plane external magnetic field [204]. Similar vortex lattices in Pt/Co/Ta trilayers were driven by current-induced spin transfer torque and the vortex paths were traced out using magneto-optical Kerr microscopy. This revealed the dependence of the skyrmion Hall angle, a transverse deflection of the vortices from the current direction, on the thickness of the Co layer [187].

A plethora of studies have demonstrated the localization of vortices on magnetic 180° domain walls in several different systems, which were manipulated with the application of an external magnetic field [205–207]. Observations of this kind are not restricted to ferromagnetic materials and have also been demonstrated in synthetic AFs. Layers of Co, antiferromagnetically exchange coupled across a non-magnetic Ru spacer layer via Ruderman-Kittel-Kasuya-Yosida (RKKY) coupling, showed current- and laser pulse-induced generation of vortices [208], as well as magnetic field induced nucleation of domain wall vortices which responded dynamically as the field strength was increased [209].

Interest in AF vortices is swelling, as their properties are especially appealing for spintronic applications. AFs have no dipole field, which inhibits the stability of the smallest

size vortices in FMs [183, 184, 210–212]. The antiparallel sublattice magnetization results in a net-zero topological charge which absents the deleterious skyrmion Hall effect deflecting vortices driven by electrical currents. Furthermore, they can be driven at velocities an order of magnitude faster than in their ferromagnetic counterparts, due to large exchange stiffness and inherent terahertz spin dynamics [150, 213, 214].

Progression of AF vortices has been limited by few methods of nucleation. In FMs, external magnetic fields can be used to generate vortices. However, compensated sublattice magnetizations in AFs makes them intractable to external influences. Instead, early studies relied on a ferromagnetic layer to imprint, via exchange coupling, vortex structures into AF thin films [215–217]. Recently, α-Fe_2O_3, a naturally occurring AF insulator, was shown to stabilize merons and bimerons by temperature cycling through the Morin magnetic transition temperature without the need of external fields or exchange coupled layers [210, 218]. This was a promising step for AFs as candidate materials to host vortices, but it is impractical for memory device applications.

In this chapter, experimental results showing the room temperature nucleation and manipulation of AF vortices using electrical pulses in CuMnAs are presented. This is the first definitive example of vortices in a conductive AF thin film which are usable as bits in memory device applications.

6.2 Methods

To identify the AF vortices, we used powerful, high-resolution magnetic imaging technique, X-ray magnetic linear dichroism combined with photoemission electron microscopy (XMLD-PEEM). The x-rays were incident at a grazing angle of 16° to the sample surface with linear polarization vector in the plane of the sample. Maximum XMLD contrast was achieved with x-ray energy tuned to the Mn $L_{2,3}$ edge.

A 50 nm layer of CuMnAs, epitaxially grown on GaP(001) and capped with 3 nm of Al, was patterned into a 4-arm cross device with 10 µm arm width using photolithography and chemical wet etching. The device arms were aligned along the [100] and [010] CuMnAs crystal axes. Once loaded into the PEEM chamber, in situ 1 ms electrical voltage pulses were applied, using a Keithley 2461 Source Meter Unit, between the device contacts. After each pulse, XMLD-PEEM images were taken to identify electrically induced changes to the micromagnetic structures. The process of acquiring XMLD-

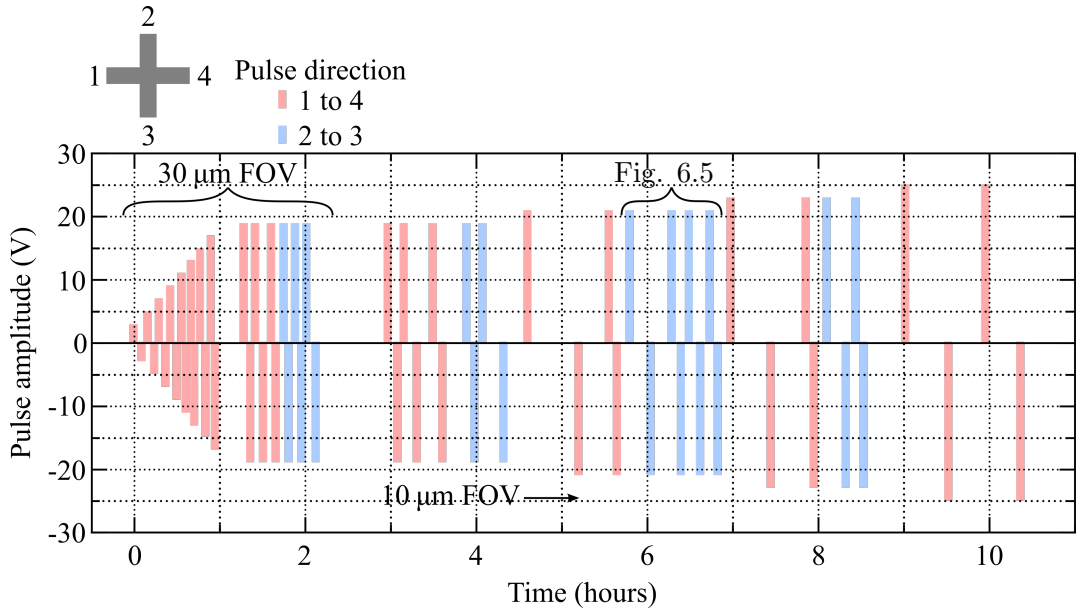

Figure 6.2: *Timeline of* 1 ms *voltage pulses applied between contacts 1 and 4, horizontal (red), and 2 and 3, vertical (blue) arms of the device. Negative pulse amplitude corresponds to pulses of opposite polarity. After each pulse was applied, XMLD-PEEM images of the device were taken to identify changes to the micromagnetic structure. Sections of the timeline are annotated with image FOVs, as well as the set of pulses corresponding to images shown in Figure 6.5.*

PEEM images after the pulse took > 5 minutes, therefore, only non-transient magnetic changes were imaged.

Figure 6.2 shows the timeline of the device pulsing. All pulses were 1 ms wide, with varying amplitude. Negative pulse amplitude corresponds to pulses of opposite polarity. The red bars indicate pulses applied along the horizontal arms of the device, between contacts 1 and 4, as shown by the top left schematic. Blue bars are pulses along the vertical arm of the device, between contacts 2 and 3. For the first ∼2 h of the experiment, XMLD-PEEM images taken after each pulse were 30 µm field-of-view (FOV) and >200 nm magnetic structures were resolved. The device was pulsed several times, along the horizontal and vertical arms, with an amplitude of 19 V before the imaging FOV was reduced from 30 µm to 10 µm, and smaller magnetic structures, >50 nm were resolved.

6.3 Results

Figure 6.3 shows composite 10 µm FOV XMLD-PEEM images of the device centre, with x-ray polarization (cyan double-headed arrow) collinear to the [1-10] CuMnAs axis. In this configuration the device appears as majority uniform grey contrast. Stripe domains, generated by microtwin defect lines along the [110] and [1-10] axes, appear as white and

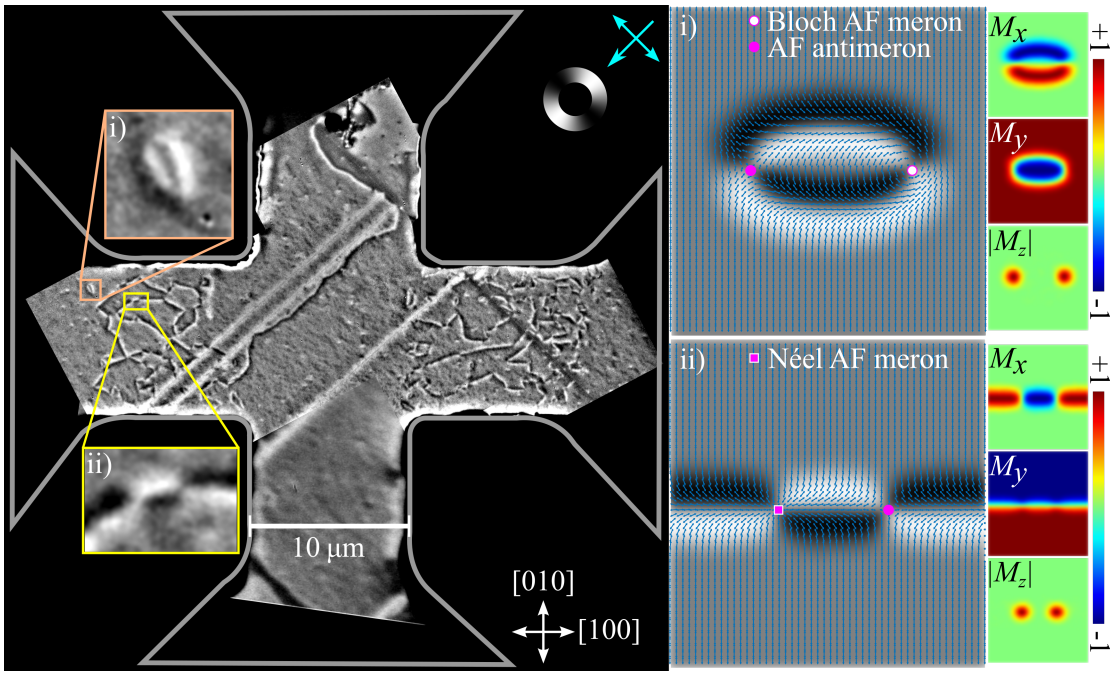

Figure 6.3: *Composite XMLD-PEEM images showing AF domain structure in the 4-arm device with* 10 µm *arm width, fabricated from a* 50 nm *layer of CuMnAs epitaxially grown on GaP(001). Linearly polarized x-rays are incident with polarization vector (cyan double-headed arrow), in the sample plane, collinear to the [1-10] CuMnAs axis. In conjunction with Figure 6.4b, the uniaxial magnetic anisotropy, with preferential alignment of Néel vector parallel to the [010], is determined. Variation of the Néel vector orientation forms prominent magnetic structures: stripe domains, driven by microtwin defect lines along the [110] and [1-10] axes, appear as white and black contrast, corresponding to Néel vector orientation perpendicular and parallel to the x-ray polarization, respectively; and* 180° *AFDWs are seen as characteristic adjacent thin white and black lines. AF vortices are localized on* 180° *AFDWs in the horizontal arms of the device, at points of chirality reversal. Two AF structures that host vortices are highlighted by yellow and orange boxes and shown enlarged in inset images, i) and ii). Corresponding simulated XMLD-PEEM images, Néel vector maps and sublattice magnetization,* $\boldsymbol{M}$*, are present in the panels on the right.*

black contrast, corresponding to Néel vector orientation perpendicular and parallel to the x-ray polarization, respectively. 180° AFDWs are seen as characteristic adjacent thin white and black lines, ∼200 nm in width.

When the x-ray polarization is rotated, collinear to the [100] axis, the device appears majority black, as shown in Figure 6.4b, with grey contrast stripe domains and thin white lines indicating the central spin of the 180° AFDWs, oriented parallel to the x-ray polarization. It is inferred from both image configurations of the device that the magnetic anisotropy is uniaxial with preferential alignment of domains along the [010] CuMnAs axis.

In the horizontal arms of the device, there is a high density of 180° AFDWs. At points where the AFDW chirality reverses, seen in Figure 6.3 as a sudden transition from white/black to black/white (and vice versa), AF vortices are localized. For two example structures, shown in the inset images i) and ii), these were simulated using a Kinetic Monte Carlo algorithm with estimate values for the CuMnAs exchange, uniaxial and cubic anisotropy strengths. The expected XMLD-PEEM images with simulated Néel vector maps, overlayed, are shown in the corresponding right-hand panels. The closed AFDW loop consists of isolated Bloch meron and antimeron pair with characteristic $+\pi/2$ helicity and +1 and -1 vorticity, respectively. The 180° AFDW, with rotational axis in the vertical direction and chirality reversal in the horizontal direction, forms a Néel-type meron and antimeron, with 0 helicity and +1 and -1 vorticity, respectively. Heatmaps of the x, y, and absolute z-components of the sublattice magnetization, $\boldsymbol{M}$, are plotted alongside the vector maps. The absolute z-component, $|M_z|$, reveals an out-of-plane spin orientation at the vortex core, not determinable in the XMLD-PEEM imaging configuration. The out-of-plane core determines the vortex polarity and endows the structure with topological protection.

Figure 6.4a shows XMLD-PEEM images of the horizontal arms and central region of the device after applying 1 ms voltage pulses in the directions indicated by the yellow arrows. The application of 21 V ($1.2 \times 10^7\,\mathrm{A\,cm^{-2}}$) in the [-100] direction causes a reconfiguration of the micromagnetic state in the device arms and displacement of the 180° AFDW in the central region (top right image). Note that the current density is approximately 60% in the centre of the device due to current spreading, as estimated by finite element calculations. Highlighted by the red box, the generation of conjoined AFDW loops is

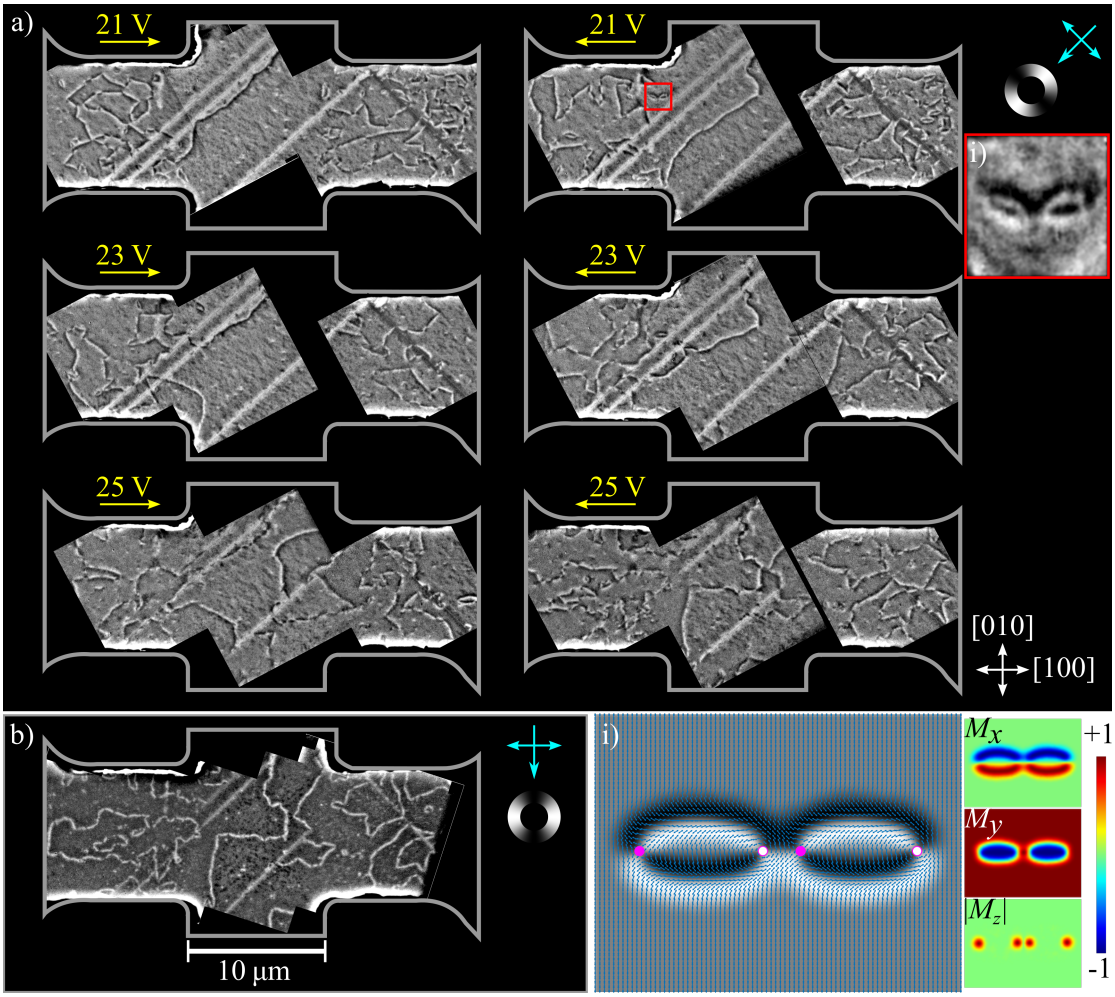

Figure 6.4: *a) XMLD-PEEM images of the horizontal arms and central region of the device after application of* 1 ms *voltage pulses in the directions indicated by the yellow arrows. After application of a* 21 V *(*1.2×10^7 A cm^{-2}*) pulse in the [-100] direction, conjoined* 180° *AFDW loops are formed, outlined by the red box in the top right image. A zoom-in view of the structure is shown in the inset image, i), and corresponding simulated version shown in the bottom panel, i). Rotating the incident x-ray direction by* 45°*, b), reveals black and white contrast between the domains, with Néel vector orientation along the [010], and* 180° *AFDW central spins, respectively. The AF state shown in b) was imaged after completion of the pulsing sequence and is commensurate with the bottom right image in a).*

identified. The neighbouring inset image, i), shows a zoom-in view of the magnetic structure. Corresponding simulated XMLD-PEEM image and vector map are plotted in the bottom right panel, i). At the point where the two loops join, a vortex/antivortex pair is localized in close proximity. The structure resembles a topologically non-trivial bimeron, with the condition that the relative polarities of the vortex cores is opposite. If the polarities are equal, then the Néel topological charges compensate ($Q = 0$), and the structure is topologically trivial.

Figure 6.5 shows the top arm of the device during a sequence of 1 ms, 21 V pulses applied along the vertical direction with alternating polarity. The top left XMLD-PEEM image shows the micromagnetic structure in the pristine state before pulses were applied. A 180° AFDW can be seen pinned between two transverse microtwin defects. After application of a 21 V pulse along the [0-10] axis, AF vortices are generated and localized on the AFDW. Subsequent 21 V pulses of alternating polarity cause the AF vortices to move reversibly along the length of the AFDW, between pinning sites.

In the sixth XMLD-PEEM image in the sequence, a section of the 180° AFDW is outlined by a green box. The zoomed-in view of the highlighted region is shown to the right with corresponding simulated XMLD-PEEM image and Néel vector map. In this configuration, with the AFDW extending in the [010] direction, the vortex pair formed at points of chirality reversal are Bloch-type, as determined from their vorticity.

6.3.1 Vortex tracking

Figure 6.6 shows the steps taken to locate vortex positions in the sequence of XMLD-PEEM images in Figure 6.5. This was done using MATLAB R2020b. The XMLD-PEEM images were read as matrices of values $-1 < I < 1$, where I is pixel intensity, and -1 and $+1$ correspond to maximal darkest and brightest pixel contrast. At each index in the image matrix, surrounding pixels that fall within an annulus with inner radius 2.5 pixels and outer radius 5 pixels are found. Figure 6.6a shows an example search area (red ring) surrounding a vortex. The pixel values within the search area are averaged in the radial direction.

Plotted in Figure 6.6d is the mean pixel intensity as a function of the radial angle, θ, (going anticlockwise) relative to the positive vertical axis of the image. The data was fitted with a function of the form $A_1 \sin\left(\frac{2\pi}{A_2}\theta + A_3\right) + A_4$, where A_1 is the amplitude,

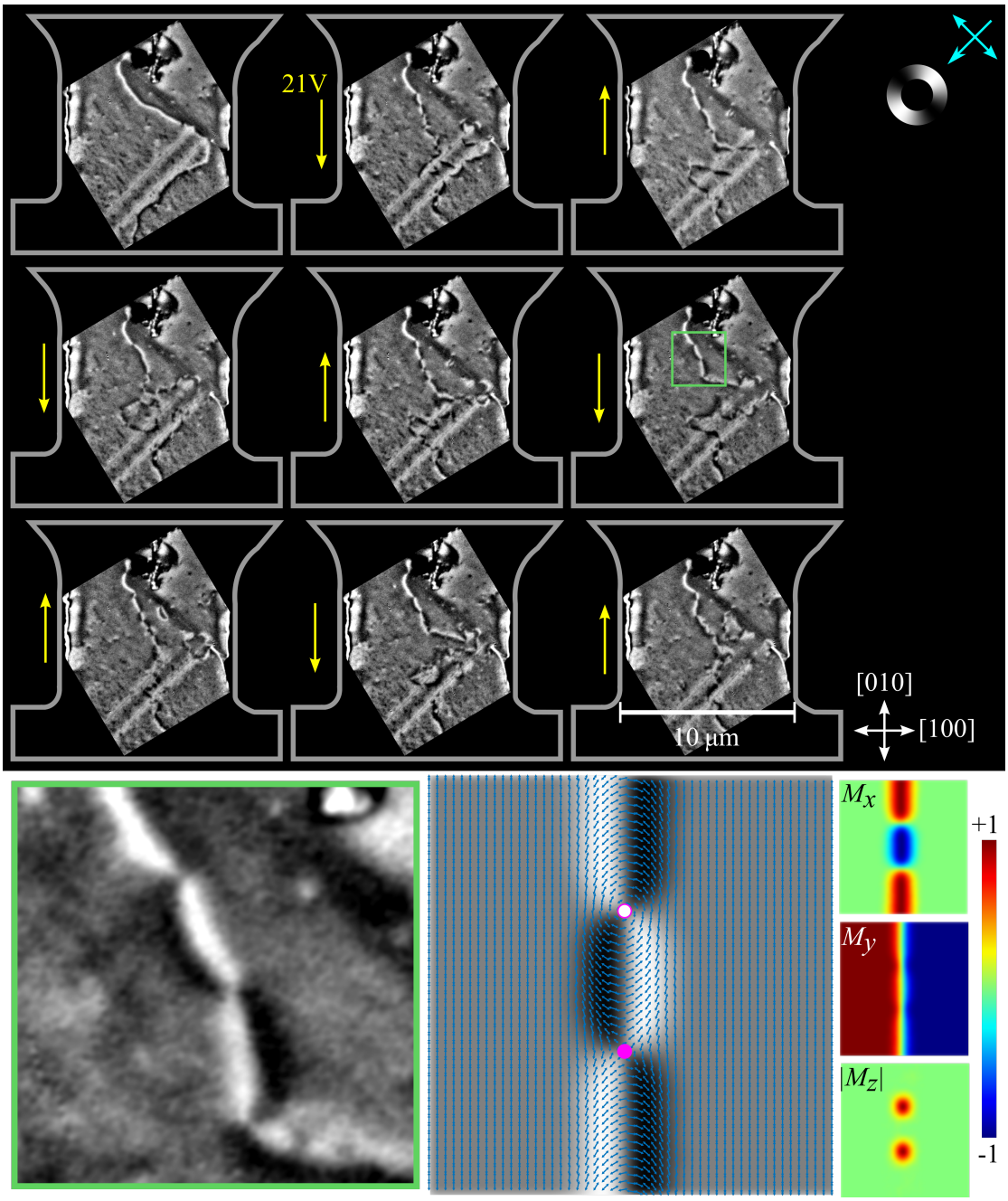

Figure 6.5: *XMLD-PEEM images of the top arm of the device during a sequence of* 1 ms, 21 V *(*1.2×10^7 A cm^{-2}*) pulses applied along the vertical direction (yellow arrows). The pristine state is shown in the top left image. After application of a pulse in the [0-10] direction, the* 180° *AFDW generates AF vortices, localized at points where the AFDW chirality reverses. Subsequent pulses with alternating polarity cause the AF vortices to move along the length of the AFDW. In the sixth image, a section of the AFDW with localized AF vortices is highlighted by the green box. A zoom-in view and corresponding simulated version are presented to the right.*

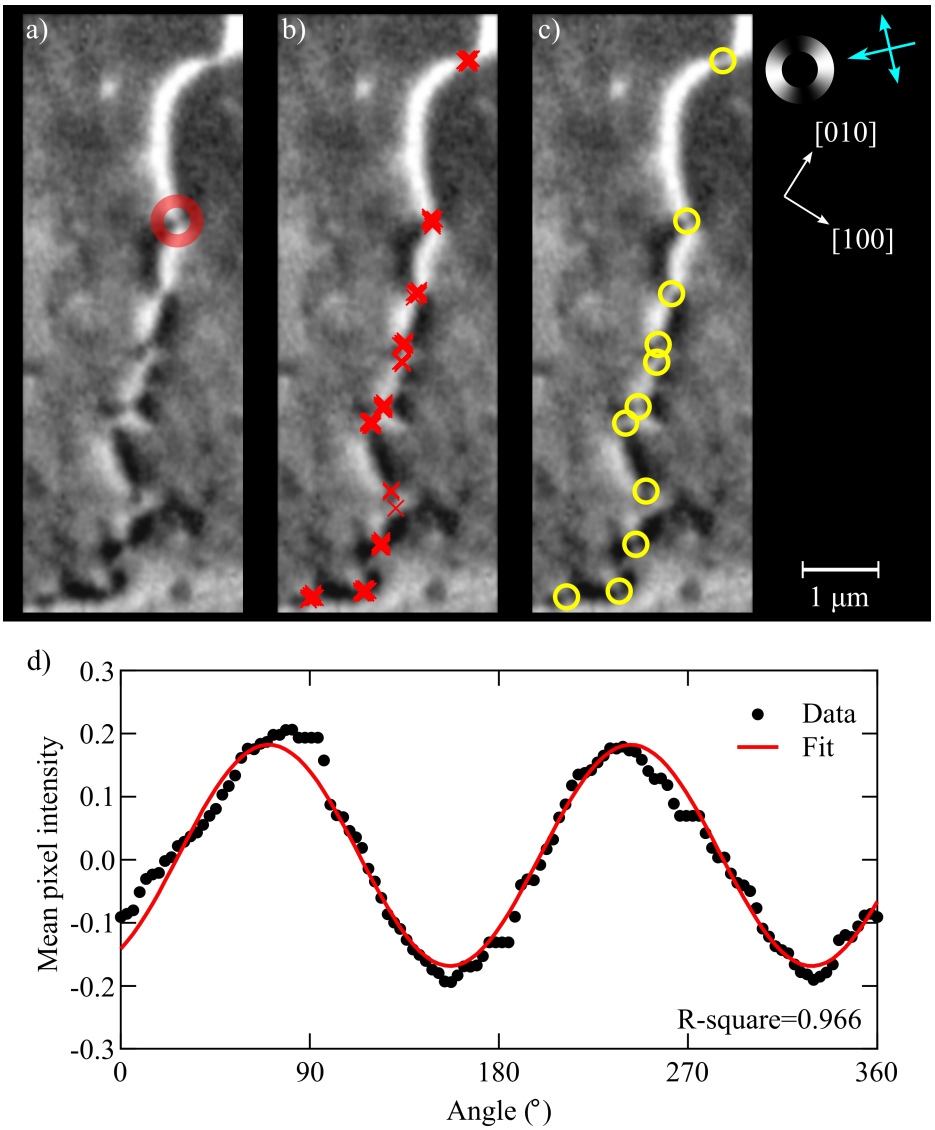

Figure 6.6: *Steps to identify AF vortices from the XMLD-PEEM images shown in Figure 6.5. a) an annulus with inner radius of* 2.5 pixels *and outer radius of* 5 pixels *bounds a search region around a pixel of interest. The radial mean pixel intensity is taken for pixels within the annulus and shown plotted in d). Satisfying the conditions outlined in the main text, the pixel is accepted as corresponding to a vortex. Accepted pixels are shown plotted as red crosses in b). The centroid coordinates of clusters of accepted pixels are taken as the vortex centres, shown plotted in c). Note that the XMLD-PEEM images in a) to c) are rotated* 32° *clockwise from the perspective shown in Figure 6.5.*

A_2 is the period, A_3 is a phase offset, and A_4 is a vertical offset from 0. This function was chosen to locate vortices because the surrounding pixel values should vary in this way, corresponding to a reversal in the AFDW chirality. This process was repeated iteratively for every pixel in the image matrix.

Pixels were associated with a vortex if the fitting parameters satisfied the following conditions, determined empirically: the amplitude, $\frac{I_{max}-I_{min}}{10} \leq A_1 \leq \frac{I_{max}-I_{min}}{3}$; the period, $1.9\pi \leq A_2 \leq 2.1\pi$; and the goodness of the fit, R-square > 0.92, where R-square $= 1 - \frac{\text{SSE}}{\text{SST}}$, given SSE $= \sum_{i=1}^{n}(I_i - \hat{I}_i)^2$ is the summed square of residuals, and SST $= \sum_{i=1}^{n}(I_i - \bar{I})^2$ is the sum of squares about the mean. The index, i, refers to the data point number in Figure 6.6d, $\hat{I}_i$ is the mean pixel intensity calculated by the fit at index i, and $\bar{I}$ is the mean mean pixel intensity. Pixels satisfying the conditions are shown plotted as red crosses in Figure 6.6. The centroid coordinates of clusters of >3 pixels within 1 pixel distance from each other were taken as vortex centres. Figure 6.6c shows the vortex centre positions indicated by yellow rings.

The AF vortex movements are considered in more detail in Figure 6.7. The XMLD-PEEM images in Figure 6.7a show a cropped view of the 180° AFDW during the pulsing sequence. Using methods outlined above, the centroid coordinates of the top four vortices were tracked. The vortices were identified between subsequent images in the pulsing sequence by coloured circles, shown in Figure 6.7a. Plotted in Figure 6.7b are the corresponding change in the centroids x, [010], and y, [100], coordinates, Δx and Δy. The plots show reversible and repeatable movement of the AF vortices dependent on the polarity of the applied voltage pulse. Larger movement is seen in the x direction, commensurate with the pulse direction.

6.4 Discussion and conclusion

The dynamics of the topological AF vortices, under the action of a current-induced spin torque, can be described by Thiele's equation [219–221], with the generalized force due to the current given by

$$\mathcal{M}^{ij}\ddot{b}_j + \alpha\Gamma^{ij}\dot{b}_j = F^i. \tag{6.5}$$

Here the b_j are the collective coordinates of the topological spin structure, $\mathcal{M}^{ij}$ is the mass tensor, and $\alpha\Gamma^{ij}$ characterizes the viscous friction. The gyrotropic forces on each

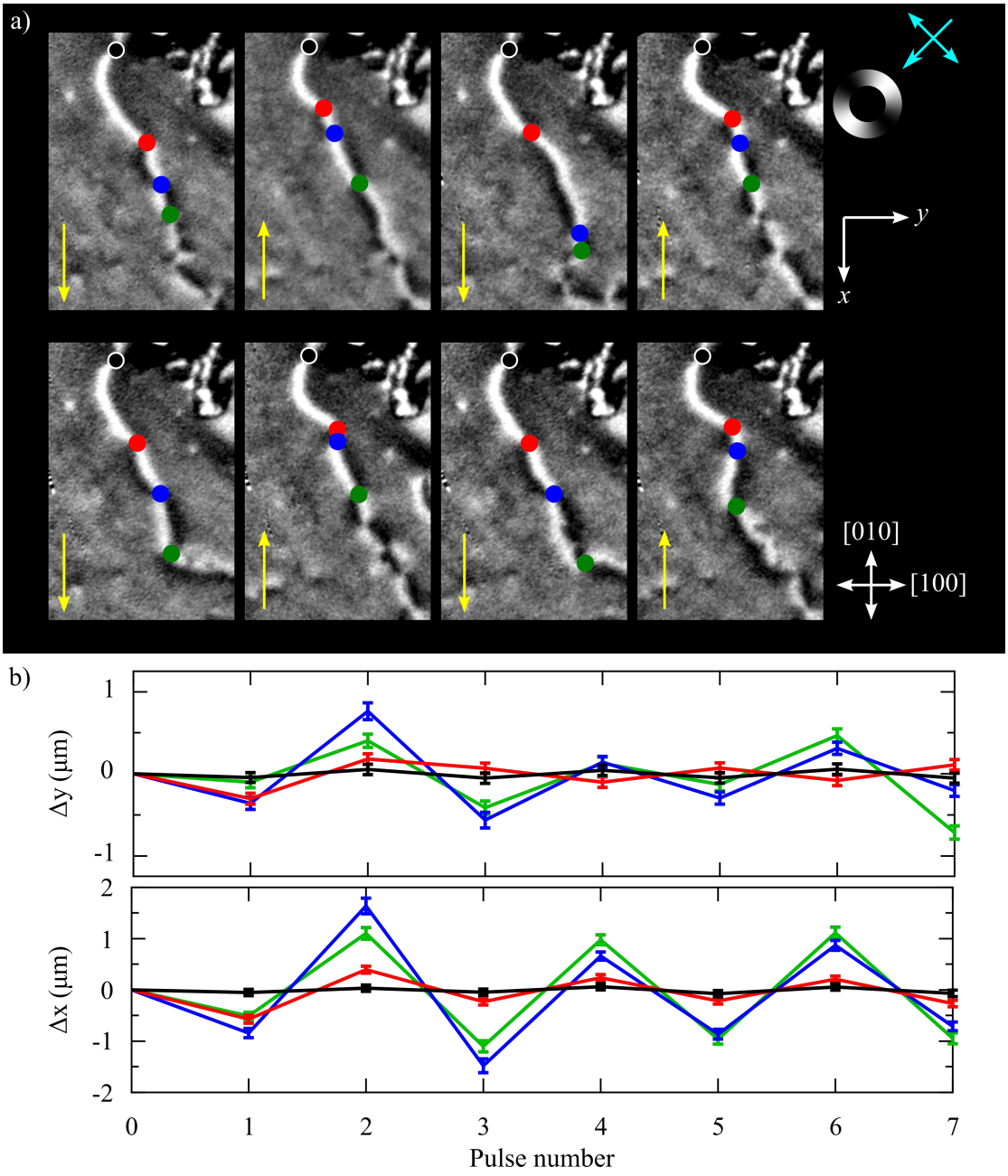

Figure 6.7: *a) Expanded view of the* 180° *AFDW with electrically generated AF vortices seen moving during a sequence of* 1 ms, 21 V *pulses applied along the vertical direction (yellow arrows). The centroid locations (coloured circles) of the first four vortices were tracked during the pulsing sequence. b) shows plots of the change in* x *and* y *coordinates,* Δx *and* Δy*, of the vortex centroids with plot colour corresponding to coloured circles in a).*

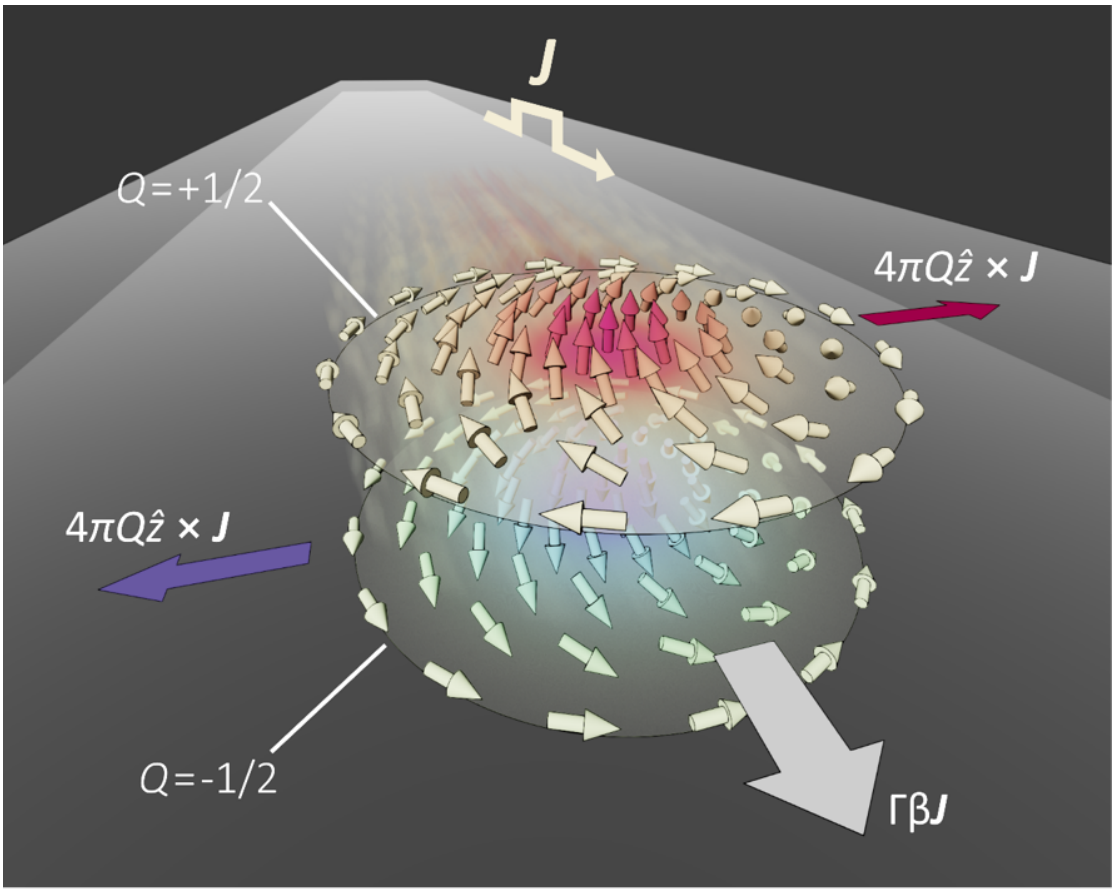

Figure 6.8: *AF meron driven by an electrical current pulse. On the individual magnetic sublattices, the half-integer topological charge, Q, generates gyrotropic forces (red and blue arrows), that compensate each other. The remaining drag force, $\Gamma\beta\mathbf{J}$, propels the AF meron in the direction of the current.*

sublattice are given by $G\hat{z} \times \boldsymbol{J}$, where $G = 4\pi Q^{(k)}$ is the gyrocoupling constant depending on the sublattice topological charge, $Q^{(k)}$. Since the AF vortex has opposite topological charges for each sublattice, the gyrotropic forces compensate each other as shown schematically in Fig. 6.8. This results in a remaining generalized drag force, $F = \Gamma\beta\boldsymbol{J}$, where β is the sum of the current-induced torques acting on the AF vortex [222]. The vortex is propelled by this force at terminal velocity $v_{\parallel} = \beta\boldsymbol{J}$, parallel to the current direction.

The generation and movement of AF vortices shown in Figures 6.5 and 6.7 can be explained based on energetics and the generalized Thiele equation for AF vortex dynamics. The underlying physics corresponds to the nucleation of vortex-antivortex pairs and the consecutive motion of these AF vortices due to applied electrical pulse. For nucleation to occur, the length of the pulse must be long enough to supply the energy above a threshold energy needed to nucleate a vortex-antivortex pair, in short enough time, so that this energy is not dissipated during this time due to damping in the system. In the exchange dominated limit, the critical energy for nucleation is given by a topological invariant $8\pi QAt$, where Q is the topological charge of vortex/antivortex, A is the AF exchange constant and t is the thickness of the sample [181, 222]. In our system a higher critical energy is expected as it involves all other interactions present. We note that the energy is minimized for vortex-antivortex pairs localized on the 180° AFDW.

After the vortex-antivortex pair is created, for the consecutive AF vortex motion it is important that in AFs both vortex and antivortex move along the current, in this particular case along the AF domain walls in the direction of the current, as this again corresponds to the minimized energy state. Deflection free movement is attributed to the fact that in AFs gyrotropic (Magnus) forces completely cancel out across the two AF sublattices [222]. The resulting force in Thiele's equation (Equation 6.5) is always in the current direction and is independent of the topological charge of AF vortex, i.e., it is the same for both vortex and antivortex. Any type of spin torque, including NSOT due to the CuMnAs crystal symmetry as well as spin transfer torques due to the gradient in $\boldsymbol{L}$, will contribute to the force. The pinning sites, due to defects and local differences in anisotropy, play an important role in determining the positions between which the vortices move, as shown in Figure 6.7.

Overall, it has been demonstrated that topological AF vortices (Bloch- and Néel-type

merons, antimerons, and bimerons) are stabilized at room temperature in thin film AF material, CuMnAs. Vortex-antivortex pairs can be generated, localized on 180° AFDWs, using microsecond electrical pulses. Once stabilized, a sequence of alternating polarity pulses causes the vortices and antivortices to move reversibly in the pulse direction, congruent with the vortex dynamics predicted by the generalized Thiele equation. This demonstration represents a crucial step towards realizing the full potential of AF thin films as active components in ultrafast magnetic soliton-based memory devices.

Chapter 7

Conclusion and Outlook

CuMnAs has been key to the development of antiferromagnetic (AF) spintronics over recent years. The crystal symmetry of the tetragonal phase gives rise to 'hidden' Rashba effects; although globally compensated, a flowing current locally spin polarizes, generating opposite sign effective fields on the magnetic sublattices [12]. This induces equal spin-orbit torques on the Mn magnetic moments, efficiently rotating the Néel vector perpendicular to the current direction. By applying orthogonal current pulses, the AF order can be switched between two perpendicular states and detected electrically in the anisotropic magnetoresistance [13, 93, 94, 107, 108]. This forms the basis of a magnetic memory with an AF material as the primary component.

In this thesis, current-induced phenomena were explored in the transport properties and AF domain structure of tetragonal CuMnAs thin films. Chapter 4 looked at characterizing the temperature, CuMnAs layer thickness, and substrate material dependence of a high magnetoresistive switching signal that is onset above a current density threshold. It was shown that the signal relaxes over time and the multicomponent exponential function describing the relaxation followed Néel-Arrhenius behaviour. From a careful temperature dependent study it was possible to extract a material dependent attempt rate, which fell in the terahertz range - intrinsic to AF spin dynamics. The resistive signal and signal relaxation are attributed to the nano-fragmentation and reformation of the AF domain structure [112, 126, 127]. However, a conclusive link between the electrical transport measurements and magnetic imaging needs to be established. In particular, no conclusions have been made about the origin of the multiple decay components which can have opposite sign, although ubiquitous in complex relaxing systems.

A more thorough investigation, using better resolution time-resolved magnetic imaging combined with electrical measurements, is required to confirm the magnetic origin of the relaxing resistive signal.

Presented in Chapter 5 and Chapter 6, synchrotron based magnetic imaging technique, XMLD-PEEM, was used to directly image current-induced changes to the AF domain structure of CuMnAs devices. At relatively low pulse current densities ($\leq$1 A cm^{-2}), 180° domain walls are observed to move in a reversible and repeatable manner, dependent on the direction of the current (Chapter 5). At higher pulse current densities ($\geq$1.2 A cm^{-2}) the generation of AF vortices and antivortices nucleated at points of chirality reversal on 180° domain walls was observed (Chapter 6). A sequence of electrical pulses with alternating polarity was able to reversibly move the vortex-antivortex pairs, in the pulse direction, between pinning sites. Both AF textures have significant proposed implications for racetrack-type architectures, which are anticipated to vastly improve the speed and density of magnetic memory devices. Whilst the work presented here is a step towards realizing practical devices based on AF textures, a reliable way to control the AF domain morphologies is required to consistently reproduce these results. It has also been shown that pinning of AF textures by local defects is important in determining the positions to which they can move. Work has been done to thoroughly characterize the effects of microtwin structural defects, but their tailored growth has not been achieved [43].

Bibliography

[1] J.-G. Zhu, "Magnetoresistive random access memory: The path to competitiveness and scalability," *Proceedings of the IEEE*, vol. 96, no. 11, pp. 1786–1798, 2008.

[2] R. B. Goldfarb, B. Dieny, and K.-J. Lee, *Introduction to magnetic random-access memory*. John Wiley & Sons, 2016.

[3] S. Bhatti, R. Sbiaa, A. Hirohata, H. Ohno, S. Fukami, and S. Piramanayagam, "Spintronics based random access memory: a review," *Materials Today*, vol. 20, no. 9, pp. 530–548, 2017.

[4] S. Ikegawa, F. B. Mancoff, J. Janesky, and S. Aggarwal, "Magnetoresistive random access memory: Present and future," *IEEE Transactions on Electron Devices*, vol. 67, no. 4, pp. 1407–1419, 2020.

[5] S. Tehrani, J. M. Slaughter, M. Deherrera, B. N. Engel, N. D. Rizzo, J. Salter, M. Durlam, R. W. Dave, J. Janesky, B. Butcher *et al.*, "Magnetoresistive random access memory using magnetic tunnel junctions," *Proceedings of the IEEE*, vol. 91, no. 5, pp. 703–714, 2003.

[6] A. Manchon, H. C. Koo, J. Nitta, S. Frolov, and R. Duine, "New perspectives for rashba spin–orbit coupling," *Nature materials*, vol. 14, no. 9, pp. 871–882, 2015.

[7] A. Manchon, J. Železnỳ, I. M. Miron, T. Jungwirth, J. Sinova, A. Thiaville, K. Garello, and P. Gambardella, "Current-induced spin-orbit torques in ferromagnetic and antiferromagnetic systems," *Reviews of Modern Physics*, vol. 91, no. 3, p. 035004, 2019.

[8] T. Jungwirth, X. Marti, P. Wadley, and J. Wunderlich, "Antiferromagnetic spintronics," *Nature nanotechnology*, vol. 11, no. 3, pp. 231–241, 2016.

[9] O. Gomonay, T. Jungwirth, and J. Sinova, "Concepts of antiferromagnetic spintronics," *physica status solidi (RRL)–Rapid Research Letters*, vol. 11, no. 4, p. 1700022, 2017.

[10] J. Železnỳ, P. Wadley, K. Olejník, A. Hoffmann, and H. Ohno, "Spin transport and spin torque in antiferromagnetic devices," *Nature Physics*, vol. 14, no. 3, pp. 220–228, 2018.

[11] E. Gomonay and V. Loktev, "Spintronics of antiferromagnetic systems," *Low Temperature Physics*, vol. 40, no. 1, pp. 17–35, 2014.

[12] J. Železnỳ, H. Gao, K. Vỳbornỳ, J. Zemen, J. Mašek, A. Manchon, J. Wunderlich, J. Sinova, and T. Jungwirth, "Relativistic néel-order fields induced by electrical current in antiferromagnets," *Physical review letters*, vol. 113, no. 15, p. 157201, 2014.

[13] P. Wadley, B. Howells, J. Železnỳ, C. Andrews, V. Hills, R. P. Campion, V. Novák, K. Olejník, F. Maccherozzi, S. Dhesi *et al.*, "Electrical switching of an antiferromagnet," *Science*, vol. 351, no. 6273, pp. 587–590, 2016.

[14] F. Máca, J. Mašek, O. Stelmakhovych, X. Martí, H. Reichlová, K. Uhlířová, P. Beran, P. Wadley, V. Novák, and T. Jungwirth, "Room-temperature antiferromagnetism in cumnas," *Journal of magnetism and magnetic materials*, vol. 324, no. 8, pp. 1606–1612, 2012.

[15] P. Wadley, V. Novák, R. Campion, C. Rinaldi, X. Martí, H. Reichlová, J. Železnỳ, J. Gazquez, M. Roldan, M. Varela *et al.*, "Tetragonal phase of epitaxial room-temperature antiferromagnet CuMnAs," *Nature Communications*, vol. 4, no. 1, pp. 1–6, 2013.

[16] K. Uhlířová, R. Tarasenko, F. J. Martínez-Casado, B. Vondráčková, and Z. Matěj, "Synthesis and single crystal study of cumn3as2 and cu2mn4as3," *Journal of Alloys and Compounds*, vol. 650, pp. 224–227, 2015.

[17] P. Wadley, V. Hills, M. Shahedkhah, K. Edmonds, R. Campion, V. Novák, B. Ouladdiaf, D. Khalyavin, S. Langridge, V. Saidl *et al.*, "Antiferromagnetic structure in tetragonal cumnas thin films," *Scientific reports*, vol. 5, no. 1, pp. 1–6, 2015.

[18] F. Máca, J. Kudrnovskỳ, V. Drchal, K. Carva, P. Baláž, and I. Turek, "Physical properties of the tetragonal CuMnAs: A first-principles study," *Physical Review B*, vol. 96, no. 9, p. 094406, 2017.

[19] S. Blundell, *Magnetism in Condensed Matter*, ser. Oxford Master Series in Condensed Matter Physics 4. OUP Oxford, 2001.

[20] V. Hills, P. Wadley, R. P. Campion, V. Novak, R. Beardsley, K. W. Edmonds, B. L. Gallagher, B. Ouladdiaf, and T. Jungwirth, "Paramagnetic to antiferromagnetic transition in epitaxial tetragonal cumnas (invited)," *Journal of Applied Physics*, vol. 117, no. 17, p. 172608, 2015.

[21] K. Uhlířová, E. Duverger-Nédellec, R. H. Colman, J. Volnỳ, B. Vondráčková, and K. Carva, "The stability and physical properties of the tetragonal phase of bulk cumnas antiferromagnet," *Journal of Alloys and Compounds*, vol. 771, pp. 680–685, 2019.

[22] M. H. Karigerasi, K. Kang, A. Ramanathan, D. L. Gray, M. D. Frontzek, H. Cao, A. Schleife, and D. P. Shoemaker, "In-plane hexagonal antiferromagnet in the cumn-as system cu 0.82 mn 1.18 as," *Physical Review Materials*, vol. 3, no. 11, p. 111402, 2019.

[23] I. A. Zhuravlev, A. Adhikari, and K. Belashchenko, "Perpendicular magnetic anisotropy in bulk and thin-film cumnas for antiferromagnetic memory applications," *Applied Physics Letters*, vol. 113, no. 16, p. 162404, 2018.

[24] M. Veis, J. Minár, G. Steciuk, L. Palatinus, C. Rinaldi, M. Cantoni, D. Kriegner, K. Tikuišis, J. Hamrle, M. Zahradník *et al.*, "Band structure of cumnas probed by optical and photoemission spectroscopy," *Physical Review B*, vol. 97, no. 12, p. 125109, 2018.

[25] C. Kittel, P. McEuen, and P. McEuen, *Introduction to solid state physics*. Wiley New York, 1996, vol. 8.

[26] L. Šmejkal, J. Železnỳ, J. Sinova, and T. Jungwirth, "Electric control of dirac quasiparticles by spin-orbit torque in an antiferromagnet," *Physical review letters*, vol. 118, no. 10, p. 106402, 2017.

[27] L. Šmejkal, T. Jungwirth, and J. Sinova, "Route towards dirac and weyl antiferromagnetic spintronics," *physica status solidi (RRL)–Rapid Research Letters*, vol. 11, no. 4, p. 1700044, 2017.

[28] P. Tang, Q. Zhou, G. Xu, and S.-C. Zhang, "Dirac fermions in an antiferromagnetic semimetal," *Nature Physics*, vol. 12, no. 12, pp. 1100–1104, 2016.

[29] T. Dietl, D. D. Awschalom, M. Kaminska, and H. Ohno, *Spintronics*. Academic Press, 2009.

[30] D. H. D. H. Martin, *Magnetism in solids / D.H. Martin.* London: Iliffe, 1967.

[31] B. D. Cullity and C. D. Graham, *Introduction to magnetic materials*. John Wiley & Sons, 2011.

[32] D. J. Craik and R. S. Tebble, *Ferromagnetism and ferromagnetic domains*. North-Holland Publishing Company, 1965, vol. 4.

[33] P. Bruno, "Tight-binding approach to the orbital magnetic moment and magnetocrystalline anisotropy of transition-metal monolayers," *Physical Review B*, vol. 39, no. 1, p. 865, 1989.

[34] G. van der Laan, "Microscopic origin of magnetocrystalline anisotropy in transition metal thin films," *Journal of Physics: Condensed Matter*, vol. 10, no. 14, p. 3239, 1998.

[35] R. Wu and A. J. Freeman, "Spin–orbit induced magnetic phenomena in bulk metals and their surfaces and interfaces," *Journal of Magnetism and Magnetic Materials*, vol. 200, no. 1-3, pp. 498–514, 1999.

[36] T. Seki, T. Shima, K. Takanashi, Y. Takahashi, E. Matsubara, and K. Hono, "L1 0 ordering of off-stoichiometric fept (001) thin films at reduced temperature," *Applied physics letters*, vol. 82, no. 15, pp. 2461–2463, 2003.

[37] T. Ono, N. Kikuchi, S. Okamoto, O. Kitakami, and T. Shimatsu, "Novel torque magnetometry for uniaxial anisotropy constants of thin films and its application to fept granular thin films," *Applied Physics Express*, vol. 11, no. 3, p. 033002, 2018.

[38] S. Komogortsev, N. Chizhik, E. Y. Filatov, S. Korenev, Y. Shubin, D. Velikanov, R. S. Iskhakov, and G. Y. Yurkin, "Magnetic properties and l10 phase formation in copt nanoparticles," in *Solid State Phenomena*, vol. 190. Trans Tech Publ, 2012, pp. 159–162.

[39] X. Han, Q. Liu, J. Wang, S. Li, Y. Ren, R. Liu, and F. Li, "Influence of crystal orientation on magnetic properties of hcp co nanowire arrays," *Journal of Physics D: Applied Physics*, vol. 42, no. 9, p. 095005, apr 2009.

[40] F. Virot, L. Favre, R. Hayn, and M. D. Kuz'min, "Theory of magnetic domains in uniaxial thin films," *Journal of Physics D: Applied Physics*, vol. 45, no. 40, p. 405003, sep 2012.

[41] H. Gomonay, "Magnetoelastic mechanism of long-range magnetic ordering in magnetic/nonmagnetic multilayers," *Physical Review B*, vol. 64, no. 5, p. 054404, 2001.

[42] H. Gomonay and V. M. Loktev, "Magnetostriction and magnetoelastic domains in antiferromagnets," *Journal of Physics: Condensed Matter*, vol. 14, no. 15, p. 3959, 2002.

[43] S. Reimers, D. Kriegner, O. Gomonay, D. Carbone, F. Krizek, V. Novak, R. P. Campion, F. Maccherozzi, A. Bjorling, O. J. Amin *et al.*, "Defect-driven antiferromagnetic domain walls in cumnas films," *arXiv preprint arXiv:2110.03724*, 2021.

[44] F. Keffer and C. Kittel, "Theory of antiferromagnetic resonance," *Physical Review*, vol. 85, no. 2, p. 329, 1952.

[45] R. B. Goldfarb, B. Dieny, and K.-J. Lee, *Introduction to magnetic random-access memory*. John Wiley & Sons, 2016.

[46] K. M. D. Hals, Y. Tserkovnyak, and A. Brataas, "Phenomenology of current-induced dynamics in antiferromagnets," *Phys. Rev. Lett.*, vol. 106, p. 107206, Mar 2011. [Online]. Available: https://link.aps.org/doi/10.1103/PhysRevLett.106.107206

[47] P. Li, J. Chen, R. Du, and X.-P. Wang, "Numerical methods for antiferromagnets," *IEEE Transactions on Magnetics*, vol. 56, no. 4, pp. 1–9, 2020.

[48] J. Shi, V. Lopez-Dominguez, F. Garesci, C. Wang, H. Almasi, M. Grayson, G. Finocchio, and P. Khalili Amiri, "Electrical manipulation of the magnetic order in antiferromagnetic ptmn pillars," *Nature Electronics*, vol. 3, no. 2, pp. 92–98, 2020.

[49] O. Gomonay, V. Baltz, A. Brataas, and Y. Tserkovnyak, "Antiferromagnetic spin textures and dynamics," *Nature Physics*, vol. 14, no. 3, pp. 213–216, 2018.

[50] H. Yuan, Z. Yuan, R. A. Duine, and X. Wang, "Recent progress in antiferromagnetic dynamics," *Europhysics Letters*, vol. 132, no. 5, p. 57001, 2021.

[51] L. Sánchez-Tejerina, V. Puliafito, P. K. Amiri, M. Carpentieri, and G. Finocchio, "Dynamics of domain-wall motion driven by spin-orbit torque in antiferromagnets," *Physical Review B*, vol. 101, no. 1, p. 014433, 2020.

[52] R. Winkler, S. Papadakis, E. De Poortere, and M. Shayegan, *Spin-Orbit Coupling in Two-Dimensional Electron and Hole Systems*. Springer, 2003, vol. 41.

[53] T. Shinjo, *Nanomagnetism and spintronics*. Elsevier, 2013.

[54] E. I. Rashba, "Properties of semiconductors with an extremum loop. i. cyclotron and combinational resonance in a magnetic field perpendicular to the plane of the loop," *Soviet Physics, Solid State*, vol. 2, pp. 1109–1122, 1960.

[55] F. Vas' ko, "Spin splitting in the spectrum of two-dimensional electrons due to the surface potential," *Soviet Journal of Experimental and Theoretical Physics Letters*, vol. 30, p. 541, 1979.

[56] Y. A. Bychkov, "Properties of 2d electron gas with lifted spectral degeneracy," *JETP lett.*, vol. 39, no. 2, pp. 78–81, 1984.

[57] G. Dresselhaus, "Spin-orbit coupling effects in zinc blende structures," *Physical Review*, vol. 100, no. 2, p. 580, 1955.

[58] R. J. Tilley, *Crystals and crystal structures*. John Wiley & Sons, 2020.

[59] X. Zhang, Q. Liu, J.-W. Luo, A. J. Freeman, and A. Zunger, "Hidden spin polarization in inversion-symmetric bulk crystals," *Nature Physics*, vol. 10, no. 5, pp. 387–393, 2014.

[60] S. D. Ganichev, E. Ivchenko, V. Bel'Kov, S. Tarasenko, M. Sollinger, D. Weiss, W. Wegscheider, and W. Prettl, "Spin-galvanic effect," *Nature*, vol. 417, no. 6885, pp. 153–156, 2002.

[61] S. Sangiao, J. De Teresa, L. Morellon, I. Lucas, M. C. Martínez-Velarte, and M. Viret, "Control of the spin to charge conversion using the inverse rashba-edelstein effect," *Applied Physics Letters*, vol. 106, no. 17, p. 172403, 2015.

[62] S. Y. Bodnar, L. Šmejkal, I. Turek, T. Jungwirth, O. Gomonay, J. Sinova, A. Sapozhnik, H.-J. Elmers, M. Kläui, and M. Jourdan, "Writing and reading antiferromagnetic mn 2 au by néel spin-orbit torques and large anisotropic magnetoresistance," *Nature communications*, vol. 9, no. 1, pp. 1–7, 2018.

[63] T. McGuire and R. Potter, "Anisotropic magnetoresistance in ferromagnetic 3d alloys," *IEEE Transactions on Magnetics*, vol. 11, no. 4, pp. 1018–1038, 1975.

[64] A. P. Malozemoff, "Anisotropic magnetoresistance with cubic anisotropy and weak ferromagnetism: A new paradigm," *Physical Review B*, vol. 34, no. 3, p. 1853, 1986.

[65] A. Rushforth, K. Vỳbornỳ, C. King, K. Edmonds, R. Campion, C. Foxon, J. Wunderlich, A. Irvine, P. Vašek, V. Novák *et al.*, "Anisotropic magnetoresistance components in (ga, mn) as," *Physical review letters*, vol. 99, no. 14, p. 147207, 2007.

[66] J. Stöhr, H. Padmore, S. Anders, T. Stammler, and M. Scheinfein, "Principles of x-ray magnetic dichroism spectromicroscopy," *Surface review and letters*, vol. 5, no. 06, pp. 1297–1308, 1998.

[67] J. Stöhr, Y. Wu, B. Hermsmeier, M. Samant, G. Harp, S. Koranda, D. Dunham, and B. Tonner, "Element-specific magnetic microscopy with circularly polarized x-rays," *Science*, vol. 259, no. 5095, pp. 658–661, 1993.

[68] C. Vettier, "Resonant x-ray scattering from magnetic materials," *Journal of magnetism and magnetic materials*, vol. 129, no. 1, pp. 59–65, 1994.

[69] J. E. Penner-Hahn *et al.*, "X-ray absorption spectroscopy," *Comprehensive Coordination Chemistry II*, vol. 2, pp. 159–186, 2003.

[70] P. Fischer, "Exploring nanoscale magnetism in advanced materials with polarized x-rays," *Materials Science and Engineering: R: Reports*, vol. 72, no. 5, pp. 81–95, 2011.

[71] G. van der Laan and A. I. Figueroa, "X-ray magnetic circular dichroism—a versatile tool to study magnetism," *Coordination Chemistry Reviews*, vol. 277, pp. 95–129, 2014.

[72] A. Scholl, J. Stöhr, J. Lüning, J. W. Seo, J. Fompeyrine, H. Siegwart, J.-P. Locquet, F. Nolting, S. Anders, E. Fullerton *et al.*, "Observation of antiferromagnetic domains in epitaxial thin films," *Science*, vol. 287, no. 5455, pp. 1014–1016, 2000.

[73] A. Scholl, "Applications of photoemission electron microscopy (peem) in magnetism research," *Current Opinion in Solid State and Materials Science*, vol. 7, no. 1, pp. 59–66, 2003.

[74] X. Cheng and D. Keavney, "Studies of nanomagnetism using synchrotron-based x-ray photoemission electron microscopy (x-peem)," *Reports on Progress in Physics*, vol. 75, no. 2, p. 026501, 2012.

[75] J. Stohr and R. Nakajima, "Magnetic properties of transition-metal multilayers studied with x-ray magnetic circular dichroism spectroscopy," *IBM Journal of Research and Development*, vol. 42, no. 1, pp. 73–88, 1998.

[76] R. Nakajima, J. Stöhr, and Y. U. Idzerda, "Electron-yield saturation effects in l-edge x-ray magnetic circular dichroism spectra of fe, co, and ni," *Physical Review B*, vol. 59, no. 9, p. 6421, 1999.

[77] C. M. Schneider and G. Schönhense, "Investigating surface magnetism by means of photoexcitation electron emission microscopy," *Reports on Progress in Physics*, vol. 65, no. 12, p. 1785, 2002.

[78] E. Bauer, "A brief history of peem," *Journal of Electron Spectroscopy and Related Phenomena*, vol. 185, no. 10, pp. 314–322, 2012.

[79] G. Marx, V. Gerheim, and G. Schönhense, "Multipole wien-filter for a high-resolution x-peem," *Journal of electron spectroscopy and related phenomena*, vol. 84, no. 1-3, pp. 251–261, 1997.

[80] R. Tromp, J. Hannon, A. Ellis, W. Wan, A. Berghaus, and O. Schaff, "A new aberration-corrected, energy-filtered leem/peem instrument. i. principles and design," *Ultramicroscopy*, vol. 110, no. 7, pp. 852–861, 2010.

[81] A. Scholl, M. Marcus, A. Doran, J. Nasiatka, A. Young, A. MacDowell, R. Streubel, N. Kent, J. Feng, W. Wan *et al.*, "Hartmann characterization of the peem-3 aberration-corrected x-ray photoemission electron microscope," *Ultramicroscopy*, vol. 188, pp. 77–84, 2018.

[82] O. Gomonay, T. Jungwirth, and J. Sinova, "High antiferromagnetic domain wall velocity induced by Néel spin-orbit torques," *Phys. Rev. Lett.*, vol. 117, p. 017202, 2016.

[83] P. E. Roy, R. M. Otxoa, and J. Wunderlich, "Robust picosecond writing of a layered antiferromagnet by staggered spin-orbit fields," *Phys. Rev. B*, vol. 94, p. 014439, 2016.

[84] L. Šmejkal, Y. Mokrousov, B. Yan, and A. H. MacDonald, "Topological antiferromagnetic spintronics," *Nature Physics*, vol. 14, no. 3, p. 242, 2018.

[85] V. M. Edelstein, "Spin polarization of conduction electrons induced by electric current in two-dimensional asymmetric electron systems," *Solid State Communications*, vol. 73, no. 3, pp. 233–235, 1990.

[86] A. Chernyshov, M. Overby, X. Liu, J. K. Furdyna, Y. Lyanda-Geller, and L. P. Rokhinson, "Evidence for reversible control of magnetization in a ferromagnetic material by means of spin–orbit magnetic field," *Nature Physics*, vol. 5, no. 9, pp. 656–659, 2009.

[87] C. Ciccarelli, L. Anderson, V. Tshitoyan, A. Ferguson, F. Gerhard, C. Gould, L. Molenkamp, J. Gayles, J. Železnỳ, L. Šmejkal *et al.*, "Room-temperature spin–orbit torque in NiMnSb," *Nature Physics*, vol. 12, no. 9, pp. 855–860, 2016.

[88] V. Barthem, C. Colin, H. Mayaffre, M.-H. Julien, and D. Givord, "Revealing the properties of Mn_2Au for antiferromagnetic spintronics," *Nature Communications*, vol. 4, no. 1, pp. 1–7, 2013.

[89] L. Liu, T. Moriyama, D. C. Ralph, and R. A. Buhrman, "Spin-torque ferromagnetic resonance induced by the spin hall effect," *Phys. Rev. Lett.*, vol. 106, no. 3, p. 036601, 2011.

[90] H. V. Gomonay and V. M. Loktev, "Spin transfer and current-induced switching in antiferromagnets," *Physical Review B*, vol. 81, no. 14, p. 144427, 2010.

[91] R. Cheng, J. Xiao, Q. Niu, and A. Brataas, "Spin pumping and spin-transfer torques in antiferromagnets," *Physical Review Letters*, vol. 113, no. 5, p. 057601, 2014.

[92] X. Chen, R. Zarzuela, J. Zhang, C. Song, X. Zhou, G. Shi, F. Li, H. Zhou, W. Jiang, F. Pan *et al.*, "Antidamping-torque-induced switching in biaxial antiferromagnetic insulators," *Physical review letters*, vol. 120, no. 20, p. 207204, 2018.

[93] K. Olejník, V. Schuler, X. Martí, V. Novák, Z. Kašpar, P. Wadley, R. P. Campion, K. W. Edmonds, B. L. Gallagher, J. Garcés *et al.*, "Antiferromagnetic cumnas multi-level memory cell with microelectronic compatibility," *Nature communications*, vol. 8, no. 1, pp. 1–7, 2017.

[94] K. Olejník, T. Seifert, Z. Kašpar, V. Novák, P. Wadley, R. P. Campion, M. Baumgartner, P. Gambardella, P. Němec, J. Wunderlich *et al.*, "Terahertz electrical writing speed in an antiferromagnetic memory," *Science advances*, vol. 4, no. 3, p. eaar3566, 2018.

[95] X. Zhou, J. Zhang, F. Li, X. Chen, G. Shi, Y. Tan, Y. Gu, M. Saleem, H. Wu, F. Pan *et al.*, "Strong orientation-dependent spin-orbit torque in thin films of the antiferromagnet mn 2 au," *Physical Review Applied*, vol. 9, no. 5, p. 054028, 2018.

[96] M. Meinert, D. Graulich, and T. Matalla-Wagner, "Electrical switching of antiferromagnetic Mn_2Au and the role of thermal activation," *Physical Review Applied*, vol. 9, no. 6, p. 064040, 2018.

[97] T. Moriyama, K. Oda, T. Ohkochi, M. Kimata, and T. Ono, "Spin torque control of antiferromagnetic moments in nio," *Scientific reports*, vol. 8, no. 1, pp. 1–6, 2018.

[98] P. Zhang, J. Finley, T. Safi, and L. Liu, "Quantitative study on current-induced effect in an antiferromagnet insulator/pt bilayer film," *Physical Review Letters*, vol. 123, no. 24, p. 247206, 2019.

[99] L. Baldrati, O. Gomonay, A. Ross, M. Filianina, R. Lebrun, R. Ramos, C. Leveille, F. Fuhrmann, T. Forrest, F. Maccherozzi *et al.*, "Mechanism of néel order switching in antiferromagnetic thin films revealed by magnetotransport and direct imaging," *Physical review letters*, vol. 123, no. 17, p. 177201, 2019.

[100] Y. Cheng, S. Yu, M. Zhu, J. Hwang, and F. Yang, "Electrical switching of tristate antiferromagnetic néel order in α- fe 2 o 3 epitaxial films," *Physical Review Letters*, vol. 124, no. 2, p. 027202, 2020.

[101] A. Kurenkov, S. DuttaGupta, C. Zhang, S. Fukami, Y. Horio, and H. Ohno, "Artificial neuron and synapse realized in an antiferromagnet/ferromagnet heterostructure using dynamics of spin–orbit torque switching," *Advanced Materials*, vol. 31, no. 23, p. 1900636, 2019.

[102] T. Matalla-Wagner, J.-M. Schmalhorst, G. Reiss, N. Tamura, and M. Meinert, "Resistive contribution in electrical switching experiments with antiferromagnets," *arXiv preprint arXiv:1910.08576*, 2019.

[103] C. Chiang, S. Huang, D. Qu, P. Wu, and C. Chien, "Absence of evidence of electrical switching of the antiferromagnetic Néel vector," *Physical Review Letters*, vol. 123, no. 22, p. 227203, 2019.

[104] J. R. Black, "Electromigration—a brief survey and some recent results," *IEEE Transactions on Electron Devices*, vol. 16, no. 4, pp. 338–347, 1969.

[105] N. L. Nair, E. Maniv, C. John, S. Doyle, J. Orenstein, and J. G. Analytis, "Electrical switching in a magnetically intercalated transition metal dichalcogenide," *Nature Materials*, vol. 19, no. 2, pp. 153–157, 2020.

[106] X. Chen, X. Zhou, R. Cheng, C. Song, J. Zhang, Y. Wu, Y. Ba, H. Li, Y. Sun, Y. You *et al.*, "Electric field control of Néel spin–orbit torque in an antiferromagnet," *Nature materials*, vol. 18, no. 9, pp. 931–935, 2019.

[107] M. Grzybowski, P. Wadley, K. Edmonds, R. Beardsley, V. Hills, R. Campion, B. Gallagher, J. S. Chauhan, V. Novak, T. Jungwirth *et al.*, "Imaging current-induced switching of antiferromagnetic domains in CuMnAs," *Physical Review Letters*, vol. 118, no. 5, p. 057701, 2017.

[108] P. Wadley, S. Reimers, M. J. Grzybowski, C. Andrews, M. Wang, J. S. Chauhan, B. L. Gallagher, R. P. Campion, K. W. Edmonds, S. S. Dhesi *et al.*, "Current polarity-dependent manipulation of antiferromagnetic domains," *Nature nanotechnology*, vol. 13, no. 5, pp. 362–365, 2018.

[109] S. Y. Bodnar, M. Filianina, S. Bommanaboyena, T. Forrest, F. Maccherozzi, A. Sapozhnik, Y. Skourski, M. Kläui, and M. Jourdan, "Imaging of current induced néel vector switching in antiferromagnetic mn 2 au," *Physical Review B*, vol. 99, no. 14, p. 140409, 2019.

[110] H. Reichlova, T. Janda, J. Godinho, A. Markou, D. Kriegner, R. Schlitz, J. Zelezny, Z. Soban, M. Bejarano, H. Schultheiss *et al.*, "Imaging and writing magnetic domains in the non-collinear antiferromagnet Mn_3Sn," *Nature Communications*, vol. 10, no. 1, pp. 1–6, 2019.

[111] I. Gray, T. Moriyama, N. Sivadas, G. M. Stiehl, J. T. Heron, R. Need, B. J. Kirby, D. H. Low, K. C. Nowack, D. G. Schlom *et al.*, "Spin seebeck imaging of spin-torque switching in antiferromagnetic Pt/NiO heterostructures," *Physical Review X*, vol. 9, no. 4, p. 041016, 2019.

[112] M. Wörnle, P. Welter, Z. Kašpar, K. Olejník, V. Novák, R. Campion, P. Wadley, T. Jungwirth, C. Degen, and P. Gambardella, "Current-induced fragmentation of antiferromagnetic domains," *arXiv preprint arXiv:1912.05287*, 2019.

[113] Z. Kašpar, M. Surýnek, J. Zubáč, F. Krizek, V. Novák, R. P. Campion, M. S. Wörnle, P. Gambardella, X. Marti, P. Němec, K. W. Edmonds, S. Reimers, O. J. Amin, F. Maccherozzi, S. S. Dhesi, P. Wadley, J. Wunderlich, K. Olejník, and

T. Jungwirth, "High electrical and optical resistive switching in a thin-film antiferromagnet," 2019.

[114] M. Wang, C. Andrews, S. Reimers, O. Amin, P. Wadley, R. Campion, S. Poole, J. Felton, K. Edmonds, B. Gallagher *et al.*, "Spin flop and crystalline anisotropic magnetoresistance in CuMnAs," *Phys. Rev. B*, vol. 101, p. 094429, 2020.

[115] J. Xu, C. Zhou, M. Jia, D. Shi, C. Liu, H. Chen, G. Chen, G. Zhang, Y. Liang, J. Li *et al.*, "Imaging antiferromagnetic domains in nickel oxide thin films by optical birefringence effect," *Physical Review B*, vol. 100, no. 13, p. 134413, 2019.

[116] J. Xu, H. Chen, C. Zhou, D. Shi, G. Chen, and Y. Wu, "Optical imaging of antiferromagnetic domains in ultrathin coo (001) films," *arXiv preprint arXiv:2003.12768*, 2020.

[117] F. Schreiber, L. Baldrati, C. Schmitt, R. Ramos, E. Saitoh, R. Lebrun, and M. Kläui, "Concurrent magneto-optical imaging and magneto-transport readout of electrical switching of insulating antiferromagnetic thin films," *arXiv preprint arXiv:2004.13374*, 2020.

[118] R. Cheng, D. Xiao, and A. Brataas, "Terahertz antiferromagnetic spin hall nano-oscillator," *Physical Review Letters*, vol. 116, no. 20, p. 207603, 2016.

[119] O. Gomonay, T. Jungwirth, and J. Sinova, "Narrow-band tunable terahertz detector in antiferromagnets via staggered-field and antidamping torques," *Physical Review B*, vol. 98, no. 10, p. 104430, 2018.

[120] P. Dowben, D. Nikonov, A. Marshall, and C. Binek, "Magneto-electric antiferromagnetic spin–orbit logic devices," *Applied Physics Letters*, vol. 116, no. 8, p. 080502, 2020.

[121] A. Ross, R. Lebrun, O. Gomonay, D. Grave, A. Kay, L. Baldrati, S. Becker, A. Qaiumzadeh, C. Ulloa, G. Jakob *et al.*, "Propagation length of antiferromagnetic magnons governed by domain configurations." *Nano Letters*, vol. 20, no. 1, p. 306, 2020.

[122] T. Jungwirth, X. Marti, P. Wadley, and J. Wunderlich, "Antiferromagnetic spintronics," *Nature nanotechnology*, vol. 11, no. 3, pp. 231–241, 2016.

[123] P. Němec, M. Fiebig, T. Kampfrath, and A. V. Kimel, "Antiferromagnetic opto-spintronics," *Nature Physics*, vol. 14, no. 3, pp. 229–241, 2018.

[124] X. Zhou, X. Chen, J. Zhang, F. Li, G. Shi, Y. Sun, M. Saleem, Y. You, F. Pan, and C. Song, "From fieldlike torque to antidamping torque in antiferromagnetic mn 2 au," *Physical Review Applied*, vol. 11, no. 5, p. 054030, 2019.

[125] M. Dunz, T. Matalla-Wagner, and M. Meinert, "Spin-orbit torque induced electrical switching of antiferromagnetic MnN." *Phys. Rev. Research*, vol. 2, no. 1, p. 013347, 2020.

[126] Z. Kašpar, M. Surỳnek, J. Zubáč, F. Krizek, V. Novák, R. Campion, M. Woernle, P. Gambardella, X. Marti, P. Němec *et al.*, "Quenching of an antiferromagnet into high resistivity states using electrical or ultrashort optical pulses," *Nature Electronics*, vol. 4, no. 1, pp. 30–37, 2021.

[127] T. Janda, J. Godinho, T. Ostatnicky, E. Pfitzner, G. Ulrich, A. Hoehl, S. Reimers, Z. Šobáň, T. Metzger, H. Reichlova *et al.*, "Magneto-seebeck microscopy of domain switching in collinear antiferromagnet cumnas," *Physical Review Materials*, vol. 4, no. 9, p. 094413, 2020.

[128] J. Zubáč, Z. Kašpar, F. Krizek, T. Förster, R. P. Campion, V. Novák, T. Jungwirth, and K. Olejník, "Hysteretic effects and magnetotransport of electrically switched cumnas," *arXiv preprint arXiv:2107.05724*, 2021.

[129] M. Wang, C. Andrews, S. Reimers, O. Amin, P. Wadley, R. Campion, S. Poole, J. Felton, K. Edmonds, B. Gallagher *et al.*, "Spin flop and crystalline anisotropic magnetoresistance in cumnas," *Physical Review B*, vol. 101, no. 9, p. 094429, 2020.

[130] O. Amin, K. Edmonds, and P. Wadley, "Electrical control of antiferromagnets for the next generation of computing technology," *Applied Physics Letters*, vol. 117, no. 1, p. 010501, 2020.

[131] M. Lederman, D. Fredkin, R. O'Barr, S. Schultz, and M. Ozaki, "Measurement of thermal switching of the magnetization of single domain particles," *Journal of Applied Physics*, vol. 75, no. 10, pp. 6217–6222, 1994.

[132] R. Kodama, "Magnetic nanoparticles," *Journal of magnetism and magnetic materials*, vol. 200, no. 1-3, pp. 359–372, 1999.

[133] J. Macdonald and J. Phillips, "Topological derivation of shape exponents for stretched exponential relaxation," *The Journal of chemical physics*, vol. 122, no. 7, p. 074510, 2005.

[134] J. Phillips, "Axiomatic theories of ideal stretched exponential relaxation (ser)," *Journal of non-crystalline solids*, vol. 352, no. 42-49, pp. 4490–4494, 2006.

[135] G. Vallejo-Fernandez, N. Aley, J. Chapman, and K. O'Grady, "Measurement of the attempt frequency in antiferromagnets," *Applied Physics Letters*, vol. 97, no. 22, p. 222505, 2010.

[136] L. Lopez-Diaz, L. Torres, and E. Moro, "Transition from ferromagnetism to superparamagnetism on the nanosecond time scale," *Physical Review B*, vol. 65, no. 22, p. 224406, 2002.

[137] L. Jia, Q. Chen, Y.-S. Meng, H.-L. Sun, and S. Gao, "Elucidation of slow magnetic relaxation in a ferromagnetic 1d dysprosium chain through magnetic dilution," *Chemical Communications*, vol. 50, no. 45, pp. 6052–6055, 2014.

[138] L. J. van der Pauw, "A method of measuring the resistivity and hall coefficient on lamellae of arbitrary shape," *Philips technical review*, vol. 20, pp. 220–224, 1958.

[139] S. S. Parkin, M. Hayashi, and L. Thomas, "Magnetic domain-wall racetrack memory," *Science*, vol. 320, no. 5873, pp. 190–194, 2008.

[140] L. Berger, "Low-field magnetoresistance and domain drag in ferromagnets," *Journal of Applied Physics*, vol. 49, no. 3, pp. 2156–2161, 1978.

[141] E. Salhi and L. Berger, "Current-induced displacements and precession of a bloch wall in ni-fe thin films," *Journal of applied physics*, vol. 73, no. 10, pp. 6405–6407, 1993.

[142] G. Tatara and H. Kohno, "Theory of current-driven domain wall motion: Spin transfer versus momentum transfer," *Physical review letters*, vol. 92, no. 8, p. 086601, 2004.

[143] N. Vernier, D. A. Allwood, D. Atkinson, M. D. Cooke, and R. P. Cowburn, "Domain wall propagation in magnetic nanowires by spin-polarized current injection," *EPL (Europhysics Letters)*, vol. 65, no. 4, p. 526, 2004.

[144] M. Kläui, P.-O. Jubert, R. Allenspach, A. Bischof, J. A. C. Bland, G. Faini, U. Rüdiger, C. A. Vaz, L. Vila, and C. Vouille, "Direct observation of domain-wall configurations transformed by spin currents," *Physical review letters*, vol. 95, no. 2, p. 026601, 2005.

[145] A. Mougin, M. Cormier, J. Adam, P. Metaxas, and J. Ferré, "Domain wall mobility, stability and walker breakdown in magnetic nanowires," *EPL (Europhysics Letters)*, vol. 78, no. 5, p. 57007, 2007.

[146] S. Glathe, I. Berkov, T. Mikolajick, and R. Mattheis, "Experimental study of domain wall motion in long nanostrips under the influence of a transverse field," *Applied Physics Letters*, vol. 93, no. 16, p. 162505, 2008.

[147] S. Glathe, R. Mattheis, and D. Berkov, "Direct observation and control of the walker breakdown process during a field driven domain wall motion," *Applied Physics Letters*, vol. 93, no. 7, p. 072508, 2008.

[148] D. Djuhana, H.-G. Piao, S.-C. Yu, S. K. Oh, and D.-H. Kim, "Magnetic domain wall collision around the walker breakdown in ferromagnetic nanowires," *Journal of Applied Physics*, vol. 106, no. 10, p. 103926, 2009.

[149] L. Fan, J. Hu, Y. Su, and J. Zhu, "Influence of temperature on current-induced domain wall motion and its walker breakdown," *Journal of Magnetism and Magnetic Materials*, vol. 401, pp. 484–487, 2016.

[150] O. Gomonay, T. Jungwirth, and J. Sinova, "High antiferromagnetic domain wall velocity induced by néel spin-orbit torques," *Physical review letters*, vol. 117, no. 1, p. 017202, 2016.

[151] S. K. Kim, Y. Tserkovnyak, and O. Tchernyshyov, "Propulsion of a domain wall in an antiferromagnet by magnons," *Physical Review B*, vol. 90, no. 10, p. 104406, 2014.

[152] T. Shiino, S.-H. Oh, P. M. Haney, S.-W. Lee, G. Go, B.-G. Park, and K.-J. Lee, "Antiferromagnetic domain wall motion driven by spin-orbit torques," *Physical review letters*, vol. 117, no. 8, p. 087203, 2016.

[153] R. Wieser, E. Vedmedenko, and R. Wiesendanger, "Indirect control of antiferromagnetic domain walls with spin current," *Physical review letters*, vol. 106, no. 6, p. 067204, 2011.

[154] E. G. Tveten, A. Qaiumzadeh, and A. Brataas, "Antiferromagnetic domain wall motion induced by spin waves," *Physical review letters*, vol. 112, no. 14, p. 147204, 2014.

[155] P. Shen, Y. Tserkovnyak, and S. K. Kim, "Driving a magnetized domain wall in an antiferromagnet by magnons," *Journal of Applied Physics*, vol. 127, no. 22, p. 223905, 2020.

[156] O. Gomonay, M. Kläui, and J. Sinova, "Manipulating antiferromagnets with magnetic fields: Ratchet motion of multiple domain walls induced by asymmetric field pulses," *Applied Physics Letters*, vol. 109, no. 14, p. 142404, 2016.

[157] K. Pan, L. Xing, H. Yuan, and W. Wang, "Driving chiral domain walls in antiferromagnets using rotating magnetic fields," *Physical Review B*, vol. 97, no. 18, p. 184418, 2018.

[158] Z. Chen, Z. Yan, Y. Zhang, M. Qin, Z. Fan, X. Lu, X. Gao, and J. Liu, "Microwave fields driven domain wall motions in antiferromagnetic nanowires," *New Journal of Physics*, vol. 20, no. 6, p. 063003, 2018.

[159] W. Li, Z. Chen, D. Wen, D. Chen, Z. Fan, M. Zeng, X. Lu, X. Gao, and M. Qin, "Rotating magnetic field driven antiferromagnetic domain wall motion: Role of dzyaloshinskii-moriya interaction," *Journal of Magnetism and Magnetic Materials*, vol. 497, p. 166051, 2020.

[160] J. J. Nakane and H. Kohno, "Magnetic-field-driven antiferromagnetic domain wall motion," *Journal of the Physical Society of Japan*, vol. 90, no. 3, p. 034702, 2021.

[161] D. Wen, Z. Chen, W. Li, M. Qin, D. Chen, Z. Fan, M. Zeng, X. Lu, X. Gao, and J.-M. Liu, "Ultralow-loss domain wall motion driven by a magnetocrystalline anisotropy gradient in an antiferromagnetic nanowire," *Physical Review Research*, vol. 2, no. 1, p. 013166, 2020.

[162] S. Selzer, U. Atxitia, U. Ritzmann, D. Hinzke, and U. Nowak, "Inertia-free thermally driven domain-wall motion in antiferromagnets," *Physical review letters*, vol. 117, no. 10, p. 107201, 2016.

[163] Z. Yan, Z. Chen, M. Qin, X. Lu, X. Gao, and J. Liu, "Brownian motion and entropic torque driven motion of domain walls in antiferromagnets," *Physical Review B*, vol. 97, no. 5, p. 054308, 2018.

[164] R. Yanes, M. R. Rosa, and L. Lopez-Diaz, "Magnetic field control of antiferromagnetic domain walls in a thermal gradient," *Physical Review B*, vol. 102, no. 13, p. 134424, 2020.

[165] Y. Zhang, Z. Chen, Z. Yan, D. Chen, Z. Fan, and M. Qin, "Staggered field driven domain walls motion in antiferromagnetic heterojunctions," *Applied Physics Letters*, vol. 113, no. 11, p. 112403, 2018.

[166] H. Yang, H. Yuan, M. Yan, H. Zhang, and P. Yan, "Atomic antiferromagnetic domain wall propagation beyond the relativistic limit," *Physical Review B*, vol. 100, no. 2, p. 024407, 2019.

[167] J.-H. Zheng, A. Brataas, M. Kläui, and A. Qaiumzadeh, "Domain-wall magnetoresistance in antiferromagnetic metals," *arXiv preprint arXiv:2004.07154*, 2020.

[168] S.-H. Yang, K.-S. Ryu, and S. Parkin, "Domain-wall velocities of up to 750 m s- 1 driven by exchange-coupling torque in synthetic antiferromagnets," *Nature nanotechnology*, vol. 10, no. 3, pp. 221–226, 2015.

[169] N. Hedrich, K. Wagner, O. V. Pylypovskyi, B. J. Shields, T. Kosub, D. D. Sheka, D. Makarov, and P. Maletinsky, "Nanoscale mechanics of antiferromagnetic domain walls," *Nature Physics*, vol. 17, no. 5, pp. 574–577, 2021.

[170] S. Sugimoto, Y. Nakatani, Y. Yamane, M. Ikhlas, K. Kondou, M. Kimata, T. Tomita, S. Nakatsuji, and Y. Otani, "Electrical nucleation, displacement, and detection of antiferromagnetic domain walls in the chiral antiferromagnet mn 3 sn," *Communications Physics*, vol. 3, no. 1, pp. 1–9, 2020.

[171] N. Weber, H. Ohldag, H. Gomonaj, and F. Hillebrecht, "Magnetostrictive domain walls in antiferromagnetic nio," *Physical review letters*, vol. 91, no. 23, p. 237205, 2003.

[172] F. Krizek, S. Reimers, Z. Kašpar, A. Marmodoro, J. Michalička, O. Man, A. Edstrom, O. J. Amin, K. W. Edmonds, R. P. Campion *et al.*, "Atomically sharp domain walls in an antiferromagnet," *arXiv preprint arXiv:2012.00894*, 2020.

[173] J. M. Kosterlitz and D. J. Thouless, "Ordering, metastability and phase transitions in two-dimensional systems," *Journal of Physics C: Solid State Physics*, vol. 6, no. 7, p. 1181, 1973.

[174] A. Bogdanov and A. Hubert, "Thermodynamically stable magnetic vortex states in magnetic crystals," *Journal of magnetism and magnetic materials*, vol. 138, no. 3, pp. 255–269, 1994.

[175] E. Y. Vedmedenko, A. Ghazali, and J.-C. Lévy, "Magnetic vortices in ultrathin films," *Physical Review B*, vol. 59, no. 5, p. 3329, 1999.

[176] T. Shinjo, T. Okuno, R. Hassdorf, K. Shigeto, and T. Ono, "Magnetic vortex core observation in circular dots of permalloy," *science*, vol. 289, no. 5481, pp. 930–932, 2000.

[177] K. Everschor-Sitte, J. Masell, R. M. Reeve, and M. Kläui, "Perspective: Magnetic skyrmions—overview of recent progress in an active research field," *Journal of Applied Physics*, vol. 124, no. 24, p. 240901, 2018.

[178] K. Y. Guslienko, "Magnetic vortices and skyrmions," *Journal of Magnetics*, vol. 24, no. 4, pp. 549–567, 2019.

[179] T. Lancaster, "Skyrmions in magnetic materials," *Contemporary Physics*, vol. 60, no. 3, pp. 246–261, 2019.

[180] A. N. Bogdanov and C. Panagopoulos, "Physical foundations and basic properties of magnetic skyrmions," *Nature Reviews Physics*, vol. 2, no. 9, pp. 492–498, 2020.

[181] O. Tretiakov and O. Tchernyshyov, "Vortices in thin ferromagnetic films and the skyrmion number," *Physical Review B*, vol. 75, no. 1, p. 012408, 2007.

[182] N. Nagaosa and Y. Tokura, "Topological properties and dynamics of magnetic skyrmions," *Nature nanotechnology*, vol. 8, no. 12, pp. 899–911, 2013.

[183] B. Göbel, A. Mook, J. Henk, I. Mertig, and O. A. Tretiakov, "Magnetic bimerons as skyrmion analogues in in-plane magnets," *Physical Review B*, vol. 99, no. 6, p. 060407, 2019.

[184] B. Göbel, I. Mertig, and O. A. Tretiakov, "Beyond skyrmions: Review and perspectives of alternative magnetic quasiparticles," *Physics Reports*, vol. 895, pp. 1–28, 2021.

[185] P. Bruno, V. Dugaev, and M. Taillefumier, "Topological hall effect and berry phase in magnetic nanostructures," *Physical review letters*, vol. 93, no. 9, p. 096806, 2004.

[186] B. Göbel, A. Mook, J. Henk, and I. Mertig, "Antiferromagnetic skyrmion crystals: Generation, topological hall, and topological spin hall effect," *Physical Review B*, vol. 96, no. 6, p. 060406, 2017.

[187] S. Zhang, X. Zhang, J. Zhang, A. Ganguly, J. Xia, Y. Wen, Q. Zhang, G. Yu, Z. Hou, W. Wang *et al.*, "Direct imaging of an inhomogeneous electric current distribution using the trajectory of magnetic half-skyrmions," *Science advances*, vol. 6, no. 6, p. eaay1876, 2020.

[188] R. Tomasello, E. Martinez, R. Zivieri, L. Torres, M. Carpentieri, and G. Finocchio, "A strategy for the design of skyrmion racetrack memories," *Scientific reports*, vol. 4, no. 1, pp. 1–7, 2014.

[189] G. Finocchio, F. Büttner, R. Tomasello, M. Carpentieri, and M. Kläui, "Magnetic skyrmions: from fundamental to applications," *Journal of Physics D: Applied Physics*, vol. 49, no. 42, p. 423001, 2016.

[190] L. D. Geng and Y. M. Jin, "Magnetic vortex racetrack memory," *Journal of Magnetism and Magnetic Materials*, vol. 423, pp. 84–89, 2017.

[191] R. Juge, K. Bairagi, K. G. Rana, J. Vogel, M. Sall, D. Mailly, V. T. Pham, Q. Zhang, N. Sisodia, M. Foerster *et al.*, "Helium ions put magnetic skyrmions on the track," *Nano Letters*, vol. 21, no. 7, pp. 2989–2996, 2021.

[192] T. Uhlig, M. Rahm, C. Dietrich, R. Höllinger, M. Heumann, D. Weiss, and J. Zweck, "Shifting and pinning of a magnetic vortex core in a permalloy dot by a magnetic field," *Physical review letters*, vol. 95, no. 23, p. 237205, 2005.

[193] D. Nissen, D. Mitin, O. Klein, S. Arekapudi, S. Thomas, M. Im, P. Fischer, and M. Albrecht, "Magnetic coupling of vortices in a two-dimensional lattice," *Nanotechnology*, vol. 26, no. 46, p. 465706, 2015.

[194] N. Gao, S.-G. Je, M.-Y. Im, J. W. Choi, M. Yang, Q.-c. Li, T. Wang, S. Lee, H.-S. Han, K.-S. Lee *et al.*, "Creation and annihilation of topological meron pairs in in-plane magnetized films," *Nature communications*, vol. 10, no. 1, pp. 1–9, 2019.

[195] Y. Wang, N. Mehmood, Z. Hou, W. Mi, G. Zhou, X. Gao, and J. Liu, "Electric field-driven rotation of magnetic vortex originating from magnetic anisotropy reorientation," *Advanced Electronic Materials*, p. 2100561, 2021.

[196] K. Yamada, S. Kasai, Y. Nakatani, K. Kobayashi, H. Kohno, A. Thiaville, and T. Ono, "Electrical switching of the vortex core in a magnetic disk," *Nature materials*, vol. 6, no. 4, pp. 270–273, 2007.

[197] S. Kasai, P. Fischer, M.-Y. Im, K. Yamada, Y. Nakatani, K. Kobayashi, H. Kohno, and T. Ono, "Probing the spin polarization of current by soft x-ray imaging of current-induced magnetic vortex dynamics," *Physical review letters*, vol. 101, no. 23, p. 237203, 2008.

[198] K. Y. Guslienko, K.-S. Lee, and S.-K. Kim, "Dynamic origin of vortex core switching in soft magnetic nanodots," *Physical review letters*, vol. 100, no. 2, p. 027203, 2008.

[199] K. Y. Guslienko, "Magnetic vortex state stability, reversal and dynamics in restricted geometries," *Journal of nanoscience and nanotechnology*, vol. 8, no. 6, pp. 2745–2760, 2008.

[200] S. Kasai, Y. Nakatani, K. Kobayashi, H. Kohno, and T. Ono, "Current-driven resonant excitation of magnetic vortices," *Physical review letters*, vol. 97, no. 10, p. 107204, 2006.

[201] M. Möller, J. H. Gaida, S. Schäfer, and C. Ropers, "Few-nm tracking of current-driven magnetic vortex orbits using ultrafast lorentz microscopy," *Communications Physics*, vol. 3, no. 1, pp. 1–7, 2020.

[202] M. Kläui, M. Laufenberg, L. Heyne, D. Backes, U. Rüdiger, C. A. Vaz, J. A. C. Bland, L. J. Heyderman, S. Cherifi, A. Locatelli *et al.*, "Current-induced vortex nucleation and annihilation in vortex domain walls," *Applied physics letters*, vol. 88, no. 23, p. 232507, 2006.

[203] Z. Li, J. Su, S.-Z. Lin, D. Liu, Y. Gao, S. Wang, H. Wei, T. Zhao, Y. Zhang, J. Cai *et al.*, "Field-free topological behavior in the magnetic domain wall of ferrimagnetic gdfeco," *Nature communications*, vol. 12, no. 1, pp. 1–7, 2021.

[204] X. Yu, W. Koshibae, Y. Tokunaga, K. Shibata, Y. Taguchi, N. Nagaosa, and Y. Tokura, "Transformation between meron and skyrmion topological spin textures in a chiral magnet," *Nature*, vol. 564, no. 7734, pp. 95–98, 2018.

[205] Y. Gao, Q. Yin, Q. Wang, Z. Li, J. Cai, T. Zhao, H. Lei, S. Wang, Y. Zhang, and B. Shen, "Spontaneous (anti) meron chains in the domain walls of van der waals ferromagnetic fe5- xgete2," *Advanced Materials*, vol. 32, no. 48, p. 2005228, 2020.

[206] M. Coïsson, G. Barrera, F. Celegato, A. Manzin, F. Vinai, and P. Tiberto, "Magnetic vortex chirality determination via local hysteresis loops measurements with magnetic force microscopy," *Scientific reports*, vol. 6, no. 1, pp. 1–9, 2016.

[207] M. Li, A. Rai, A. Pokhrel, A. Sapkota, C. Mewes, T. Mewes, D. Xiao, M. De Graef, and V. Sokalski, "Magnetic domain wall substructures in pt/co/ni/ir multi-layers," *Journal of Applied Physics*, vol. 130, no. 15, p. 153903, 2021.

[208] R. Juge, N. Sisodia, J. U. Larrañaga, Q. Zhang, V. T. Pham, K. G. Rana, B. Sarpi, N. Mille, S. Stanescu, R. Belkhou *et al.*, "Skyrmions in synthetic antiferromagnets and their nucleation via electrical current and ultrafast laser illumination," *arXiv preprint arXiv:2111.11878*, 2021.

[209] A. Kolesnikov, V. Plotnikov, E. Pustovalov, A. Samardak, L. Chebotkevich, A. Ognev, and O. A. Tretiakov, "Composite topological structure of domain walls in synthetic antiferromagnets," *Scientific reports*, vol. 8, no. 1, pp. 1–9, 2018.

[210] J. Harrison, H. Jani, and P. G. Radaelli, "A route towards stable homochiral topological textures in a-type antiferromagnets," *arXiv preprint arXiv:2111.15520*, 2021.

[211] P. Radaelli, J. Radaelli, N. Waterfield-Price, and R. Johnson, "Micromagnetic modeling and imaging of vortex— meron structures in an oxide— metal heterostructure," *Physical Review B*, vol. 101, no. 14, p. 144420, 2020.

[212] M. Augustin, S. Jenkins, R. F. Evans, K. S. Novoselov, and E. J. Santos, "Properties and dynamics of meron topological spin textures in the two-dimensional magnet crcl3," *Nature communications*, vol. 12, no. 1, pp. 1–9, 2021.

[213] L. Shen, J. Xia, X. Zhang, M. Ezawa, O. A. Tretiakov, X. Liu, G. Zhao, and Y. Zhou, "Current-induced dynamics and chaos of antiferromagnetic bimerons," *Physical Review Letters*, vol. 124, no. 3, p. 037202, 2020.

[214] X. Li, L. Shen, Y. Bai, J. Wang, X. Zhang, J. Xia, M. Ezawa, O. A. Tretiakov, X. Xu, M. Mruczkiewicz *et al.*, "Bimeron clusters in chiral antiferromagnets," *npj Computational Materials*, vol. 6, no. 1, pp. 1–9, 2020.

[215] J. Sort, K. Buchanan, V. Novosad, A. Hoffmann, G. Salazar-Alvarez, A. Bollero, M. Baró, B. Dieny, and J. Nogués, "Imprinting vortices into antiferromagnets," *Physical review letters*, vol. 97, no. 6, p. 067201, 2006.

[216] J. Wu, D. Carlton, J. Park, Y. Meng, E. Arenholz, A. Doran, A. Young, A. Scholl, C. Hwang, H. Zhao *et al.*, "Direct observation of imprinted antiferromagnetic vortex states in coo/fe/ag (001) discs," *Nature Physics*, vol. 7, no. 4, pp. 303–306, 2011.

[217] F. P. Chmiel, N. Waterfield Price, R. D. Johnson, A. D. Lamirand, J. Schad, G. van der Laan, D. T. Harris, J. Irwin, M. S. Rzchowski, C.-B. Eom *et al.*, "Observation of magnetic vortex pairs at room temperature in a planar α-fe2o3/co heterostructure," *Nature Materials*, vol. 17, no. 7, pp. 581–585, 2018.

[218] H. Jani, J.-C. Lin, J. Chen, J. Harrison, F. Maccherozzi, J. Schad, S. Prakash, C.-B. Eom, A. Ariando, T. Venkatesan *et al.*, "Antiferromagnetic half-skyrmions and bimerons at room temperature," *Nature*, vol. 590, no. 7844, pp. 74–79, 2021.

[219] A. A. Thiele, "Steady-state motion of magnetic domains," *Phys. Rev. Lett.*, vol. 30, pp. 230–233, 1973.

[220] O. A. Tretiakov, D. Clarke, G.-W. Chern, Y. B. Bazaliy, and O. Tchernyshyov, "Dynamics of domain walls in magnetic nanostrips," *Phys. Rev. Lett.*, vol. 100, no. 12, p. 127204, 2008.

[221] E. G. Tveten, A. Qaiumzadeh, O. A. Tretiakov, and A. Brataas, "Staggered dynamics in antiferromagnets by collective coordinates," *Phys. Rev. Lett.*, vol. 110, p. 127208, 2013.

[222] J. Barker and O. A. Tretiakov, "Static and dynamical properties of antiferromagnetic skyrmions in the presence of applied current and temperature," *Physical review letters*, vol. 116, no. 14, p. 147203, 2016.

Appendix A

Device Fabrication

All transport devices used in this thesis were fabricated at the University of Nottingham, either in the A-floor clean rooms using chemical wet etching, or in the Nanoscale and Microscale Research Centre (nmRC) using electron-beam lithography.

A.1 Photolithography and Chemical Wet Etching

Chips of CuMnAs were scribed from the wafer along the substrate cleave axes using a Dynapert scriber. They were then cleaned in Ethyl Lactate, Methanol, Acetone, and IPA for >2 min in each. A layer of AZ ECI 3007 positive photoresist was spin coated onto the chip using a Laurell spin-coater at 4000 rpm for 30 s. Edge beading was removed using a fine-tip cotton bud and the chip was baked on a hotplate at ∼90 °C for 1 min. The chip was then loaded into a Suss MJB-3 photolithography aligner with a chrome plated soda lime mask containing the device design. Exposure was done for 6 s with a dose of 9.5 mW cm^{-2}. After the exposure, the design was developed in a developer solution of AZ400K:H_2O, ratio 1:6, for ∼15 s. Dipping the chip in deionised water ensured no overdevelopment. It was important to use a developer containing potassium, as this removed the Al capping layer prior to chemical wet etching.
Once developed, the CuMnAs layer was etched using either chemical wet etching or ion milling. For most cases chemical wet etching was the method used. The etch solution consisted of H_2O:H_2O_2:H_3PO_4, ratio 400:10:1, which etches CuMnAs at a rate of ∼1 nm s^{-1}. The chip was rinsed in deionised water to halt etching.
Devices used for non-XPEEM experiments were mounted onto in-house made, 12-pin ceramic headers using GE varnish or silver paint. Device contact pads were bonded to the header pins using a wedge wire bonder and Al wire.

A.2 Electron-beam Lithography and Ion Milling

Electron-beam lithography (EBL) was used to fabricate a few devices for XPEEM experiments. This technique is beneficial because device designs can be made using AutoCAD software and do not need to be printed onto chrome plated photolithography masks. Furthermore, device dimensions can be smaller than using typical photolithography masks, reaching a minimum of ∼500 nm owing to EBL resolution of ±20 nm.
EBL was carried out using a nanobeam nB5 (nanobeam limited, Cambridge) with an accelerating voltage of 80 kV. After cleaning with Acetone and IPA, the sample was coated with a 200 nm thick layer of AR-P 6200.09 (allresist GmbH, Strausberg) and spin coated at 4000 rpm for 60 s. The samples were soft baked on a hot plate for 6 min at 85 °C, which is considerably lower than the recommended temperature (150 °C) in order to ensure the magnetic properties of the CuMnAs layer were not altered.

After loading into the nB5, the beam was focused using a scratch in the corner; astigmatism and alignment was carried out automatically. A current of around 2 nA was used to reduce charging and to ensure the smallest possible spotsize. The nanobeam software fractures the pattern into 500 µm write fields which are stitched together. There is an error around 20 nm in doing this, so it was ensured that the edges of these fields did not cross any critical areas. The pattern was exposed using a dose of 465 µC cm^{-2}. The exposed sample was then developed in AR 600-546 for 60 s and rinsed in IPA for 30 s to stop the development.

Appendix B

Room Temperature Transport System

The design of the system is a T-shaped vacuum chamber, as shown in the computer aided design (CAD) drawing of Figure B.1a. The system can achieve vacuum pressures $\sim 10^{-7}$ hPa and ≤ 2 mK temperature stability in a temperature range $-10\,^{\circ}\mathrm{C}$ to $60\,^{\circ}\mathrm{C}$ controlled by a Peltier device. The copper cylinder, at the bottom of the T, acts both as a mounting point and as a thermal feedthrough. The two arms of the T are used for signal feedthroughs and the Peltier device is sandwiched between a copper sample space and the bottom copper cylinder of the vacuum chamber, with a bracket to tidy the wiring and keep the Peltier device central. There are four holes in the copper cylinder below the vacuum chamber to allow L-shaped heat pipes to conduct heat. A two-part copper bracket sandwiches the pipes and is in thermal contact with a large heatsink assembly. The signal feedthroughs facilitate a 12-pin header on one side and the two power pins of the Peltier device and four pins of a PT100 platinum resistor on the other. The sample space houses the resistor and the 12-pin sample header's matching socket as shown in Figure B.1b. The inset illustrations show the sample header, fabricated from a polyether ether ketone (PEEK) disk with brass pins for electrical contact and a copper slug as the sample stage. The sample is stuck to this slug using thermally conductive varnish or silver conductive paste, before bonding wires are used to connect the device to the pins of the header. Once loaded into the sample socket, the chamber lid applied small downward pressure onto the sample header, ensuring good thermal contact between the copper slug and the raised stem for improved heat transfer to the Peltier device.

To the Peltier temperature (and corresponding system temperature) is controlled by a Meerstetter Engineering$^{\mathrm{TM}}$ TEC-1091 precision temperature controller. This reads both the sample space temperature and the external copper block temperature and has a range of features including protections against over current when changing from heating to cooling and auto-tuning of the PID. Figure B.1c shows the temperature stability, averaged over a 10 h period, of the system at three set temperatures, $-5\,^{\circ}\mathrm{C}$, $21\,^{\circ}\mathrm{C}$, and $60\,^{\circ}\mathrm{C}$. Plotted is the difference between the average temperature and the set point, $\bar{T} - T_{\mathrm{sp}}$. The orange shaded area shows the standard deviation from the set point temperature; maximum (± 2 mK) at the lowest temperature ($-5\,\mathrm{K}$) and reducing (± 1 mK) as the set point temperature increases.

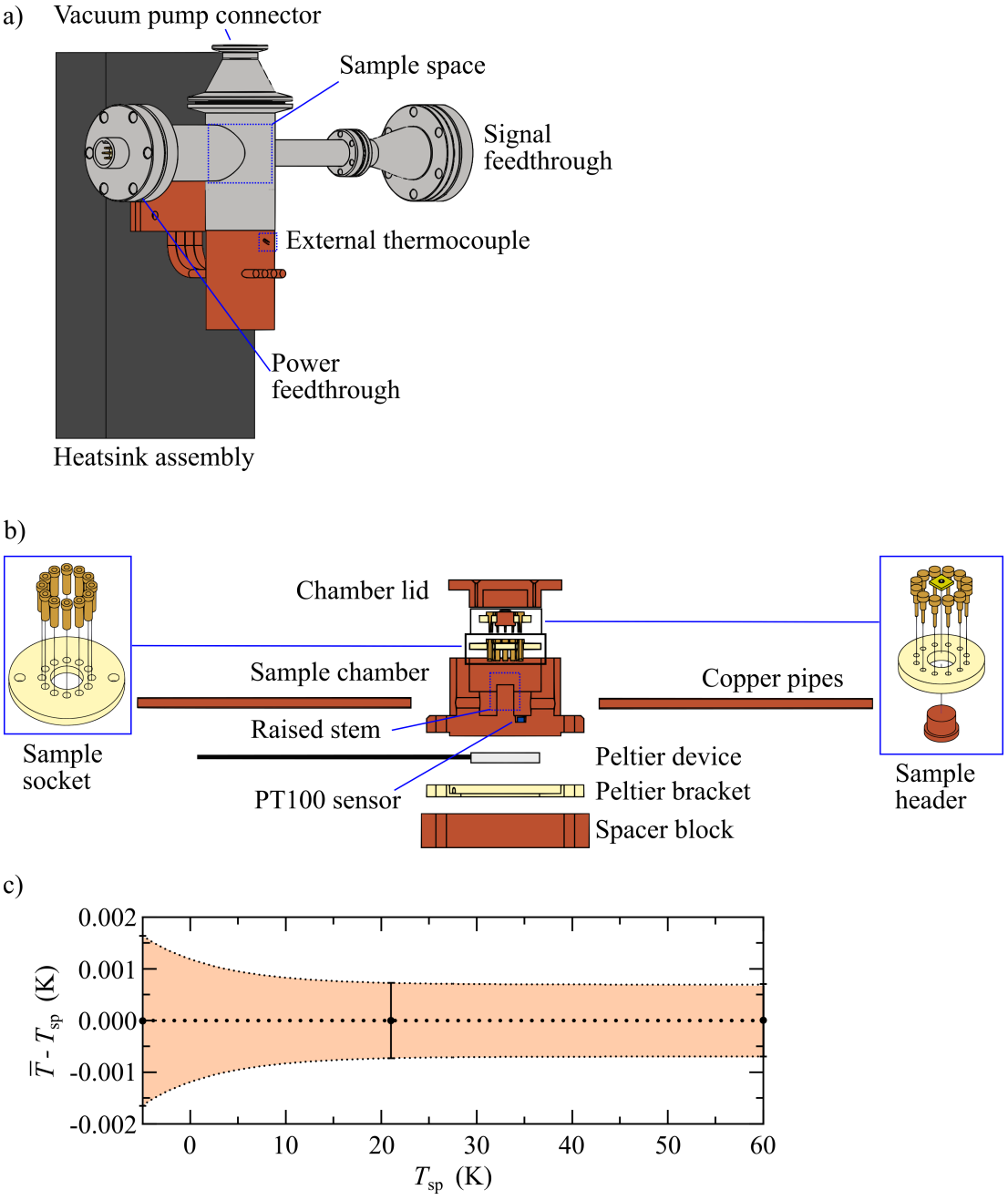

Figure B.1: *a) External view of the Peltier controlled room temperature system. b) Exploded view of the sample chamber with mounting socket and sample header. c) Temperature stability measured over a* 10 h *period. Plotted is the difference between the mean temperature,* $\bar{T}$*, measured by the PT100 sensor and the temperature set point,* T_{sp} *at three different set temperatures,* −5 °C, 21 °C, *and* 60 °C. *The shaded area corresponds to the standard deviation about the mean temperature.*

Appendix C

List of Abbreviations

AF	Antiferromagnet
FM	Ferromagnet
SAF	Synthetic antiferromagnet
MRAM	Magnetoresistive random access memory
STT	Spin-transfer torque
SOT	Spin-orbit torque
NSOT	Néel spin-orbit torque
DW	Domain wall
SOC	Spin-orbit coupling
AMR	Anisotropic magnetoresistance
SHMR	Spin Hall magnetoresistance
XMCD	X-ray magnetic circular dichroism
XMLD	X-ray magnetic linear dichroism
PEEM	Photoemission electron microscopy